INVESTIGATION ON THE WS_2 THIN FILM GROWTH AND DEVICE FABRICATION

YU YANG

Ph.D

The Hong Kong Polytechnic University

2018

The Hong Kong Polytechnic University

Department of Electronic and Information Engineering

Investigation on the WS_2 Thin Film Growth and Device Fabrication

YU Yang

A thesis submitted in partial fulfilment of the requirements for the degree of Doctor of Philosophy

July 2017

CERTIFICATE OF ORIGINALITY

I hereby declare that this thesis is my own work and that, to the best of my knowledge and belief, it reproduces no material previously published or written, nor material that has been accepted for the award of any other degree or diploma, except where due acknowledgement has been made in the text.

_____

YU Yang

ABSTRACT

Transition metal dichalcogenides (TMDC) layered materials with their remarkable layer-dependent electrical and optical properties have attracted a great deal of research interests recently. The weak van der Waals force dominated layer interactions can accommodate large lattice mismatch to reduce interface defects, because the bonds in a single layer are fully saturated. Additionally, lattice strain is almost absent between layers for such materials. These features make TMDC layered materials to be as potential materials for the fabrication of ultra-thin and flexible electronic and optoelectronic devices. Single-layer or few-layer TMDC materials can be easily acquired by mechanical exfoliation from a single crystal for basic investigations to fabricate proof-of-concept electronic devices. Nevertheless, the exfoliation method is limited to microscale, which is not appropriate for production on large scale. In this thesis, wafer-scale p-type WS_2 thin film growth by molecular beam epitaxy (MBE) and chemical vapor deposition (CVD) had been systematically investigated. In addition, WS_2/GaN p-n junctions with low leakage current were fabricated by the transfer of p-type WS_2 thin films onto n-type GaN, and ultra-thin WS_2-based FETs were fabricated by using 40 nm WS_2 thin films as the channel layer.

Only the (002) family X-ray diffraction (XRD) peaks were detected for the WS_2 thin film grown by MBE method, indicating strong preferential growth along the [001] crystal orientation of WS_2. For the CVD growth of the WS_2 thin film, by employing a thin Ni layer as texture promoter, the crystal structure of the WS_2 thin film changed from randomly oriented crystallites to large layered crystals with their c-axis oriented perpendicular to the growth substrate with the carrier mobility of 63.3 cm^2/Vs. The liquid NiS_x phase in the sulfurization process served as the liquid crystallization seeds for van der Waals rheotaxy resulting in horizontal growth of WS_2 crystallites with enhanced crystal size.

Taking advantage of the hydrophobicity of WS_2 and hydrophilicity of sapphire

substrates, the wafer-scale etching-free transfer method was developed to transfer the as-grown WS_2 thin films onto other substrates without inducing cracks or wrinkles to fabricate heterojunctions. Compared to conventional epitaxial-grown heterojunctions, a wide range of semiconductors can be used for the fabrication of heterojunctions by this etching-free transfer method. Additionally, the etching-free approach does not require the use of any destructive etchants and thereby enables the reuse of substrates. The p-n junctions fabricated by transferring p-type WS_2 thin films onto n-type GaN layer had a quite low leakage current density of 29.6 $\mu A/cm^2$, whereas the direct grown WS_2/GaN p-n junction had a large leakage current density of 92.4 mA/cm^2. This demonstrates superior performance of the transferred device compared to the as-grown WS_2/GaN p-n junctions. This etching-free transfer method is expected to enormously expand the applications of WS_2 thin films for optoelectronic and electronic devices.

Layered WS_2 thin films, which have fewer dangling bonds, are attractive for use as channel layers in ultra-thin field effect transistors (FETs). In this thesis, uniform large-area ultra-thin WS_2 thin films, down to 40 nm, were obtained by a chemical etching method to fabricate ultra-thin FETs. The WS_2-based FET employing a 40 nm WS_2 thin film as the channel layer had a field-effect mobility of 0.54 $cm^2V^{-1}s^{-1}$ and on/off ratio of 2700.

PUBLICATIONS

[1] Yang Yu, Patrick W. K. Fong, Shifeng Wang, and Charles Surya*, “Fabrication of WS_2/GaN p-n junction by wafer-scale WS_2 thin film transfer ”, *Scientific Reports*, ***6***, 37833, (2016)

[2] Shifeng Wang, Wei Wang, W. K. Fong, Yang Yu, and Charles Surya*, “Tin compensation for the SnS based optoelectronic devices”, *Scientific Reports*, ***7***, 39704, (2017)

ACKNOWLEDGEMENTS

I am deeply honored and sincerely grateful to have had the opportunity to pursue my Ph.D. studies in the department of Electronic and Information Engineering at The Hong Kong Polytechnic University. I would like to express my most profound gratitude to my supervisor, Prof. Charles Surya, for his patient guidance, invaluable advice and active encouragement and support during my Ph.D. research. I have benefited considerably from his comprehensive planning, meticulous consideration and serious attitude towards my academic work.

I would also like to thank other members of the Research Group: Dr. Patrick Fong, Dr. S. F. Wang, Mr. C. W. Lip, Dr. Annie Ng, Mr. Q. Shen, Mr. Z. W. Ren and Mr. J. X. Zhou, for their helpful discussions, kindness and support during my research. My special thanks go to Dr. Patrick Fong, for his guidance in the handling of the MBE system, kind assistance in thin film deposition and his readiness to provide academic suggestions.

I wish to acknowledge Dr. Hardy Lui from the Materials Research Centre, Dr. Terence Wong and Ms. Joyce Lau from the University Research Facility in Materials Characterization and Device Fabrication Lab, and Dr. Vincent Chan from the department of Applied Physics, for their technical support in the material characterizations and device fabrication.

I wish to show my appreciation to my parents for their endless love and support throughout the entire period of my studies. Finally I would like to acknowledge my special appreciation to my beloved wife Chi Zhang. Her enduring love, understanding and encouragement have provided the most significant support to enable the completion of my studies.

TABLE OF CONTENTS

LIST OF FIGURES

LIST OF TABLES

CHAPTER 1 INTRODUCTION

1.1 Introduction

Semiconductor material is important for the electronics industry due to its optical and electrical properties that can be applied to fabricate electronic and optoelectronic devices. [1, 2] Silicon is the main material used for large-scale integrated circuits. [3] However, in the field of ultra-high-speed integrated circuit and optoelectronic devices, compound semiconductor materials are irreplaceable. [4, 5] The famous Moore's law states that the number of transistors per chip can double every two years, approximately. [6] Moore's law has been proven accurate for several decades, and was employed to guide long-term planning for research and development in the semiconductor industry. However, as integrated circuits are becoming increasingly compact in size, the Si-based transistor will eventually meet its physical dimension limitation due to the quantum tunneling effect that starts at about 6 nm, [7] by which electrons can easily tunnel across the junction. Therefore, it will be difficult to produce the next generations of electronic devices by relying on today's manufacturing techniques. Moreover, the modern era of electronics demands the development of more novel electronics, such as flexible electronics, large-area electronics, and transparent electronics. Consequently, we need to explore new materials to produce more compact chips and develop new applications.

The two-dimensional (2D) materials system is a very promising candidate to

advance device fabrication technology because of its high packing density, resulting in a faster circuit speed and lower power consumption compared to the traditional Si-based electronic devices. In 2D layered materials, the force between cationic layers is dominated by van der Waals force, which theoretically provides the possibility of high tolerance in interface mismatch in a solid-state junction. The excellent performances of the electronic devices produced by transition metal dichalcogenides (TMDCs) layered materials, including field-effect transistors, [8, 9] sensors[10, 11] and photodetectors, [12] showed their potential as prospective alternatives to Si in conventional electronic devices and organic semiconductors in flexible devices. [13, 14]

Two-dimensional materials, including graphene as a conducting material, hexagonal boron nitride (BN) as a dielectric material, and TMDCs as semiconductor materials are key components for the fabrication of 2D devices. Graphene was discovered by Novoselov and Geim [15] in 2004 is the most widely studied 2D material due to its remarkable physical properties, such as its high optical transmittance and superior electrical conductivity. [16-18] However, unlike the semiconductor Si, graphene has no bandgap between its valence and conduction bands. This limits its application in the semiconductor industry. [15, 19] Two-dimensional TMDC materials, such as $MoSe_2$, WS_2, $MoTe_2$, MoS_2, WSe_2, etc., are promising channel materials to fabricate ultra-thin field-effect transistors (FETs). [20, 21] These layered semiconductors also have the potential to be used as solar materials

due to their high light absorption and proper bandgaps ranging from 1 eV to 2.2 eV. [22] Although the surface morphology and crystal structure of TMDC materials have already been widely studied, [23, 24] an in-depth study of their electrical and optical properties, which are the critical parameters for device performance, is still needed.

Obtaining high quality TMDC thin films, not only with excellent crystallinity and surface morphology, but also with high carrier mobility and low surface defects, is a key objective when it comes to fabricating high quality electronic and optoelectronic devices. To acquire 2D materials for electronic device fabrication, the mechanical exfoliation from bulk materials developed by Novoselov and Geim [15] in 2004 is the most widely used method. Although high quality and micro-sized 2D materials can be obtained through this mechanical exfoliation method, it is only appropriate for basic material examination and proof-of-concept device fabrication. This is because the thickness and effective area of the mechanically exfoliated 2D layers are difficult to replicate and control. For electronic and optoelectronic applications, large-area 2D materials are definitely significant for the large scale manufacturing of flexible and transparent electronic and optoelectronic devices. Thus, a suitable technique for the realization of large-area 2D materials should be developed to replace the mechanical micro-exfoliation of 2D materials. Molecular beam epitaxy (MBE) and chemical vapor deposition (CVD) are two effective deposition methods to grow high quality, large-area 2D materials. In this thesis, the synthesis of large-area WS_2 layer materials by both the CVD and MBE methods is systematically

studied.

1.2 Motivation

In this thesis, the research focus is on the investigation of the van der Waals epitaxial growth of high quality WS_2 layered material and its application in the fabrication of electronic devices. The motivation behind this research is as follows:

(1) The most commonly used method to obtain monolayer or few layers TMDC materials is the micro-mechanical exfoliation of a single crystal due to the weak layer interaction governed by van der Waals force. However, the exfoliated materials are limited to micron-sized scale which is not appropriate for production on large scale. In this thesis, different epitaxial growth techniques are studied to grow large-area WS_2 thin films.

(2) WS_2 commonly exists in a mixture of type-I and type-II crystallites with their *c*-axis parallel or perpendicular to the surface of the substrate. However, for electronic applications, WS_2 with large type-II layered crystallites is required for device fabrication. Thus, a detailed investigation is performed to grow highly textured type-II WS_2 thin films.

(3) Most of semiconductors and conductors are not suitable for the high growth temperature of WS_2. In addition, they may not be stable in a sulfur rich environment. For example, a Si substrate can be destroyed at around 900°C under S atmosphere, because it can be converted to SiS_x and its melting point is much

lower than that of Si. This imposes significant restrictions on the fabrication of WS_2-based heterojunctions. Thus, the development of a layer transfer technique to overcome this restraint is very important. Furthermore, the layered material can be transferred to any arbitrary substrate without suffering from any mismatches in the lattice constant and thermal coefficients.

(4) The traditional transfer of 2D materials commonly makes use of chemical etchants, such as KOH and HF, which contaminates the surface of the film, resulting in considerable degradations of device performance. Thus, the realization of an etching-free transfer method will have a significant impact on the fabrication of TMDC electronic devices.

(5) Another significant characteristic of 2D TMDCs is the flexibility of the weak interlayer interaction of van der Waals forces. This creates the possibility of fabricating wearable electronics. In addition, the layered WS_2 is a suitable candidate to fabricate ultra-thin FETs.

CHAPTER 2 BACKGROUND

2.1 Two-dimensional Layer Materials

Two-dimensional materials with their novel electronic and optical properties have the potential to be used in nano-electronic and optoelectronic devices. Graphene was first acquired through micro-mechanical exfoliation from graphite by A. K. Geim *et al.* in 2004.[15] Since then, it has attracted of the attention of researchers who are interested in its remarkable physical and chemical properties, for instance, its large specific surface area of 2630 m^2/g,[25] outstanding mechanical strength with a Young's modulus as high as 1 TPa,[26] and remarkable optical transmittance reaching 97.7%.[16] Moreover, graphene has a superior electrical conductivity of 200 S/m due to its novel band structure. This means that the conduction band meets the valence band at a specific point, called the Dirac point, in the Brillouin zone, [17, 18] as shown in Figure 2.1.

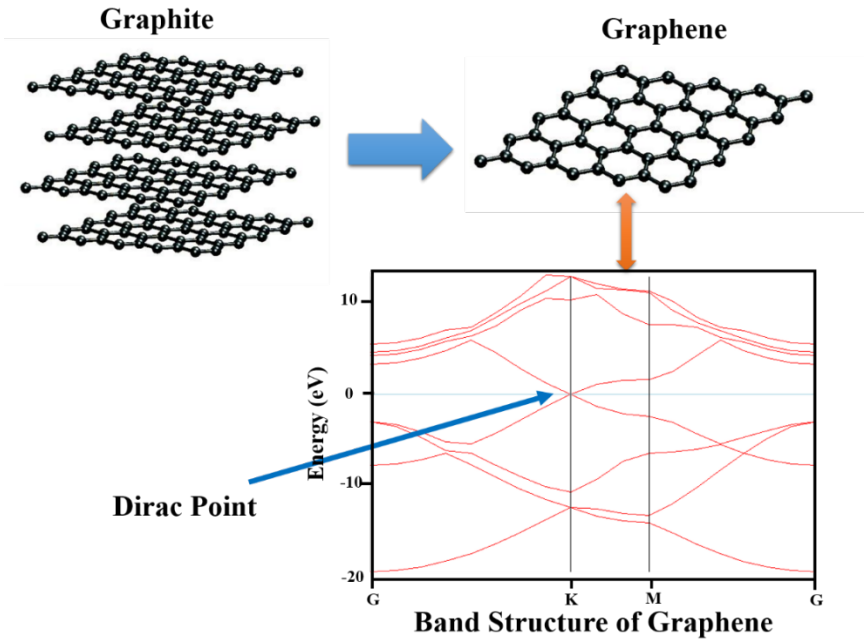

Figure 2.1 Crystal structure and energy band structure of graphene.

However, graphene has no bandgap between its valence and conduction bands. This limits its replacement of silicon in the semiconductor industry.[15, 19] Following the discovery of graphene, other isolated monolayer or few layers materials have emerged and rapidly developed. These materials include dielectric hexagonal boron nitride (hBN), transition metal trichalcogenides ($NbSe_3$, $TaSe_3$), transition metal dichalcogenides ($TaSe_2$, MoS_2, WS_2, $MoSe_2$,WSe_2, etc.), transition metal oxides ($LaMnO_3$, $LaVO_3$), and other complex oxide layered materials. The categories of 2D materials are summarized in Table 2.1. [27, 28]

Table 2.1 Category of 2D materials. [27, 28]

<table>
<tr><td>Graphene Family</td><td>Graphene</td><td colspan="2">hBN</td><td>BCN</td><td>Fluorographene</td><td>Graphene Oxide</td></tr>
<tr><td rowspan="2">2D Chalcogenides</td><td rowspan="2">MoS_2, WS_2, $MoSe_2$, WSe_2</td><td colspan="3" rowspan="2">$MoTe_2$, WTe_2, ZrS_2, $ZrSe_2$ … etc.</td><td colspan="2">Metallic dichalcogenides: $NbSe_2$, NbS_2, TaS_2, TiS_2, $NiSe_2$ …etc.</td></tr>
<tr><td colspan="2">Layered Semiconductors: GaSe, GaTe, InSe, Bi_2Se_3 … etc.</td></tr>
<tr><td rowspan="2">2D Oxides</td><td>Micas, BSCCO</td><td colspan="3">MoO_3, WO_3</td><td rowspan="2">Perovskite-type:$LaNb_2O_7$,

$Bi_4Ti_3O_{12}$, $Ca_2Ta_2TiO_{10}$ … etc.</td><td>Hydroxides: $Eu(OH)_2$, …etc.</td></tr>
<tr><td>Layered Cu oxides</td><td colspan="3">TiO_2, MnO_2, V_2O_5,RuO_2 … etc.</td><td>Others</td></tr>
</table>

Transition metal dichalcogenides layered materials have a forceful in-plane bonds, and their out-of-plane forces mostly are weak van der Waals forces which enables us to obtain 2D thin layers of transition metal chalcogenides.[29, 30] Transition metal dichalcogenides, such as $MoSe_2$, WS_2 and WSe_2, with different sized direct or indirect bandgaps are necessary components for ultra-thin 2D electronic

devices, such as transistors, photodetectors and electroluminescent devices. [31-34] The improvement of 2D film quality and the fabrication of efficient devices composed of 2D materials has become a hot research topic recently.

TMDCs with the formula MX_2, M is transition metal element (Mo, W) and X is chalcogen element (Te, S or Se), have several different combinations of chemical compound with different electronic properties. For example, NbS_2 and TaS_2 have metal and superconducting properties, whereas MoS_2 and WS_2 are semiconductor materials that have the potential to be used in a large variety of applications due to their proper bandgaps. [20, 21] The electronic properties of TMDCs are summarized in Table 2.2. [29, 35-37]

2.1.1 Crystal Structures and Physical Properties of TMDCs

Every individual layer of bulk TMDCs includes a transition metal (Mo, W) atomic layer in between two chalcogen (S, Se) atomic layers. These layered materials have the form of X-M-X consisting of a hexagonal plane of transition metal atoms in between two planes of chalcogen atoms, such as MoS_2 and WS_2.[38-40] The hexagonal structure of MoS_2 (WS_2) layers are constructed by a trigonal prism of six sulfur atoms with one Mo (W) atom located in the center.[41-43] This kind of tri-layer sandwich structure of monolayer MoS_2 (WS_2) can form three possible configurations of bulk MoS_2 (WS_2) by different stacking orders and atom coordination with adjacent S atoms, as shown in Figure 2.2.[44, 45]

Table 2.2 Electronic properties of TMDCs. [29, 35-37]

Material	Electronic Property	Material	Electronic Property
NbS_2	Metallic; Superconducting	$NbSe_2$	Metallic; Superconducting
TaS_2	Metallic ; Superconducting	$TaSe_2$	Metallic ; Superconducting
MoS_2	Semiconducting 1L: 1.8 eV; Bulk: 1.2 eV	$MoSe_2$	Semiconducting 1L: 1.5 eV; Bulk: 1.1 eV
WS_2	Semiconducting 1L: 1.9-2.1 eV; Bulk: 1.4 eV	WSe_2	Semiconducting 1L: 1.7 eV; Bulk: 1.2 eV

The 3R and 2H structures, with trigonal prismatic coordination, are commonly found in nature.[46, 47] The 3R form has a rhombohedra symmetry consisting of three S-Mo-S (S-W-S) units. The 2H form has a hexagonal symmetry including two S-Mo-S (S-W-S) units for each primitive cell. The 1T form has a tetragonal symmetry with a octahedral coordination geometry that is a metastable configuration of only one S-Mo-S (S-W-S) layer as the repeated unit.[48, 49]

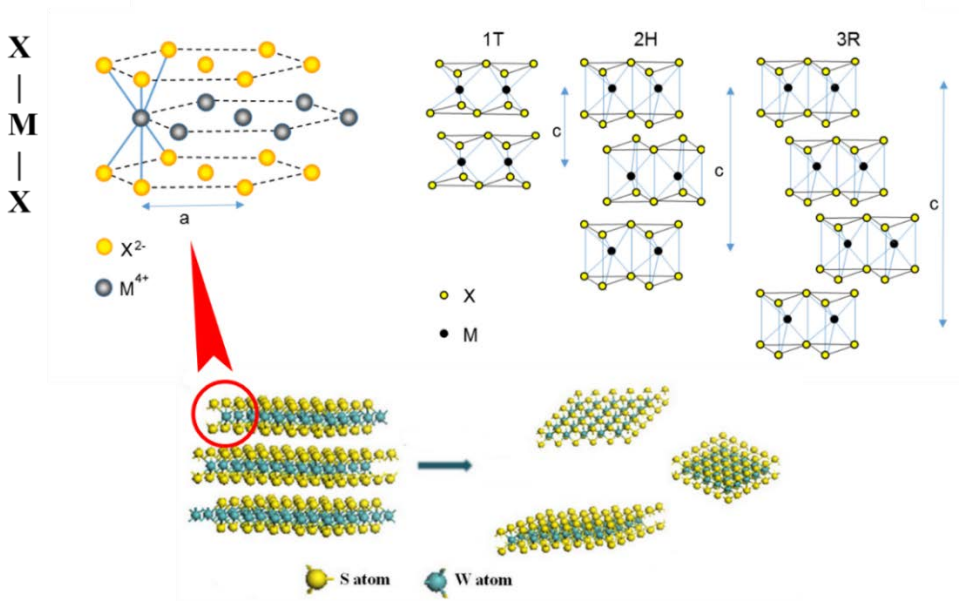

Figure 2.2 Crystal structure and three configurations of bulk MoS_2 or WS_2.[45]

Recently, the unique layer-dependent properties of TMDC materials have attracted attention, especially since the bandgap of a few TMDCs can change from an indirect bandgap of the bulk material into a direct bandgap while in the monolayer form. For example, the bandgap of the bulk WS_2 changes from an indirect energy bandgap of 1.3 eV to a direct energy bandgap of 2.1 eV for a monolayer structure. (Figure 2.3).[50-52] As photoluminescence only occurs in the direct bandgap materials, it provides the possibility that TMDCs can be used for light emission applications by reducing the thickness to a single layer.[36, 53, 54] Valley polarization exists in the monolayer MoS_2 due to its novel electronic property, which cannot be observed in bulk MoS_2.[55, 56]

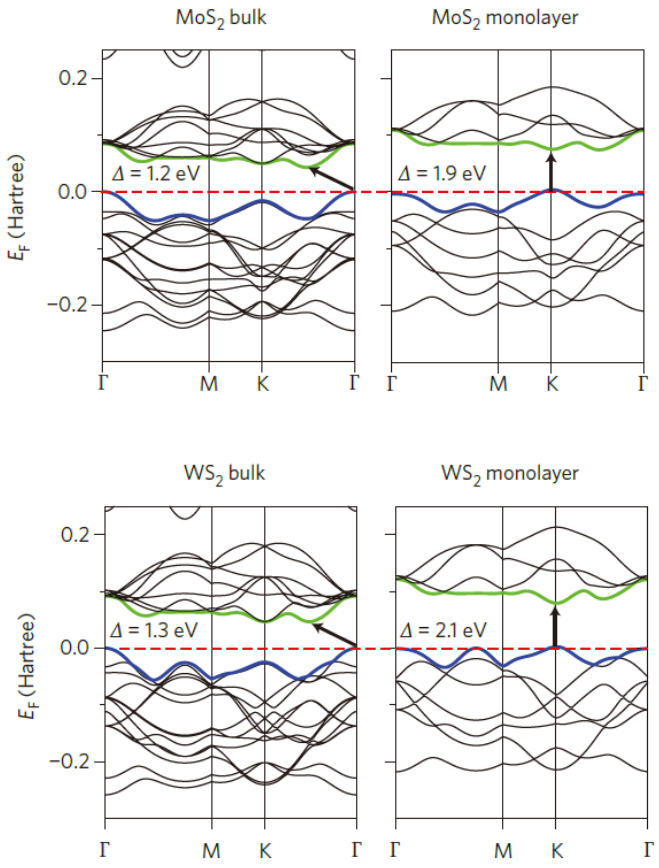

Figure 2.3 Band structures of bulk and monolayer MoS_2 and WS_2.[57, 58]

2.1.2 Synthesis Methods of TMDC Materials

One primary and significant area of TMDC research is the reliable manufacture of atomically thin 2D layers. To date, two main methods are used to acquire monolayer TMDCs: one is the top-down method including chemical[59, 60] and micro-mechanical exfoliation[61] from bulk materials; another is the bottom-up growth method by chemical vapor deposition (CVD) or MBE (Figure 2.4).[58] The former method is cost-effective and time-effective to get a high quality single layer or few-layer TMDCs. The material quality of the micro-mechanical exfoliated

monolayer TMDCs is usually higher than that of the bottom-up grown monolayer. Since fewer impurities are formed on the surface, it is more appropriate for fundamental materials examination and proof-of-concept device fabrication. However, the drawbacks are size limited, typically in the range of dozens of micrometers, and randomly distributed on a target substrate. In addition, there is no control in the final thickness of the TMDCs prepared by the micro-mechanical exfoliation method. Thus, it is not a suitable technique for production processes that requires a larger area format and more precise control over the film's thickness.[62-64]

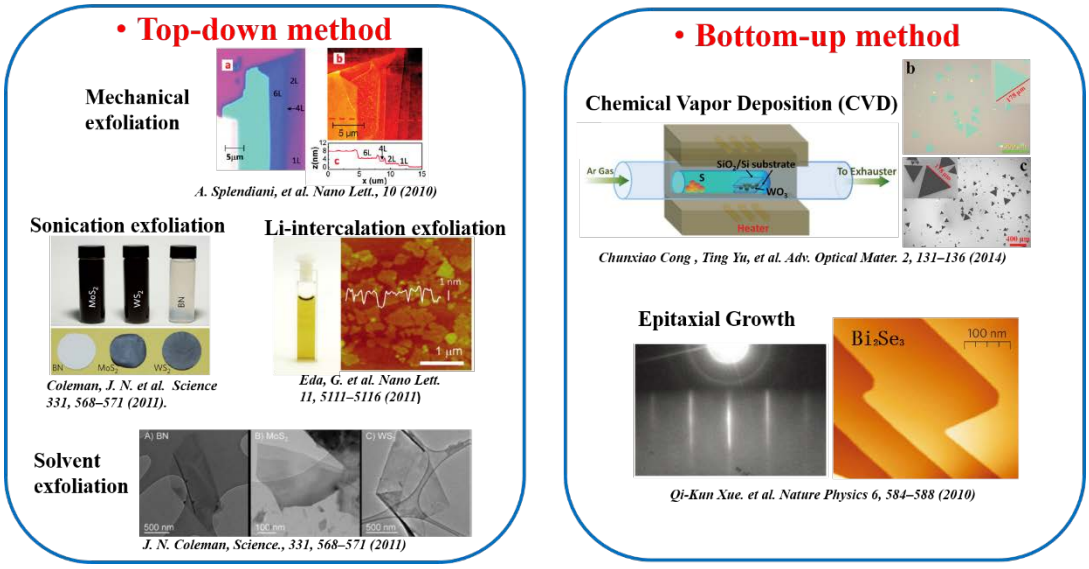

Figure 2.4 Two primary methods to acquire monolayer TMDCs: Top-down method and bottom-up method.

Top-down methods

The micro-mechanical exfoliation method introduced by Novoselov and

Geim[15] in 2004 is the most widely used technique to synthesize 2D materials because of its economical price and flexibility. This method is used to synthesize layered materials of thicknesses ranging from a monolayer to several layers of crystallite flakes, as well as maintaining excellent crystal quality. Scotch tape is employed in this straightforward process to exfoliate a monolayer (or a few layers) of graphene from the bulk of the graphite material. Then, the exfoliated graphene flakes are transferred to an arbitrary substrate, such as SiO_2/Si.[65, 66] Since the successful preparation of graphene layers by micro-mechanical exfoliation method, the technique has also been used for synthesizing other layered materials, such as TMDCs. Up to now, many reports have demonstrated the synthesis of WS_2, MoS_2, $MoSe_2$ and WSe_2 by using the micro-mechanical exfoliation method.[67-69] The exfoliated flakes are free from impurities, thereby making them suitable for fundamental material characterization and to fabricate proof-of-concept electronic devices. Unfortunately, this technique is not suitable for large-scale commercial manufacturing.

Another top-down method is sonication exfoliation in solvent, in which sonication is used to generate 2D micro flakes dispersed in a liquid solvent.[60, 70] The sonication energy as external power to generate 2D materials should be carefully adjusted to an appropriate level to exfoliate the bulk layered materials to a monolayer or few layered thin flakes.[71] Coleman *et al.* has reported that the sonication power and timing used during the dispersion process are the key factors to control product

quality.[72, 73] In the liquid exfoliation process, various kinds of organic solvents are used as dispersing solvents, according to the bulk layered materials. Several 2D materials have already been synthesized by employing the liquid exfoliation technique, such as $TaSe_2$, MoS_2, WS_2, $MoSe_2$.[72, 74]

Lithium intercalation is another method used to synthesize monolayer MoS_2 flakes. It is generally carried out by dipping the bulk layered materials into a butyllithium hexane liquid for several days in a flask filled with protective gas.[59] Through the intercalation of lithium ions among the $MoSe_2$ layers, the bulk layered materials can be exfoliated into single layers by hydration forces, thereby producing reliable MoS_2 monolayer flakes suspended in a liquid.[75, 76] Li_xMoSe_2 produced by this method can be collected by filtering and hexane is then used to remove excessive Li and organic residue.[77] The phase conversion caused by the intercalation could be reversed by thermal annealing to recover the semiconductor properties of the original $MoSe_2$. This is supported by the existence of the bandgap shown in the photoluminescence spectra.[78] Based on the reaction of $LiBH_4 + WS_2 \rightarrow LiWS_2 + 1/2B_2H_6 + 1/2H_2$, lithium intercalation was employed to produce WS_2 monolayer flakes by using $LiBH_4$.[79]

Bottom-up methods

For electronic and optoelectronic applications, large-area 2D materials are definitely significant for the large-scale manufacturing of flexible and transparent

electronic and optoelectronic devices. Chemical vapor deposition (CVD) is commonly thought as an efficient chemical reaction approach to grow large-area thin films.[80] The technique has been widely used to grow thin films of different varieties of materials including metals, semiconductors and insulators.[39, 40] Li *et al*.[81] were the first to use CVD to synthesize large-scale graphene 2D materials on copper at 1000˚C with methane as the precursor gas. CVD has also been used to grow large-scale 2D TMDCs.[82]

There are two routes to synthesize monolayer MoS_2 or WS_2 by CVD, as shown in Figure 2.5.[42, 47, 83] The first one is regarded as a two-step route in which pure metal or metal compounds are pre-deposited on the substrate and then sulfurized at a high temperature to form MoS_2 or WS_2, respectively.[84] The second route is considered a one-step growth, in which gaseous transition metal compounds and S sources are simultaneously introduced into a reactor to form MoS_2 or WS_2 on a substrate.[85, 86]

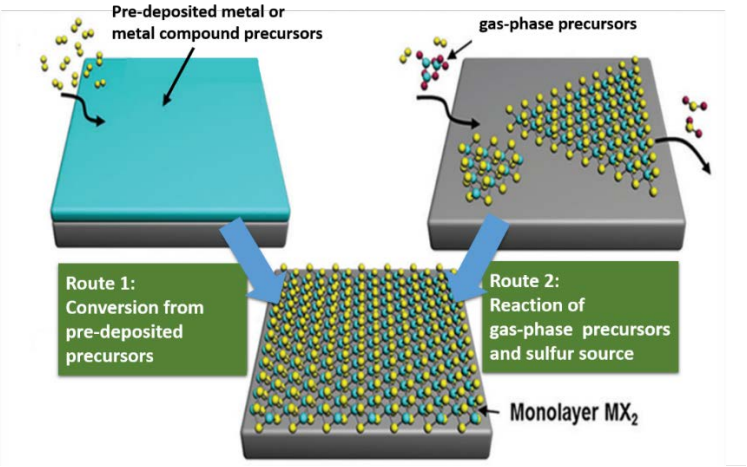

Figure 2.5 Two routes to synthesize monolayer MoS_2 or WS_2 by CVD. [87]

For the first route to synthesize MoS_2 or WS_2, transition metal oxide was the most widely used kind of precursor to react with the gaseous S to synthesize 2D TMDCs based on the reactions:[88, 89]

$$MoO_3(WO_3) + S(g) \rightarrow MoO_{3-x}(WO_{3-x}) + SO_x(g) \quad (2.1)$$

$$MoO_{3-x}(WO_{3-x}) + S(g) \rightarrow MoS_2(WS_2)(s) \quad (2.2)$$

During the CVD process, the MoO_3 or WO_3 was initially converted into MoO_{3-x} or WO_{3-x} at a high temperature, then it reacted with the gaseous S to form MoS_2 or WS_2. An advantage of using transition metal oxide precursors is that the reaction temperature of the transition metal oxide with the S source is commonly lower than when using pure metal precursors. The CVD method is suitable for manufacturing large-scale multilayer TMDCs, but producing monolayer TMDCs by precisely controlling the thickness on a monolayer scale is definitely a challenge.

2.1.3 Electronic and Optoelectronic Applications of TMDC Materials

The specific properties of 2D semiconducting TMDCs, including fewer dangling bonds, stable structure and high mobility, are the key advantages that make them competitive candidates for the channel layers of thin-film field-effect transistors (FETs).[90-92] P-type WSe_2 was the first of the TMDCs to be used as the channel material in an FET in 2004.[93] Soon after, the MoS_2 thin-film FET was fabricated in the back gate construction and its mobility reached 10 $cm^2V^{-1}s^{-1}$.[68, 94] The top

gate FET was also fabricated by using an n-type single layer MoS_2.[95] The mobility of the top gate MoS_2 FET was about 200 $cm^2V^{-1}s^{-1}$ and the on/off ratio was about 108. The p-type single layer WSe_2 flake was also used as channel material to fabricate the top gate transistor, and its mobility was about 250 $cm^2V^{-1}s^{-1}$. [67] The liquid exfoliation synthesized MoS_2 flakes are another alternative to fabricating flexible and transparent devices, and this method has been used to manufacture thin-film FET.[95] The development of the synthesis of large-area 2D TMDCs by using the CVD technique, as discussed above, created possibilities with regard to wafer-scale device fabrication. The construction of the top gate and back gate ultra-thin FET with TMDCs as the channel material is illustrated in Figure 2.6. The top gate construction enables a decreased gate voltage and integrates various kinds of devices on a single substrate. HfO_2 and Al_2O_3 are effective high-k dielectric materials that are usually employed in the single-layer MoS_2 and WS_2 FETs. [33, 96]

To fabricate flexible electronic and optoelectronic devices, like wearable displays and solar cells, different kinds of flexible and transparent materials including semiconductors, dielectrics and conductors are used as functional parts, such as optical absorbers, window layers and light emitters. Different 2D materials with diverse properties should be integrated in one substrate to realize a variety of different functions.[97-99] Graphene as a transparent conductor with high conductivity and very low absorption is a resourceful substitute for the primary transparent conducting material that is currently used.[100] In_2O_3/SnO_2 is indeed inflexible and increasingly

expensive due to a shortage of In.[101, 102] TMDCs as semiconductor materials with tunable bandgaps for visible light absorption are desirable alternative light absorption materials in traditional thin-film photovoltaic cells.[103] Phototransistors fabricated with a single layer of MoS_2 have the potential to become photodetectors.[104]

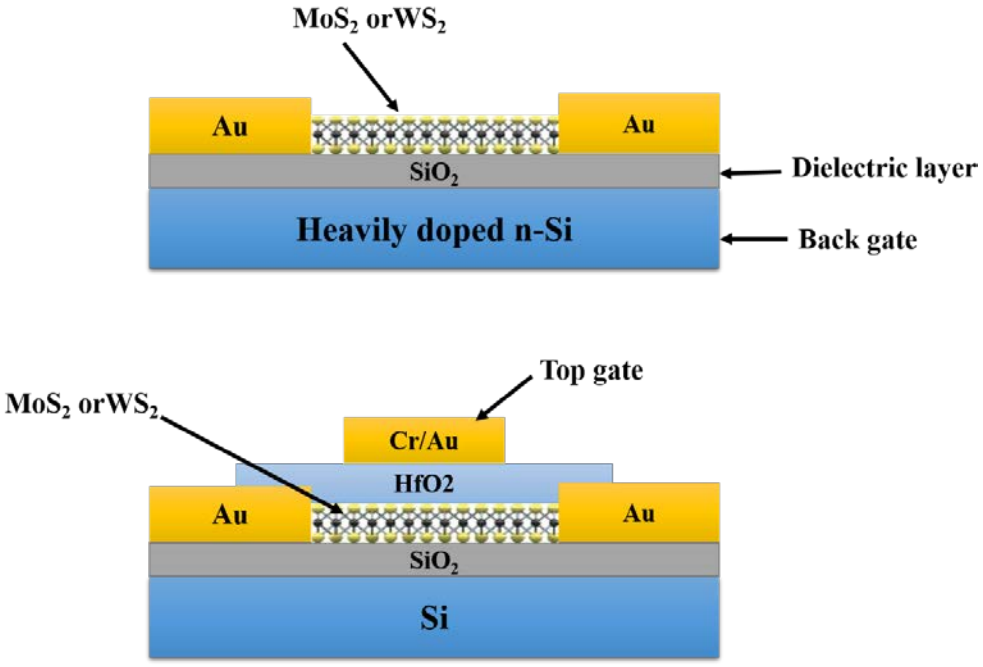

Figure 2.6 Illustration of the top gate and back gate ultra-thin FET with TMDCs as channel material.

2.2 Van der Waals Epitaxial Growth

2.2.1 Basic Concepts of Epitaxy

Epitaxy refers to the growth of a crystalline film on top of another crystalline substrate along a particular orientation decided by the crystal structure of the

substrate material.[105] During the epitaxy process, the gas or liquid molecule gets close to the substrate material and bonds to the vacant site of the substrate surface that serves as a seed crystal. A large number of molecules repeat this process to build layer upon layer at a particular orientation. If it forms a random orientation, it is called non-epitaxial growth. Epitaxy is a non-equilibrium process in which super saturation is the driving force to convert the gas or liquid phase material into the crystalline phase.[106] The flux can be written as:

$$J = k\sigma \tag{2.3}$$

where k is the coefficient of mass transportation and σ is the driving force that can be expressed by the partial differential of the chemical potential of the growth material in the liquid or gas phase.

$$\sigma = \Delta\mu \approx RT \ln(c/c_{eq}) \approx RT \ln(p/p_{eq}) \tag{2.4}$$

where $\mu_i = (\partial G/\partial n_i)_{p,T,...}$ is the chemical potential, c and p are the concentration and pressure of the growth material in the liquid or gas phase and c_{ep} and p_{ep} are the equilibrium concentration and pressure. The surface property of the substrate can influence the growth rate, and an exorbitant growth rate will lead to poor crystal quality. For most thin film applications, thin films do not have to be deposited by epitaxial growth. However, it is strongly preferred to grow semiconductor epitaxial films for electronic and optoelectronic applications.[107, 108]

If the epitaxial material and the substrate are the same material, the epitaxy process is referred to as homoepitaxy;[109] otherwise, it is called heteroepitaxy.[110]

For homoepitaxy, such as Si epitaxial growth on a Si substrate, the epitaxial layer is usually purer than the substrate material and the epitaxy material can be doped independently. For heteroepitaxy, the lattice mismatch will lead to a strained or relaxed growth. Such deviations will cause the change of electrical or optical properties of the epitaxial film. For the substrate selection, less lattice mismatch is desired to reduce defects and increase carrier mobility. Lattice mismatch may induce the epitaxial film to strain to match the lattice of the substrate to form pseudomorphic growth during the initial stage of the growth.[111] If strain accommodation is not possible due to the extent of the lattice mismatch, relaxed epitaxy will form due to the large dislocation stress and the film will keep its initial lattice structure on top of the substrate, as shown in Figure 2.7.[112, 113] For pseudomorphic growth, the initial epitaxial layer has the same lattice space as the substrate. However, as the thickness increases, a series of lattice misfits will occur due to the rising stress. The critical film thickness d_c can be expressed as:[114]

$$d_c = \frac{a_0(f)}{a_0(s) - a_0(f)} \cdot b/2 \tag{2.5}$$

where $a_0(f)$ and $a_0(s)$ are the lattice constants of the epitaxy film and growth substrate and b is the unit cell dimension of thin film.

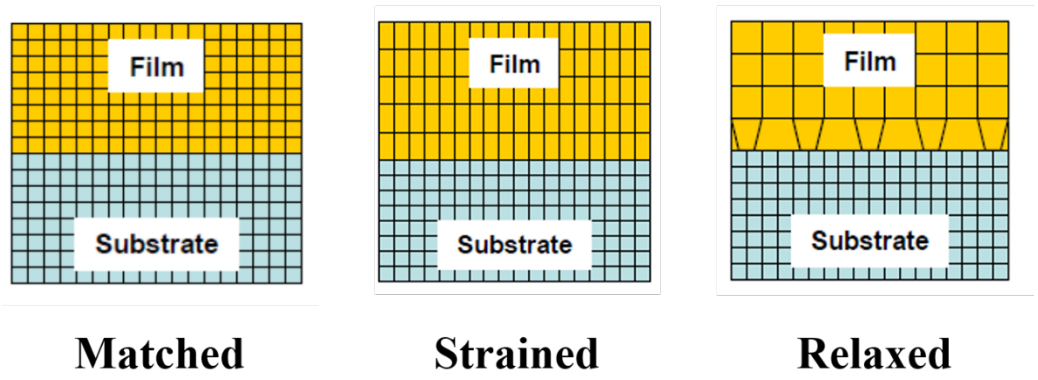

Figure 2.7 Schematic of the heteroepitaxy structure of matched, strained and relaxed lattices.[113]

Crystal defects not only result from large lattice mismatch but can also be caused by rapid cooling from a high temperature, or high-energy electrons striking the solid. According to dimension, the classification of crystal defects has three forms, which are point defects, line defects and planar defects, as shown in Figure 2.8,[115] which are important in terms of the electrical, optical and mechanical behavior of semiconductors. Point defects refer to a missing atom or its irregular placement in the crystal, including lattice vacancy, anti-site defect, interstitial and substitution atoms. Line defects, also called line dislocation, are groups of atoms arranged in irregular positions along a line. Planar defects are located at the grain boundaries of homogeneous regions or interfaces between different materials. Planar defects include grain boundaries and stacking faults. Grain boundaries are commonly derived from uneven growth during crystallization.[116]

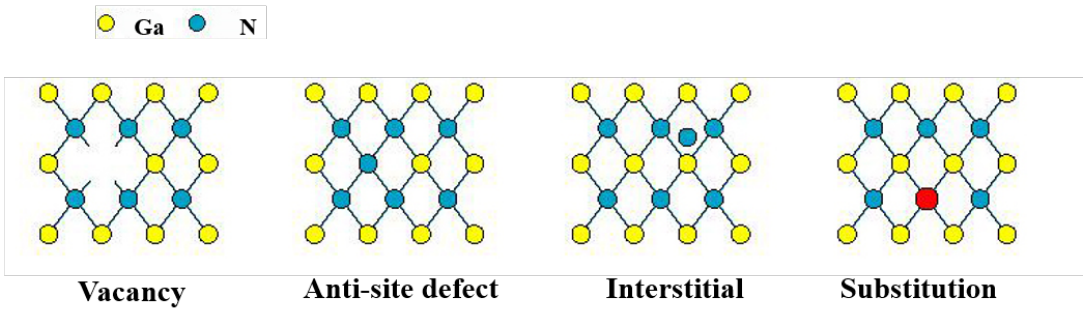

Figure 2.8 Schematic illustration of three types of crystal defects.

2.2.2 Molecular Beam Epitaxy

Molecular beam epitaxy is a thin-film deposition method in an ultra-high vacuum to deposit crystalline thin films with precise control over their composition, morphology and even monolayer thickness.[117] Since it was first used for depositing high quality semiconductor thin films in the 1970s,[118] MBE has become one of the most extensively used growth techniques for different kinds of materials, including oxides, metals and semiconductors. In the process of MBE, beams of molecules are evaporated in an ultra-high vacuum chamber toward the substrates where they can diffuse and finally form an epitaxial film. By exercising this precise control, the composition of the epitaxial film can be rapidly changed to make it possible to produce atomically abrupt crystal interfaces. This in turn helps producing a wide variety of unique structures consisting of quantum well structures, super-lattice devices, lasers, etc.[119] MBE structures are the nearest approximation to solid state physical models.

Figure 2.9 illustrates the schematic view of a MBE system, including a UHV chamber, substrate holder with a heating and rotating system, effusion cells, cryo panels and a surface analytical system, which commonly is a reflection high energy electron diffraction system (RHEED). The substrate is mounted on a holder facing the effusion cells with an internal system for substrate heating and rotating. Effusion cells are installed directly beneath the substrate and covered with mechanical shutters, which enable the molecular beams to be switched on and off. The heating system in

the effusion cells typically consists of a heating filament around the pyrolytic boron nitride (PBN) crucibles or electron beam heating. For electron beam evaporation, thermionic electrons are generated from a filament, accelerated by an electric field of a few kV, which pass through a confining magnetic field to trike the source material to evaporate it.

Different temperatures are required according to the melting point and vapor pressure of the materials used. For instance, the melting point of indium is only 156˚C, [120] but obtaining a suitable flux of indium requires temperatures above 700˚C due to the low vapor pressure at its melting point. Tungsten, with its very high melting point of 3422˚C,[121] can only be evaporated by the electron beam evaporation method. The cryo panels surrounding the effusion cells and the substrate holder force the beams to pass through a single path without being contaminated by other sources and keep the background pressure at a very low level, usually less than 10^{-9} torr.

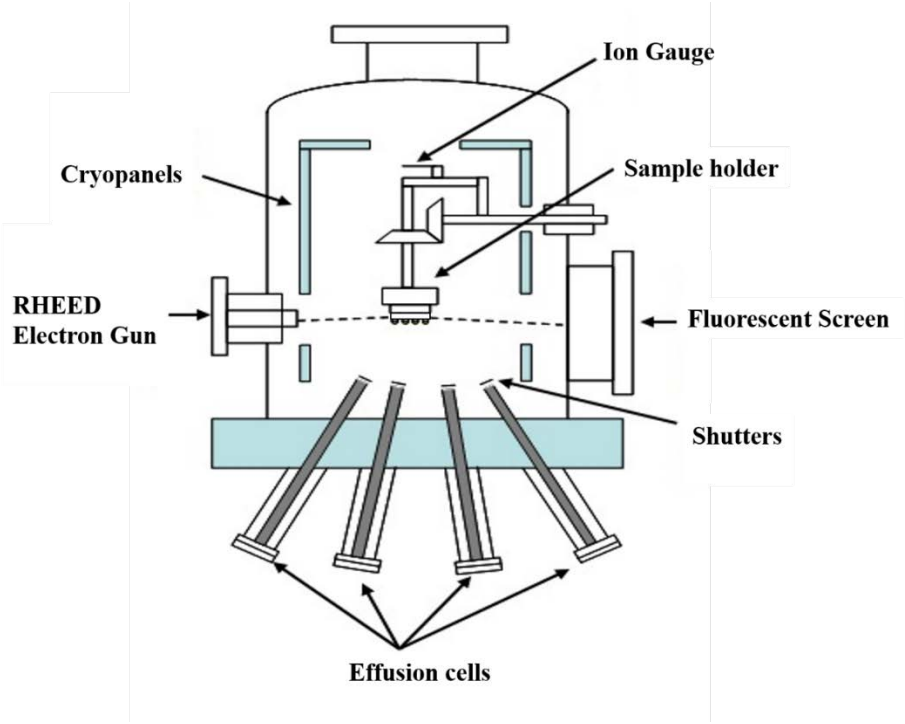

Figure 2.9 Schematic view of molecular beam epitaxy.

At a glancing incidence angle, the RHEED system provides the diffraction pattern to indicate the crystal ordering of the sample surface. Ultra-high vacuum is mandatory for the growth of high purity epitaxy films to avoid contamination that could affect the film morphology and electronic properties. Based on the kinetic gas theory, the flux F of gas molecules at the pressure P and temperature T on the unit area of surface is: [122]

$$F = \frac{P}{\sqrt{2\pi m k_B T}} \tag{2.6}$$

where m is the molecule mass and k is the Boltzmann constant. As an example, CO is considered the residual gas with a partial pressure of 10^{-8} torr at 300K, the arrival rate of CO can reach 3.2×10^{12} $cm^{-2}s^{-1}$. The number of atoms in a 1 cm^2 area

of the Si surface is about 3.2×10^{14}. If we assume that all CO molecules that arrive at the substrate can stick to the surface, then the residual gas would result in about 1% impurities in the epitaxy film, even in a high vacuum of 10^{-8} torr. Another constraint for reproducible epitaxial growth is the cleanliness of the substrate surface. The growth rate of MBE is commonly less than one monolayer per second. Impurities on the substrate surface can capture diffusing molecules to form nucleation islands during the slow MBE process. Assuming the sticking coefficient of residual gas is 1, then to maintain the arrival rate of the residual gas at one per million would require 10^{-12} torr vacuum pressure. Fortunately, many residual gases have sticking coefficients that are much lower than 1 for typical deposition temperatures, and the toleration of impurities for some kinds of semiconductor devices can be lower than 10^{-8} torr.

For a typical MBE growth process, there are four main steps, as illustrated in Figure 2.10. These include:[123, 124]

(1) Molecular beams are evaporated from the effusion cells towards substrates.

(2) The evaporated molecules are adsorbed on the substrate by van der Waals force, which is called physical adsorption, or form a chemical bond with the surface, which is called chemical adsorption.

(3) The adsorbed molecules diffuse to vacant sites and interact with the atoms of the surface. There are several different processes that can occur depending on the types of atoms, substrates and the temperature, such as diffusion along the

atomic step, diffusion along the edge, adsorption at the edge and desorption.

(4) Accumulated molecule islands merge into epitaxial layers.

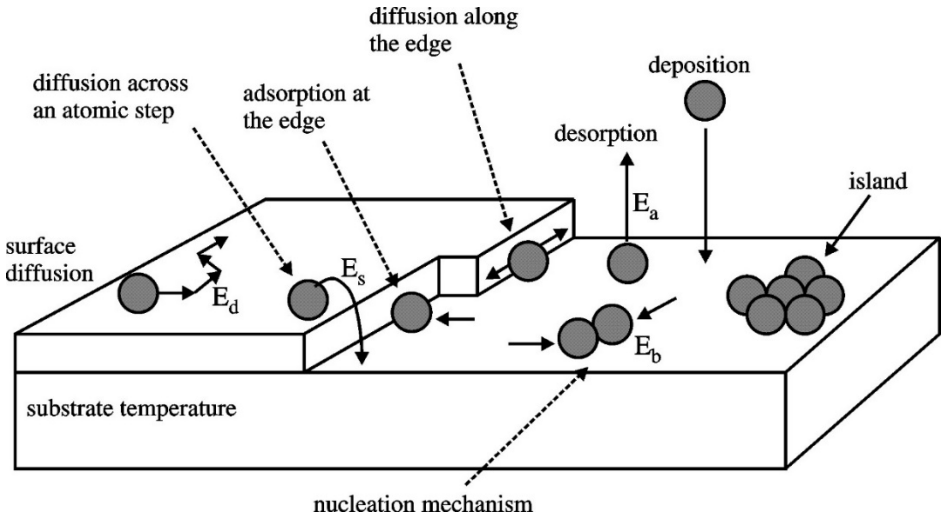

Figure 2.10 Behavior of atoms during the MBE process.[125]

Depending upon the growth conditions, three different growth modes can occur during the MBE process, as illustrated in Figure 2.11.[126]

(1) Layer-by-layer growth is also named as Frank–van der Merwe growth mode. Under the circumstance that the surface energy of substrate is greater than the sum of the surface energy of the film and the interface energy of the film and the substrate,[127] the growing layer reduces the surface energy, resulting in atoms preferentially attaching to free sites on the surface, and thus becoming atomically smooth.

(2) Island growth is also referred to as the Vollmer–Weber growth mode. Under the

circumstance that the surface energy of substrate is less than the sum of the film surface energy and the interface energy of the film and substrate,[128] the growing layer increases both the surface energy and the interface energy, resulting in the nucleation of molecules to form large islands.

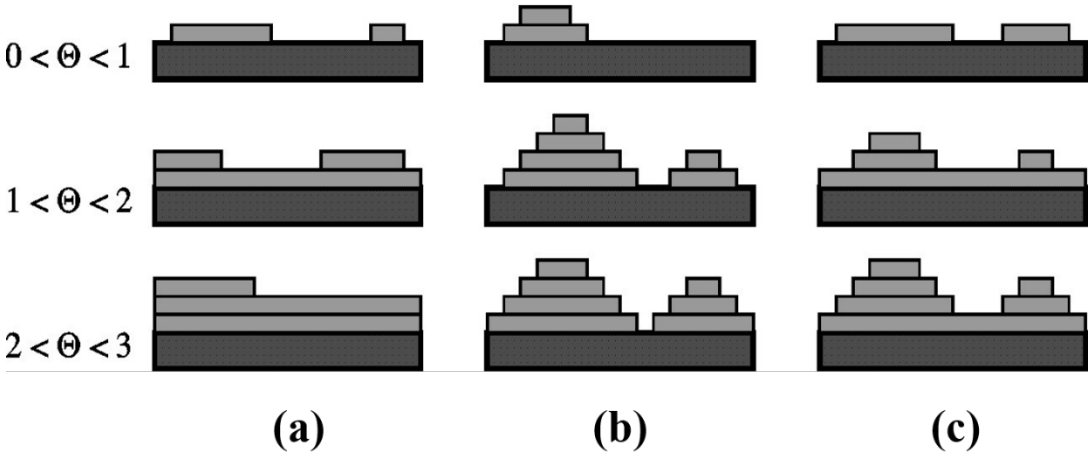

Figure 2.11 Schematic illustration of three epitaxy modes. (a) Layer-by-layer growth (Franck–van der Merwe mode); (b) Island growth (Vollmer–Weber mode); (c) Layer-by-layer followed by island (Stranski–Krastanov mode). Θ is the degree of monolayer coverage.[126]

(3) Layer-by-layer growth followed by island growth is also termed as Stranski–Krastanov growth mode. The substrate surface energy is greater than the sum of the surface energy of the film and the interface energy of the film and substrate at the initial stage, along with further growth, more lattice strain accumulated to induce that surface energy of the substrate is less than the sum of the film surface energy and the interface energy.[129] This mode is an intermediate mode including smooth layer growth at the beginning and subsequently followed by island growth. The change in equilibrium force

commonly originates from the lattice mismatch between the epitaxy film and substrates during the MBE process.

2.2.3 Van der Waals Epitaxy

Currently, good heteroepitaxy growth is only possible in a very limited combination of materials due to the lattice mismatch in most cases. Lattice matching is significant for both the growth material and the substrate, such as GaAs on Si. The presence of dangling bonds on the surface of the substrate is detrimental to the establishment of good heteroepitaxy. Layer materials, such as graphite, MoS_2, WS_2, and mica, with their 2D layer crystals combined with weak van der Waals force have no dangling bonds on the surface. Thus, an epitaxy layer on the surface that is free of dangling bonds will begin with its own constant lattice to keep the surface defects at a minimum level. In 1984, Koma *et al*. [130, 131] developed the heteroepitaxy growth of $NbSe_2$ on MoS_2 and this new kind of molecular beam epitaxy with weak van der Waals interaction was termed as van der Waals epitaxy (vdWE). Taking advantage of the weak van der Waals interaction, the lattice mismatch can be drastically relaxed, as shown in Figure 2.12a. It has been demonstrated that the lattice mismatch toleration of a thin film grown by the van der Waals epitaxy technique can reach as much as 50%.[132] Therefore, the van der Waals epitaxy allows for a great variety of different heterostructures.

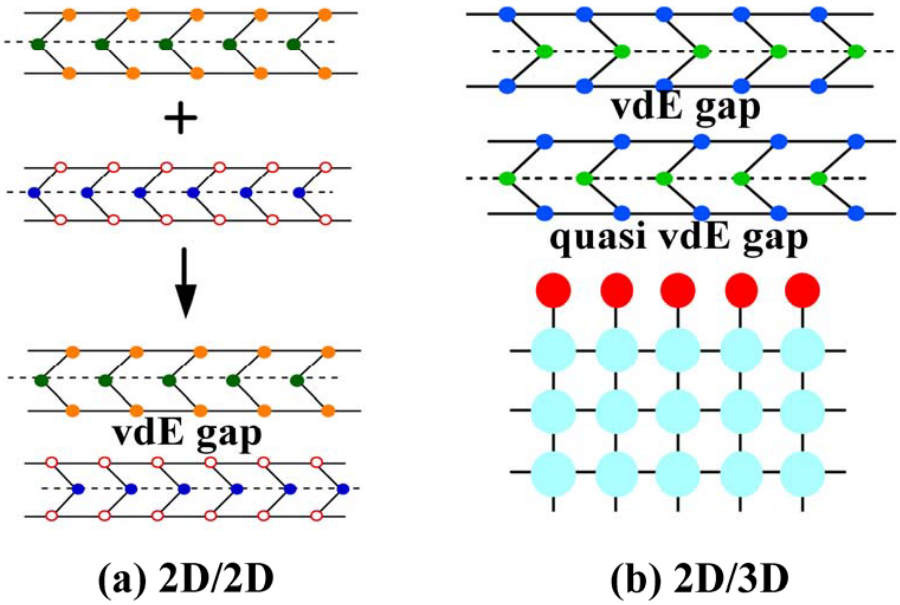

Figure 2.12 Schematic drawing of van der Waals epitaxy and quasi-van der Waals epitaxy.[130, 132]

The van der Waals epitaxy method can be applied to a three-dimensional (3D) substrate by passivating the dangling bonds on the flat surface of the 3D material, known as quasi-van der Waals epitaxy, as shown in Figure 2.12b. For instance, $(NH_4)_2S$ passivized GaAs(111) has been used as a van der Waals epitaxy substrate for $MoSe_2$ and $NbSe_2$ thin film growth,[133] and high quality GaSe film was proven to be grown on a hydrogen passivated Si substrate.[134] In addition, some organic epitaxial layers have been grown by utilizing the van der Waals epitaxy, such as Cu-phthalocyanine grown on a cleaved surface of MoS_2.[135] In conclusion, van der Waals epitaxy effectively reduces the lattice mismatch of the epitaxy layer on different substrates. This widens the scope for material selection to fabricate

heterostructures for the innovation of novel devices.[130]

2.3 Chemical Vapor Deposition

2.3.1 Basic Concepts of Chemical Vapor Deposition

Chemical vapor deposition (CVD) is a solid growth method achieved through the reaction of gaseous materials.[136] Depending on the type of reactants, the pressure range or the use of equipment with an enhanced activation system, there are several variants of CVD, such as ultra-high vacuum chemical vapor deposition (UHV-CVD),[137] metal organic chemical vapor deposition (MOCVD),[138] plasma-enhanced chemical vapor deposition (PECVD),[139] hybrid physical-chemical vapor deposition (HPCVD), etc.[140] CVD has various advantages including: 1) The reaction can selectively occur in certain regions of the substrate; 2) The CVD method is more easily used to cover a rough surface or the vertical sidewalls of the substrate than some physical vapor deposition methods, like thermal evaporation; 3) The gaseous materials used in the CVD process that flow into the reaction chamber can be stored in external reservoirs to prevent contaminating the growth chamber when refilling it with new materials; 4) CVD usually does not require very a high vacuum; and 5) CVD is commonly used to produce larger batches than thermal evaporation.

In CVD, source materials are delivered as volatile gases, known as precursors,

to deposit thin films through a series of chemical reactions of different precursors and substrates. These reactions can occur both in the reaction chamber and on the surface of the substrate. Gaseous precursors are commonly diluted in a carrier gas to deliver the gaseous precursors to the reaction region. The typical carrier gases used in the CVD process are nitrogen, argon, hydrogen, or mixtures of the three. The temperature for the CVD process ranges from room temperature to 2000˚C. If reactions require higher energy, a plasma can be utilized to generate the radicals and ions reaction by electron strike collisions to activate the chemical during reaction, which are called as plasma-enhanced chemical vapor deposition (PECVD).[139]

2.3.2 Kinetics of Chemical Vapor Deposition

A normal CVD process involves a series of reactions, as shown in Figure 2.13.[141] The mass-transport mechanism is particularly important because the reactions involved in the CVD process determine the growth rate and the design of the CVD system. The sources, in the form of gas, pass through the pipes and valves to the reaction chambers to change state from a gas to a solid at a certain temperature and under a certain amount of pressure. In some cases, reactions may occur before arrival at the substrate when the sources are still in their gaseous state. The steps involved in the CVD process are summarized as follows:[142, 143]

(1) Gaseous sources are brought to the reaction zone by the carrier gas;

(2) Gaseous sources diffuse through the boundary layer;

(3) Reactants move to the surface of the substrate;

(4) Physical absorption and chemical reaction occur on the surface of the substrate;

(5) Surface reactions occur for thin film deposition;

(6) Desorption of gaseous by-products; and

(7) Gaseous by-products diffuse away from the reaction zone.

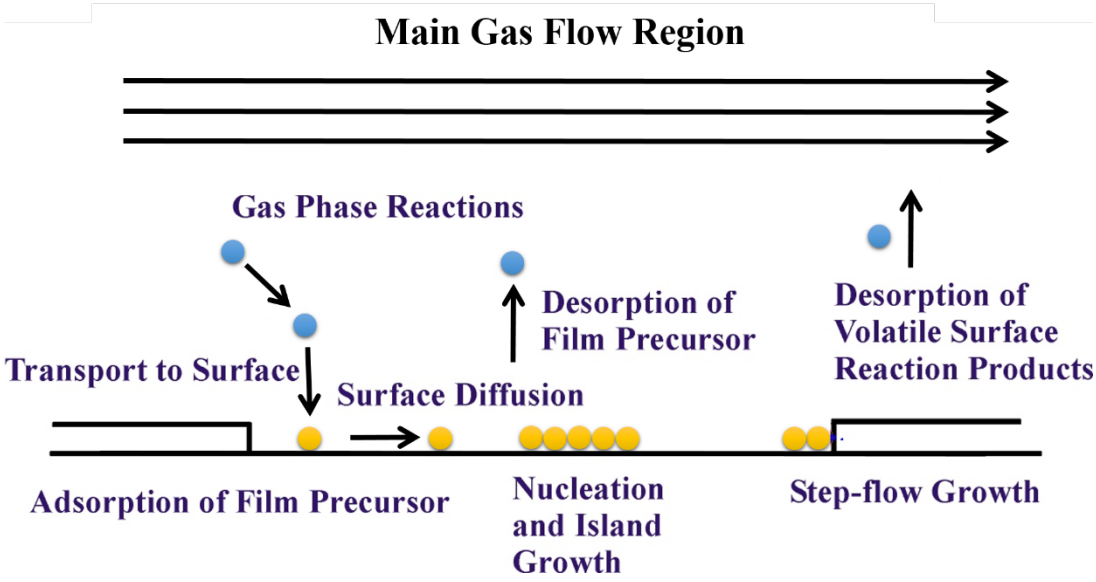

Figure 2.13 Schematic illustration of types of chemical reactions in the CVD process.[141]

These steps take place in order and the slowest step determines the growth rate. The behavior of gas flow in the CVD chamber is described and characterized by fluid mechanics and the Reynolds number, R_e , a dimensionless parameter.[144] The gas flow is usually regarded as laminar. Based on fluid dynamics, a boundary layer of the gaseous mixture, also called a stagnant layer, develops in the reaction zone over the

surface of substrate. The gas flow velocity near the inner wall of the reaction zone is almost zero. The boundary is the area from the edge of the wall to the center where the velocity of the gas flow changes from zero to a stable level, as shown in Figure 2.14. The boundary layer thickness is expressed as:[136]

$$T_{boundary\ layer} = \sqrt{\frac{x}{R_e}} \tag{2.7}$$

$$R_e = \frac{\rho u_x}{\mu} \tag{2.8}$$

where ρ is the mass density, u_x is the flow density, x is the distance of flow from the inlet position and μ is the viscosity.

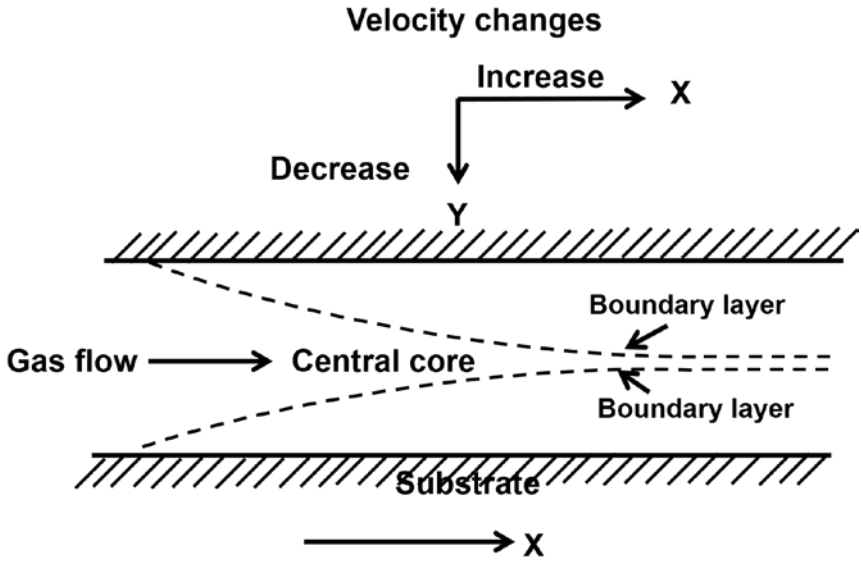

Figure 2.14 Schematic drawing of the boundary layer
and the velocity changes in a tube reactor.[145]

This indicates that a lower gas flow and a longer distance from the inlet will

increase the boundary layer thickness. The adsorption mode significantly depends on the chemical properties of the source materials or the precursors pre-deposited on the substrate. Source molecules can adsorb on the substrate surface though weak physical adsorption. If there is enough chemical coordination between source materials or the precursor pre-deposited on the substrate, stronger chemical adsorption is achievable for a longer period of adsorption. Some adsorbate molecules or fragments, such as dissociative chemical adsorbates, can react rapidly on the substrate surface due to the weak original chemical bonds. Adsorbate molecules or fragments can diffuse along the sample surface, some chemical sites or layer steps for their reaction. Generally, surface diffusion is a necessary process for the eventual formation of the thin film. Locating optimal adsorption sites through diffusion is critical to grow high quality crystalline films that would ultimately determine the performance of an electronic device.

There are two main limitations to the reaction rate of the CVD process: gas transport limitation and surface reaction rate limitation.[145, 146] Gaseous source concentration in the carrier gas and gas flow viscosity are two decisive factors in the gas transport limitation, while the surface reaction rate limitation relys on the physical and chemical adsorption rate, the reaction mechanism and the deposition temperature. The entire rate of a CVD process considering these two primary limitations could be expressed as:[146]

$$\boldsymbol{R} = \frac{\boldsymbol{C_g}}{\boldsymbol{N_s}} \frac{\boldsymbol{k_f h_g}}{\boldsymbol{k_f + h_g}} \tag{2.9}$$

$$k_f = k_0 e^{-\Delta H / k_B T} \tag{2.10}$$

where C_g is the concentration of the most rate limited gaseous source, k_f is the surface reaction rate, h_g is the gas transport rate and N_s is the atom concentration in the solid form of the most limited gaseous source. The net rate limited by surface reaction and gas transport in Equation 2.9 as a function of inverse temperature is shown in Figure 2.15.

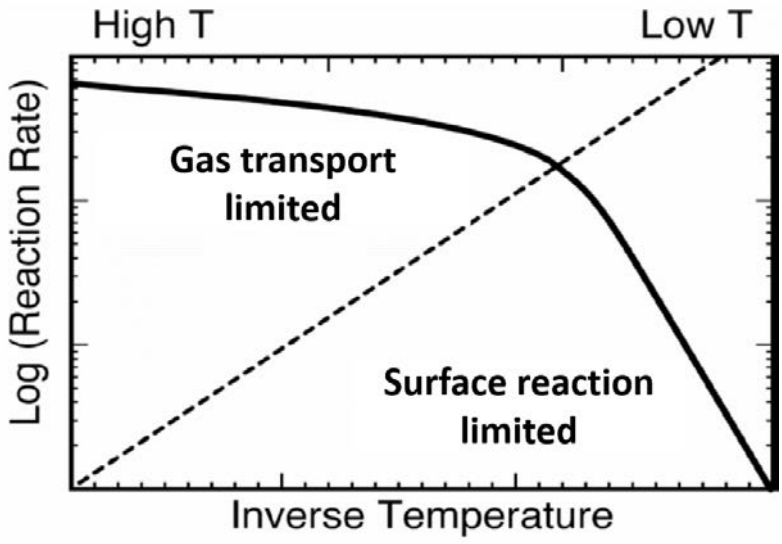

Figure 2.15 The net rate limited by surface reaction and gas transport with inverse temperature (solid line).[146]

In most cases, source materials undergo chemical reactions in the gas phase leading to the production of more reactive molecular fragments.[147] This process can be activated thermally or by external energy, such as a plasma. In general, these more reactive molecular fragments are part of the original molecule, or are even radicals or ions when applying plasma to activate the chemical reaction. It should be

noted that most CVD processes are carried out at a low pressure, enabling a substantial lifetime for most reactive molecular fragments in comparison to many other chemical reaction circumstances, such as a liquid solution. Hydrogen, as a typical kind of carrier gas, usually participates in the gas phase reactions, while nitrogen and argon may also take part in the reactions in the plasma activation CVD process.[148]

2.3.3 Chemical Vapor Deposition System

The various reaction types and different deposition rates result in distinctively designed CVD systems. It is necessary to take the design of the CVD system into the consideration of the thin film growth. A typical CVD system includes source material reservoirs, gas flow controllers, a reaction tube, heating system, pumping system to remove by-products and residual sources, and a safety system to detect toxic gases, as shown in Figure 2.16.[149]

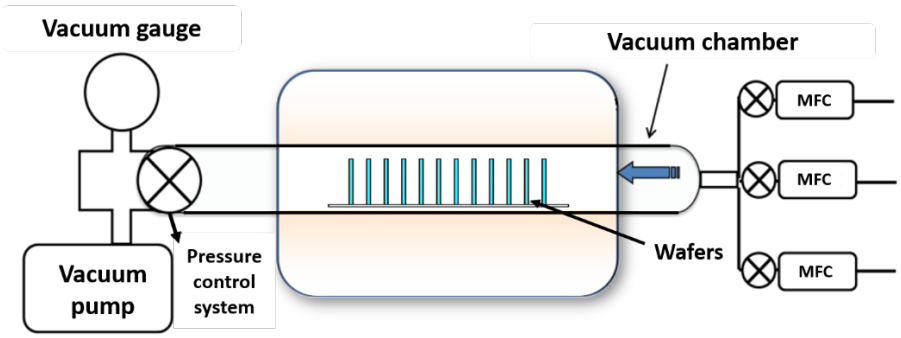

Figure 2.16 Schematic drawing of a typical CVD system.[149]

The flow of gaseous sources into the reaction zone should be carefully monitored to control the stoichiometry and the deposition rate. Source materials delivery is quite critical because the flow rate could determine whether or not the deposition takes place in some cases. For low vapor pressure source materials, the pipes and valves through which gas flows are required to be heated to avoid the condensation of the source material. A mass flow controller (MFC) is commonly used to precisely gauge and control gas flows. An MFC is designed and calibrated to measure and control one or several types of gas in a certain range of flow rate.

There are two classes of CVD systems based on whether they are operating at a low pressure (LPCVD) or atmosphere pressure (APCVD).[150, 151] APCVD is easy to realize since it does not need a vacuum system. APCVD yields a high growth rate due to its high reactant concentration at low temperatures. However, its deposition coverage is not usually as uniform as LPCVD, and powders are likely to form during the deposition process. Thus, for most electronic and optical electronic materials, the reactor configurations are LPCVD, since this can provide outstanding uniformity on rough surfaces and deliver high purity deposition. The low pressure results in a low deposition rate and requires a higher temperature; both of these are necessary for high quality thin film growth.

For thermal CVD systems, a resistive heating system or a radio frequency induced heating system is required to obtain a high temperature to activate the

chemical reaction. Up to 2000˚C may be necessary to decompose some source materials. There are two primary types of thermal CVD reactors based on the substrate heating methods, the hot wall reactor and the cold wall reactor, as shown in Figure 2.17.[146]

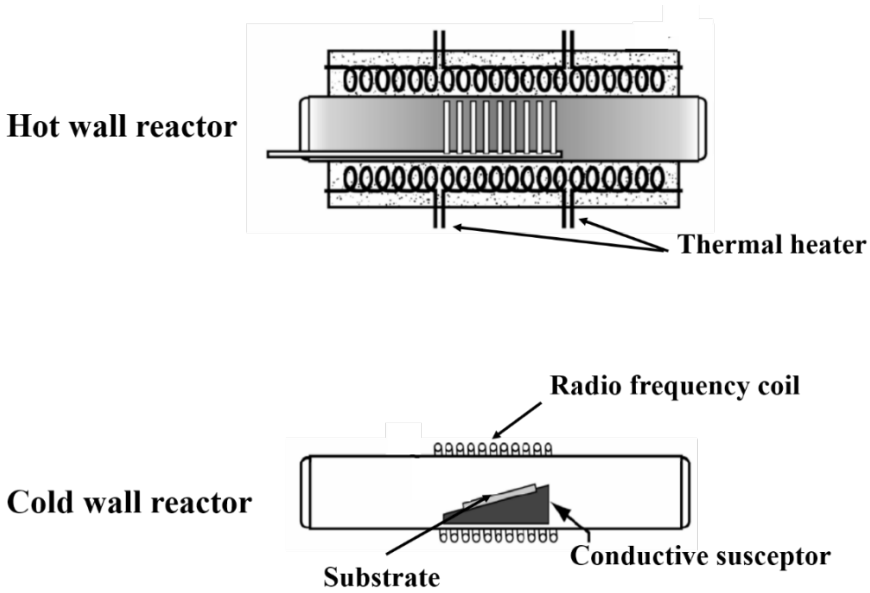

Figure 2.17 Schematic illustration of the hot wall and the cold wall reactors.[146]

The hot wall reactor tube is placed in an isothermal furnace. Hot wall reactors are usually large, and a number of substrates can be deposited at a time. The temperature can be precisely controlled as the whole chamber is heated, which permits superior temperature uniformity for a large number of substrate depositions. However, a disadvantage of the hot wall reactor is that depositions take place not only on the substrate but also on the chamber wall. Moreover, the fragments released from

the chamber wall during the cooling down process may contaminate the sample surface. In the cold wall reactor, only the substrate is heated. The most common configuration of a cold wall reactor is to mount the substrate on a conductive holder, such as graphite or Cu, and wrap the tube reactor with radio frequency coils. The conductive holder can absorb the radio frequency energy to generate heat and transport it to the mounted substrate, thus deposition is limited to the substrate. Because deposition only occurs on the substrate, the depletion of source materials is reduced, and without condensation on the reactor wall, the reactor wall is relatively clean, thus preventing the contamination of fragments released from the wall. The substrate holder in the cold wall reactor commonly has small thermal mass, so the temperature rising and falling occurs much more rapidly to prevent the overreaction of some high activity source materials. The most important issue with thermal CVD reactors is to maintain a uniform temperature throughout the wafer to prevent the creation of non-uniform thickness as the growth rate strongly depends on temperature, especially in LPCVD.

Plasma-enhanced CVD (PECVD), also known as plasma-assisted CVD (PACVD), uses plasma to activate reactions at a much lower temperature in comparison to thermal CVD. For instance, the deposition of Si_3N_4 thin film in thermal CVD requires a temperature of between 700˚C and 900˚C, while in a PECVD system, reactions can occur at a much lower temperature of 300˚C.[152] Most plasmas used in a CVD system is generated by a radio frequency field. The energy distribution of

the electrons and ions in plasma gas is commonly in the range of 0.1 eV to 2.0 eV,[153] which is adequate to excite molecules to higher activity energy or break chemical bonds through collision. The reactive species produced in collisions have much lower energy barriers for chemical reactions than their parent molecules and significantly reduce the reaction temperature. In addition, the reactive species commonly have higher stick coefficients to the substrate; hence, the PECVD reactions are dominated by the plasma-generated reactive species on the substrate surface instead of the parent molecules. A typical PECVD is shown in Figure 2.18.[154]

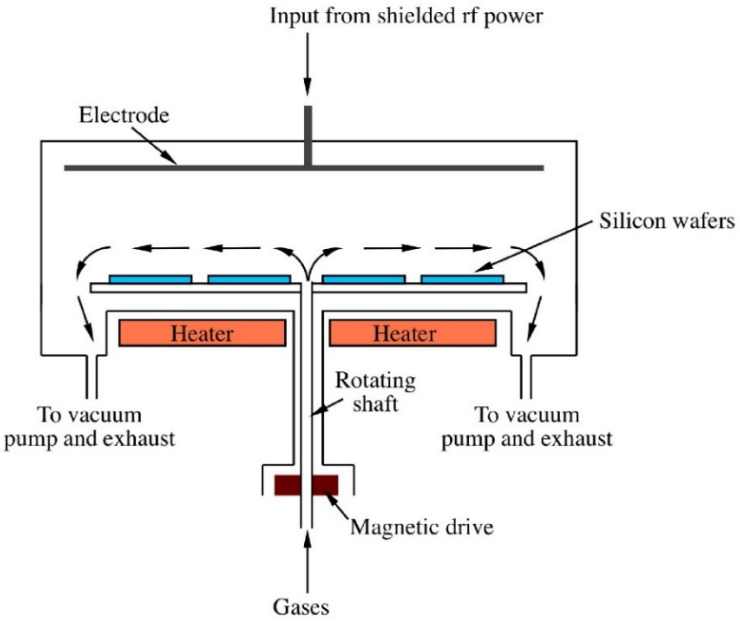

Figure 2.18 Schematic drawing of plasma-enhanced CVD system.[154]

The wafers are located at the ground potential electrode. Gases used for plasma generation are introduced from the center of the holder and pumped out from the

edges or vice versa. The gases can also be introduced from evenly distributed small holes in the upper electrode to achieve more uniform plasma distribution. The magnetic drive is used to rotate the wafer holder during the CVD process to obtain a more uniform deposition. PECVDs are favored in large-scale industrial production due to their reduced deposition temperature and higher productivity.

2.4 Objectives of the Thesis

In this thesis, high quality WS_2 thin films were grown on different substrates, including mica and sapphire, by molecular beam epitaxy, which is based on the van der Waals epitaxy, and the chemical vapor deposition method. Making use of WS_2 thin films, WS_2/GaN p-n junctions and WS_2 thin-film FET were fabricated. The objectives of the thesis are listed as follows:

(1) Synthesize high quality WS_2 thin films on mica and sapphire substrates by MBE and the CVD methods. Film quality is one of the most important factors impacting the performance of WS_2-based electronic devices. The relationship between the growth conditions and the phase compositions, crystal structure and electron properties of WS_2 thin films needs to be systematically studied. Micron-sized WS_2 layered materials obtained through mechanical exfoliation method is only suited to basic investigation and proof-of-concept device fabrication, and is not suitable for large-scale commercial manufacturing. However, MBE and CVD can be used to grow high quality large-area uniform

WS_2 thin films.

(2) Explore the growth mechanism of the crystal structure of WS_2 thin films. WS_2 commonly exists in a mixture of type-I and type-II crystallites with their *c* axis perpendicular or parallel to the substrate surface. Large layered type-II WS_2 crystals are necessary for the fabrication of WS_2-based electronic devices. A thin Ni layer has been used as a texture promoter to grow large layered type-II WS_2 crystals. The liquid NiS_x formed during the growth process could serve as the nucleation seed for liquid epitaxy, which leads to the horizontal growth of WS_2 crystals.

(3) Fabricate WS_2/GaN p-n junctions via the wafer-scale etching-free transfer method. Most semiconductors and conductors are not stable enough for the high temperature growth of WS_2. To overcome this constraint, the transfer method to fabricate WS_2-based heterojunctions by transferring the WS_2 thin film from the sapphire substrate to arbitrary flat substrates needs to be developed. The use of chemical etchants such as HF or KOH that can contaminate or damage the surface of the film resulting in degradations of device performance should be avoided in the transfer method.

(4) Fabricate WS_2 field-effect transistors using thin WS_2 layer as channel material. The specific properties of semiconducting WS_2 thin film, including fewer dangling bonds, chemical stability and high mobility, make it a potential option for the channel layer for thin-film FETs. Additionally, horizontal layered type-

II WS_2 crystals can serve as high-speed channels to transport electrons for the fabrication of ultra-thin FETs.

CHAPTER 3 CHARACTERIZATION TECHNIQUES

3.1 X-ray Diffraction

3.1.1 Basic Principles

X-ray diffraction (XRD) is one of the most widely used non-destructive techniques for determining the crystal properties of materials, such as the crystal structure, phase, orientation, average particle size and crystallinity.[155] X-ray diffraction peaks are generated by the monochromatic interference of diffraction at a specific angle based on Bragg's law, which is indicated by Equation 3.1

$$n\lambda = 2d_{hkl}\sin\theta \tag{3.1}$$

where d_{hkl} is the equivalent distance of the periodic crystal planes, and θ is the angle between the incident beam and the parallel crystal planes.[156] If the difference of the optical paths between adjacent X-ray diffraction is equal to an integral multiple of the wavelength (λ) to meet Bragg's law, then constructive interference occurs. The peak intensity and distribution are determined by the periodic arrangement of atoms in the crystal lattice. Therefore, XRD patterns become the fingerprints of different materials. Comparing an XRD pattern with a standard database can quickly identify a large number of different crystalline samples.

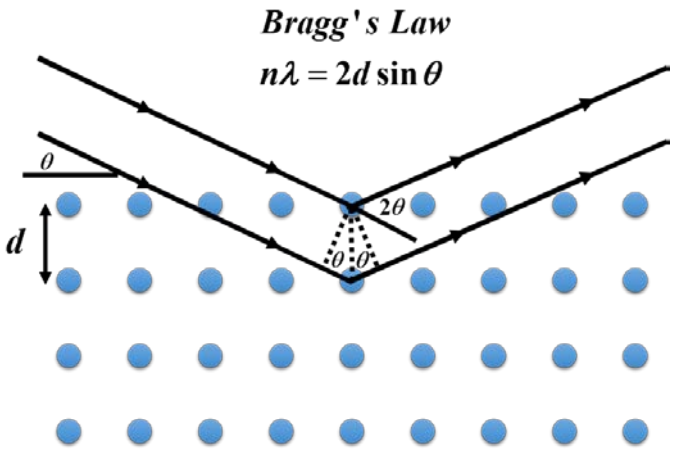

Figure 3.1 X-ray diffraction based on Bragg's law.

An X-ray diffraction instrument contains three major components, including an X-ray generation tube, a sample holder and a detector, as shown in Figure 3.2. The electrons escape from a heated filament and accelerate through a high-voltage field towards a metal target. When the electrons strike the target atoms, the inner shell electrons of the target atoms gain sufficient energy to escape to the outer shell and the X-ray is generated. The X-ray spectra comprise several components. K_α and K_β are the primary portions of the X-ray spectra and K_α comprises $K_\alpha 1$ and $K_\alpha 2$. Different target materials, such as Cu, Al and Mo, have unique sets of characteristic wavelengths. By filtering with Ni foil and crystal monochromators, the monochromatic X-ray necessary for diffraction is obtained. Cu is the most widely used target material with $K_\alpha 1$ and $K_\alpha 2$ wavelengths of 1.541Å and 1.544Å, respectively. The monochromatic X-ray extracted from the X-ray tube is pointed at the sample and reflected into the detector. The detector rotates with the sample to record the intensity of the reflected X-ray. When the incident angle of the X-ray to

the sample meets Bragg's law, constructive interference occurs and is recorded as a peak.

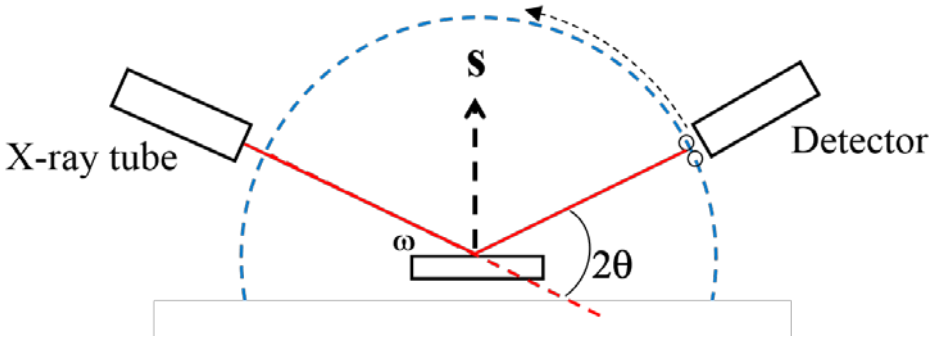

Figure 3.2 Schematic illustration of the X-ray diffraction system.

3.1.2 Scan Modes of Operation

The X-ray diffraction system can be used to analyze both the powder and thin film of crystalline material. For thin film characterization, three different types of scan—θ-2θ scan, ω scan (rocking curve) and phi-scan—are commonly used to investigate thin film properties, such as crystallite size, orientation and lattice strain. The working principles of these three scan types will be introduced in the following section.

θ-2θ Scan

In the θ-2θ scan, θ is the angle between the incident X-ray beam and the substrate surface. The angle between the detector and incident X-ray is 2θ. In this type of scan,

keeping the X-ray beam fixed, while the sample rotates at an angle of θ, and the detector rotates at an angle of 2θ simultaneously to detect the reflected signal, as illustrated in Figure 3.3. For polycrystalline thin films, several sets of peaks can be detected due to the mixture of different crystal orientations. For a single crystal film with its crystal planes parallel to the sample surface, θ equals the angle between the incident X-ray and the crystal planes ω, which is specifically referred to as the ω-2θ scan.

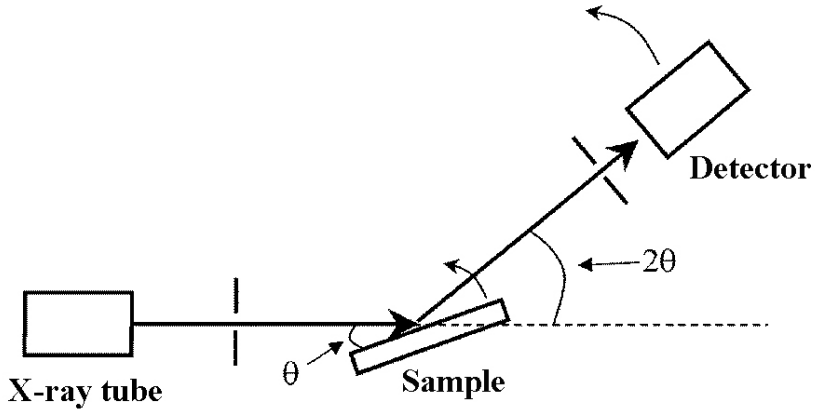

Figure 3.3 Schematic of a ω-2θ scan.

Rocking Curve

Another kind of scan is a ω scan, which is also referred to as a rocking curve scan. In the operation of the rocking curve scan, the X-ray beam and the detector are set at a specific Bragg angle, then the sample is tilted around its equilibrium position. The rocking curve is primarily used to evaluate the crystal quality of an imperfect

crystal and yields a quantitative value.[157] The widening of the full width at half maximum (FWHM), the width of a spectrum peak at the half maximum value, mainly results from the existence of defects and various imperfections in the crystal, such as misorientation and dislocation. An ideal crystal would give an extremely sharp peak.

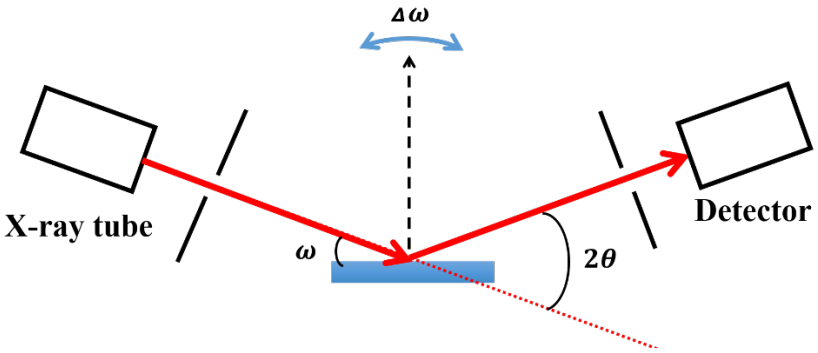

Figure 3.4 Schematic of ω scan.

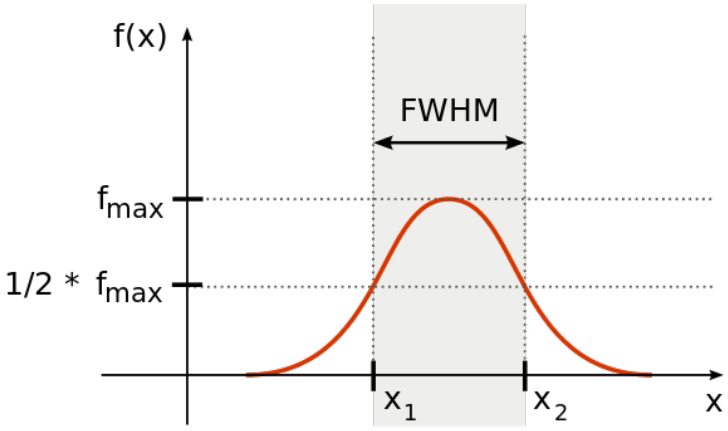

Figure 3.5 Illustration of the full width at half maximum (FWHM).

Phi-scan

Both the θ-2θ scan and the ω scan are referred to as out-of-plane techniques and only provide the orientation information of the crystal planes parallel to the sample surface. Phi-scan provides the orientation information of the crystal planes not parallel to the surface of sample and is referred to as an in-plane technique. Combining the out-of-plane and the in-plane techniques can provide more intuitive orientation information than conventional asymmetric reflection methods.

During the phi-scan measurement, the X-ray beam and detector are set at a specific Bragg angle, then the sample is tilted at an angle of χ relative to the reflection vector and rotated along the ϕ axis from 0° to 360° to get the in-plane symmetry information of the crystal sample, as shown in Figure 3.6. A typical phi-scan XRD pattern, which contains a set of peaks in equal intervals, reveals the specific symmetrical characteristics of crystal samples. For example, four peaks indicate four-fold symmetry, whilst six peaks may result from six-fold symmetry in a hexagonal crystal structure.

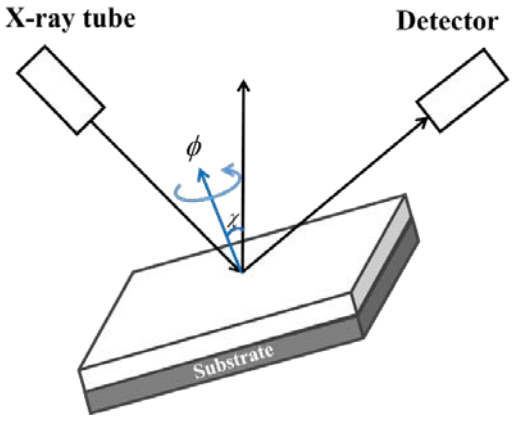

Figure 3.6 Schematic of a phi-scan.

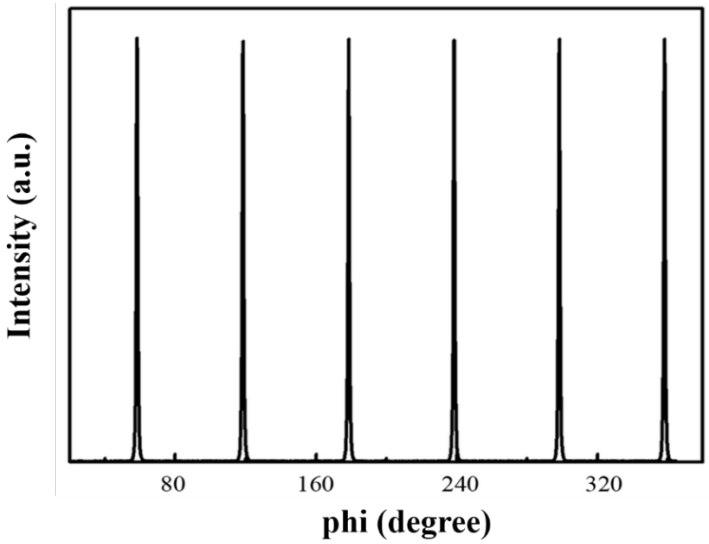

Figure 3.7 A typical phi-scan XRD pattern.

3.2 Raman Spectroscopy

3.2.1 Basic Principles

Raman spectroscopy is one of the essential techniques used in the investigation of the rotational and vibrational spectra of atoms or molecules inside a material. This method is based on the Raman effect, the inelastic scattering of incident light by atoms or molecules, which was observed by C. V. Raman in 1928.[158] When a sample is irradiated with a laser, the re-emitted light has the same wavelength as the incident laser, which is termed elastic scattering, or Rayleigh scattering. However, a very small portion (about 10^{-6} times) of the scattered light has the frequency shifted from the incident laser due to the vibration and rotation of atoms or molecules. This frequency-shifted scattering process is known as inelastic scattering, or Raman scattering.

Without consideration of the molecular vibration and rotation, when an incident light with the frequency of ν_0 and the periodical electric field of $E = E_0 \cos(2\pi\nu_0 t)$ hits a molecule, a dipole moment is stimulated with the same frequency ν_0. The dipole moment μ can be expressed as:

$$\mu = \alpha E_0 \cos(2\pi\nu_0 t) \tag{3.2}$$

The polarizability α of the molecule changes as a function of the displacement $\boldsymbol{R}$ of the vibration of atoms from the equilibrium position, which can be expanded as:

$$\alpha(R) = \alpha(R_0) + \frac{d\alpha}{dR}(R - R_0) + \textit{higher order terms} \tag{3.3}$$

$\boldsymbol{R}$ is time dependent and can be written as:

$$R = R_0 q \cos(2\pi\nu_{vib} t) \tag{3.4}$$

where ν_{vib} is the amplitude modulation frequency induced by the dipole moment. Combining this equation with Equation 3.2, the first-order vibration Raman equation is given as:

$$\mu(t) = \alpha(R_0) E_0 \cos(2\pi\nu_0 t) + \frac{d\alpha}{dR} E_0 q\{\cos[2\pi(\nu_0 + \nu_{vib})t] + \cos[2\pi(\nu_0 - \nu_{vib})t]\} \tag{3.5}$$

In the higher order terms of Equation 3.2, $(\nu_0 \pm 2\nu_{vib})$, $(\nu_0 \pm 3\nu_{vib})$, . . . can be observed are called the second-order, third-order, . . . Raman effect. The three different frequencies $\nu_0, (\nu_0 \pm \nu_{vib})$ of the dipole indicate three different kinds of scattering, including Rayleigh scattering, Stokes scattering and anti-Stokes scattering, as shown in Figure 3.8.[158] In the process of Rayleigh scattering, the excited molecule relaxes from the virtual state—the polarized state which is not a true energy

state—to the initial state, and a photon is generated with the same frequency as the incident light. Rayleigh scattering is an elastic scattering. In the process of Stokes scattering and anti-Stokes scattering, the excited molecule relaxes from the virtual state with the frequency of $(\nu_0 \pm \nu_{vib})$ to the initial state and a photon is generated with a lower or higher frequency. Both Stokes scattering and anti-Stokes scattering are inelastic and referred to as Raman scattering. In the Raman spectrum, the frequency shift to lower energy is referred to as a Stokes line, while the shift to higher energy is called an anti-Stokes line. Atoms or molecules have their specific Stokes lines and anti-Stokes lines, which are independent of the incident light. According to this characteristic, the Raman spectrum can be used as the fingerprint spectrum for material identification.

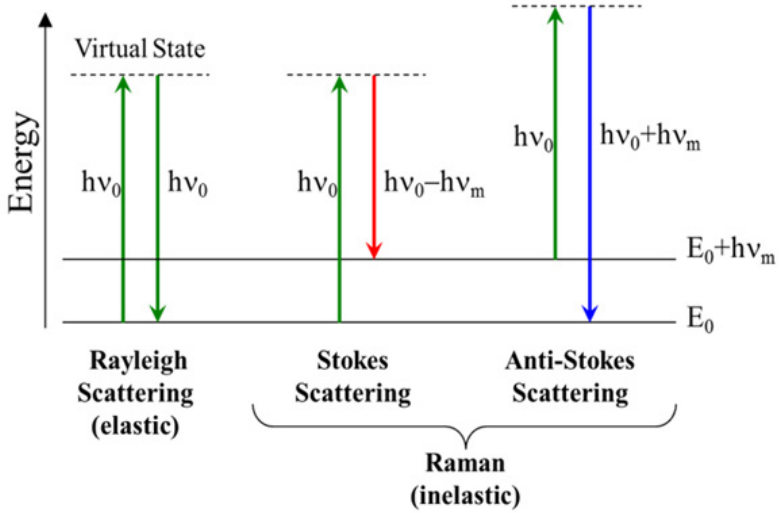

Figure 3.8 Schematic energy transition diagram for Rayleigh and Raman scattering.

3.2.2 Operation of the Raman System

Raman spectroscopy usually makes use of a laser as its excitation source with typical wavelengths of 473 nm, 532 nm, 633 nm and 780 nm. In order to obtain a stronger Raman signal, shorter laser wavelengths are employed because the intensity of Raman scattering is inversely proportionate to λ^4.[159] This might encourage the employment of a laser source with a shorter possible wavelength in the Raman system, but the probability of fluorescence occurring is increased with the shorter wavelength laser due to its higher energy excitation. Though low-level fluorescence disturbance can be reduced or eliminated by some strategies or computer algorithms, strong fluorescence saturates the photo detector and makes a Raman measurement impossible. Fluorescence excitation caused by a specific wavelength light is much less likely to occur if another wavelength light is used, so a typical Raman system is usually equipped with different wavelength lasers to eliminate fluorescence The frequency shifts of Raman scattering are quite small (in the order of $1cm^{-1}$), so a double or even triple monochromator is normally required to detect the inelastic scattering to obtain a Raman spectrum. In addition, the line width of the frequency of the incident light should be as narrow as possible—usually a laser—in order to separate the weak Raman scattering light from the high-intensity elastic scattering light. The edge of the Raman spectrum depends on the capability of the notch filters to exclude the Rayleigh scattering. A schematic drawing of Raman spectroscopy is shown in Figure 3.9.[160]

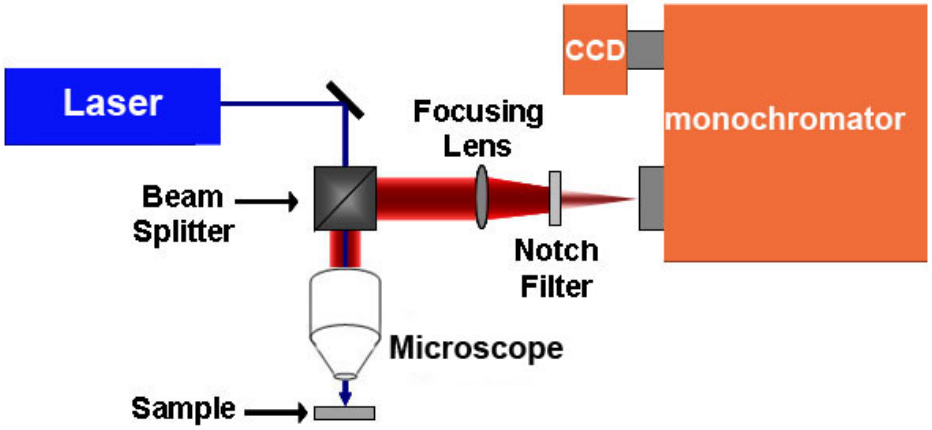

Figure 3.9 Schematic drawing of Raman spectroscopy.

3.3 Scanning Electronic Microscopy

Scanning electron microcopy (SEM) is a powerful and widely used instrument to obtain a picture of a three-dimensional object that can be directly observed by people. The SEM image is formed using a different method than a normal optical image. The main parts of a typical SEM image include an electron gun, condenser and objective lenses, a series of apertures, the specimen controller and the vacuum chamber, as shown in Figure 3.10. Free electrons are generated by the electron gun and accelerated toward an anode with energies from 1 keV to 40 keV. Condenser lenses are used to converge the electron beam into a small focused point, about 1000 times smaller than its initial size, on the sample.

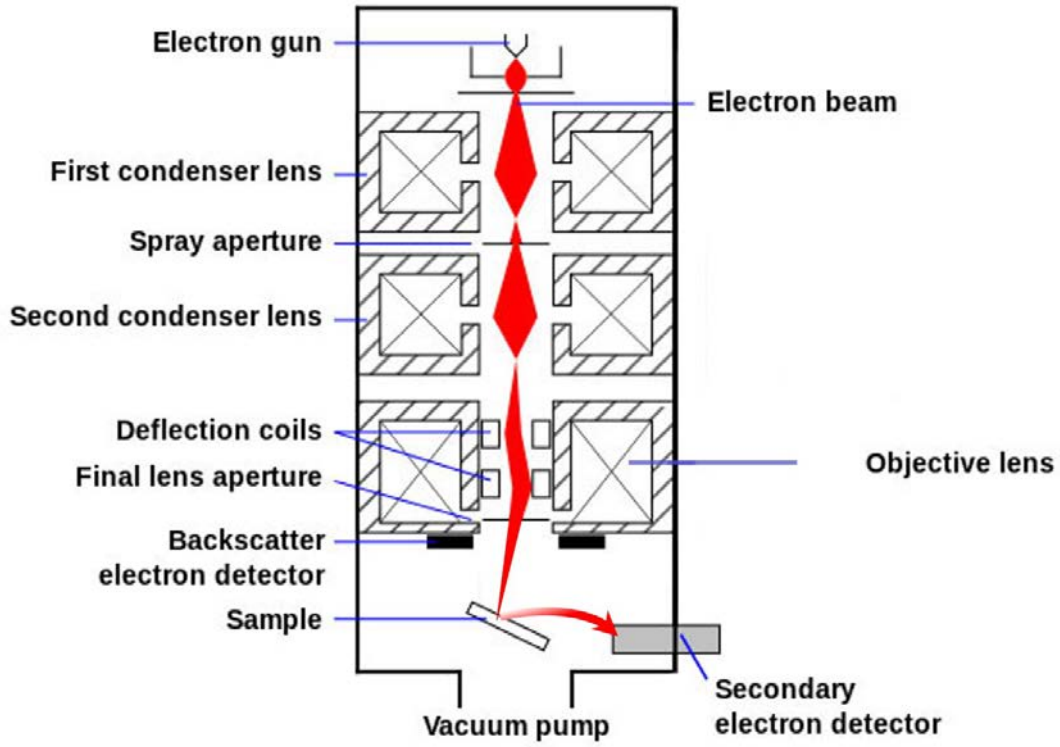

Figure 3.10 Schematic picture of scanning electronic microscopy.

The spot size can be less than 10 nm, but still has enough current to provide a clear image. One or more apertures are equipped in the SEM system to eliminate external electrons in the lenses. The final lens aperture below the deflection coil helps to adjust the spot size of the beam on the sample. The resolution and the depth of focus of a SEM image partly depend on the spot size on the sample; a higher resolution can be obtained by decreasing the spot size, but this results in a loss of brightness. The deflection coil in the objective lens controls the electron beam to scan the sample to generate images. A vacuum chamber with a pressure of at least $5*10^{-5}$ torr is required for the operation of the SEM system for various reasons. First, since the filament to generate electrons works at a high temperature above 2000℃, the hot

filament will be oxidized in the air. Secondly, particles and dust in the air will interfere or block the electron beam before it reaches the sample surface. Third, the acceleration field in the electron gun may be higher than 30 kV, which can cause the ionization of air.[161]

A variety of signals can be obtained due to the complex interactions of the electrons with the sample surface. The interaction depth is about 10 μm, as shown in Figure 3.11. Two types of signals, secondary and backscattered electrons, are utilized to acquire a SEM image of a sample surface morphology. Secondary electrons and backscattered electrons are generated by two different kinds of interactions that occur near the sample surface. Secondary electrons are generated by the inelastic collision between the incident electrons and the electrons in the sample surface at a depth of about 100 nm. They are commonly used to investigate the structure of the sample surface.

Backscattered electrons are generated by the elastic collision of the incident electrons with the electrons or nuclei at a deeper depth, at about 1 μm from the material surface. For further depth interactions between the electron beam and the sample, X-rays are generated by the recombination of free electrons and holes. The further depth X-ray signal can be used to investigate elemental composition through energy dispersive X-ray spectroscopy (EDS).[162] Figure 3.11 shows a cross section of the depth and the volume of several kinds of signals as a result of interactions between the electron beam and the sample.

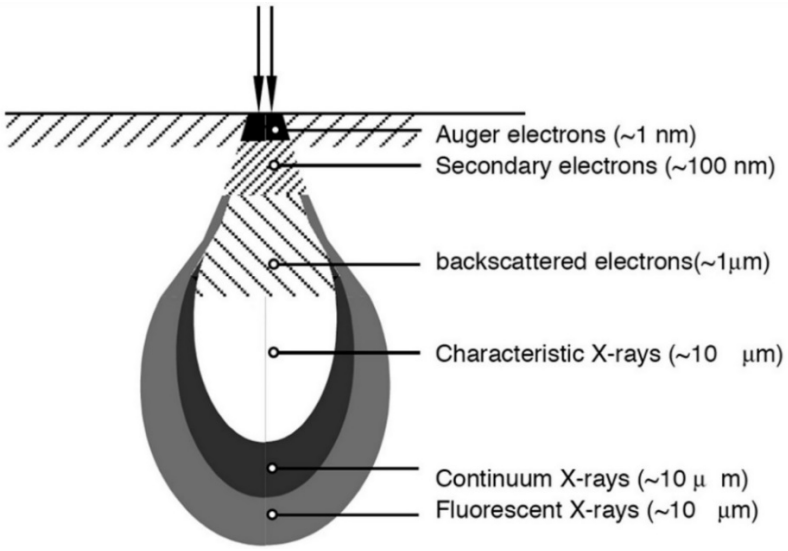

Figure 3.11 Interaction of the electron beam and the specimen.

3.4 Atomic-force Microscopy

3.4.1 Basic Principles

Atomic-force microscopy (AFM) is a technique to investigate surface morphology in three-dimensional view. AFM was invented by Binning et al. in 1986.[163] The sample surface is scanned by a sharp probe to measure changes in the interaction force between the probe tip and the sample surface. Figure 3.12 shows the schematic drawing of an atomic-force microscope. Applying a sharp tip above the sample surface, the separation distance determines the dominant interaction force—

either short-range or long-range force. A positive or negative bending of the cantilever can be detected by a laser beam targeted at the back side of the cantilever and reflected onto a photodetector. By using the probe tip to scan the sample surface and recording the deflection, the surface morphology and other properties (such as adhesion, friction, hardness and elasticity) can be detected.[164] AFM is commonly used to investigate multiple kinds of materials, including conducting or non-conducting materials, soft biological specimens and clusters of molecules or individual macromolecules in different environments, such as air, liquids and in a vacuum. In addition, sample preparation for AFM measurement is quite simple in contrast to scanning tunneling microscope (STM).

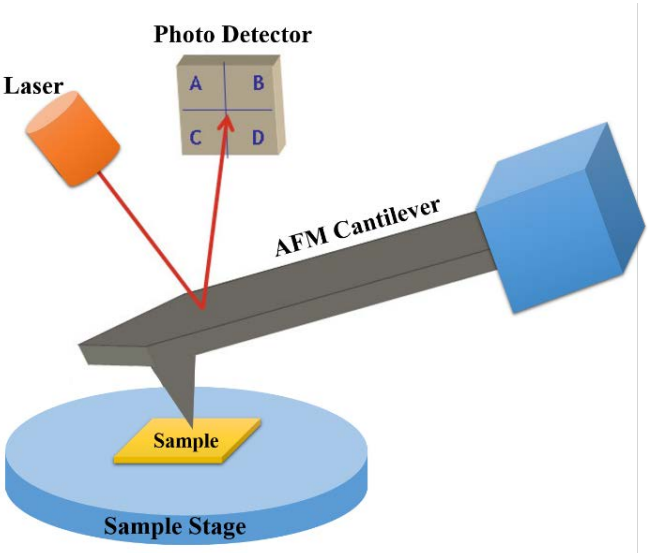

Figure 3.12 Schematic drawing of atomic-force microscopy.

AFM can only operate in the condition that the tip and sample are within an interactive force field. When the tip approaches the sample surface, different kinds of forces operate as shown in Figure 3.13.[164] In the contact region, the probe tip stays only a few angstroms above the sample surface, and the interaction force of the tip and the sample surface is dominated by short-range repulsive force. This comes from the electrostatic repulsive interaction between the electron clouds and the sample surface, and is reduced as the tip and the sample are separated. In the non-contact region, the probe tip stays up to hundreds of angstroms above the sample surface, and the interaction force of the tip and the sample surface is dominated by the long-range attractive force, also known as the van der Waals force. As the probe tip approaches the surface of the sample, attractive van der Waals force increase to induce the cantilever to deflect towards the sample. Nevertheless, at a distance of less than a few angstroms, the repulsive electrostatic force becomes dominant to induce the positive deflective of the cantilever. Along with the Coulomb force and the van der Waals force, various other interactions can also affect the tip. When conducting AFM in the air, there may be a thin layer of moisture covering the tip and sample surface. When the tip approaches the sample surface, capillary force is generated due to the liquid layer.

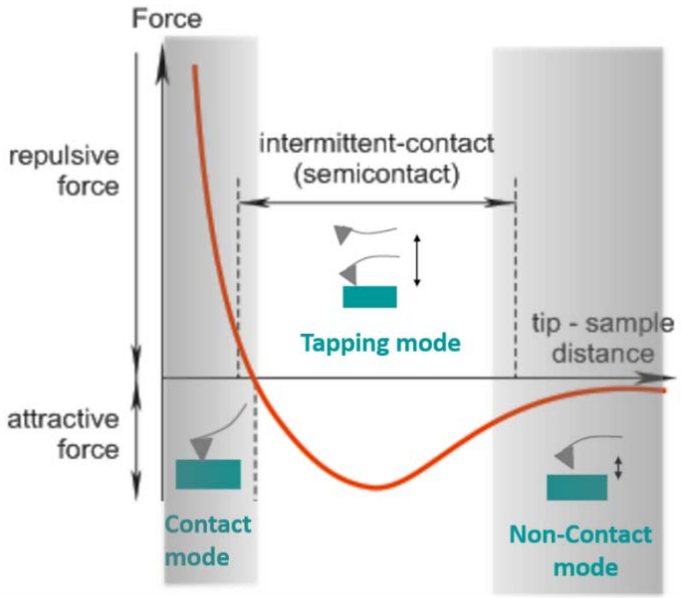

Figure 3.13 Force versus distance diagram of tip and sample and operation modes.

3.4.2 Operation Modes

The three primary types of AFM include: 1) contact mode, of which the separation of the probe and the sample is less than 0.5 nm; 2) intermittent contact mode, which is also referred to as tapping mode, of which the separation of the probe and the sample is in the range of 0.5 nm to 2 nm; and 3) non-contact mode, of which the separation of the probe and the sample is in the range of 1 nm to 10 nm.[165, 166]

Contact mode is the most commonly used mode in AFM operation. In this mode, the probe maintains gentle physical contact with the sample during the scanning process. The bending force of the cantilever can be described by Hooke's law:[167]

$$\boldsymbol{F = -k \cdot x} \tag{3.6}$$

where $\boldsymbol{k}$ is the spring constant of the cantilever and $\boldsymbol{x}$ is the deflection of the

cantilever. The tip works at a small constant distance above the sample, which is called the constant distance mode. The cantilever keeps a constant force maintaining a constant cantilever deflection by using the feedback loops, which is called the constant force mode. The contact mode of AFM can provide a high-resolution image of the sample surface, even at the nanometer scale.

Intermittent mode, also called tapping mode, is similar to contact mode. However, in this scan mode, the cantilever is driven at its resonant frequency, usually at hundreds of kHz. The tip is tapping lightly on the sample surface, maintaining a constant oscillation. As the tapping is rapid relative to its oscillation time, the lateral force is significantly reduced. Tapping mode is preferred to obtain high-resolution images of samples that are soft and easily damaged, or when the structures are loosely bonded to a surface. In non-contact mode, the cantilever oscillates above the surface of the sample and the tip and the sample are separated by the attractive force regime dominated by the van der Walls force. In non-contact mode, the tip operates at least above the adsorbed thin water layer on the sample surface during scanning. If the probe tip is too close to the surface, capillary force will bring the tip down to contact the sample surface, which is referred to as jump-to-contact. The feedback loop is applied to monitor the amplitude of the cantilever to measure the attractive force of the surface.

The choice of AFM mode depends on the properties of the sample and which of its characteristics are being investigated. Contact mode is commonly used to measure

hard surface samples and enables the manipulation of the sample surface. However, the tip may suffer contamination from the sample and excessive force in the contact mode may damage the probe tip. In non-contact mode, the probe tip remains above the sample surface, but it is sensitive to external oscillations and the absorbed liquid layer on the sample surface in the air. In tapping mode, the tip periodically contacts the surface. The primary properties of the three modes of operation are summarized in Table 3.1.[164]

Table 3.1 Properties of the three modes of operation in AFM.

Mode of operation	Interaction force	Probe state	Contamination
Contact mode	Strong repulsive force	Constant force or constant distance	Yes
Non-contact mode	Weak attractive force	Vibrating probe	No
Tapping mode	Strong repulsive force	Vibrating probe	Yes

3.5 X-ray Photoelectron Spectroscopy

3.5.1 Basic Principles

X-ray photoelectron spectroscopy (XPS) is a non-destructive technique for the investigation of the chemical composition and electronic state of the sample surface. The common detection depth of a sample surface is in the range of 5 nm to 10 nm. The basic principle of the photoelectron effect that explains the energy conversion when a photon is absorbed was initially described by Einstein in 1905.[168]

According to the photoemission theory, Swede Kai Siegbahm developed the electron spectroscopy for chemical analysis (ESCA) technique, which is also simply called XPS today.[169] In doing so, Siegbahn revealed the existence of slightly different energy levels due to the different electronic structure of an atom. When a beam of photons strikes the sample surface, an incident photon transfers its energy to a bound electron in the sample to excite the electron to a higher energy level, as shown in Figure 3.14. If the excited energy is greater than the vacuum level, the electron has enough energy to escape from the solid and can be detected by the electron spectrometer. The energy conservation in this process can be expressed as:

$$E(A) + h\nu = E(A^*) + E_{kinetic} + \Phi \tag{3.7}$$

$$E_{kinetic} = h\nu - [E(A^*) - E(A)] - \Phi = h\nu - E_B - \Phi \tag{3.8}$$

where $E_{kinetic}$ is the kinetic energy of the escaped electron, $h\nu$ is the photon energy, E_B refers to the binding energy of the electron and Φ is the work function. By analyzing the energy state of the collected electrons and the energy of incident photons, the initial energy of the excited electron can be obtained based on the energy conservation equation. The XPS spectra plotted by the kinetic energy distribution provide information regarding the sample's chemical elements. The intensity of peaks is proportional to the atoms number of elements, by which the stoichiometry is obtained. The valence band maximum (VBM) with respect to the Fermi level is determined by the intersection between the linear fits to the leading edge of the valence band and the baseline.

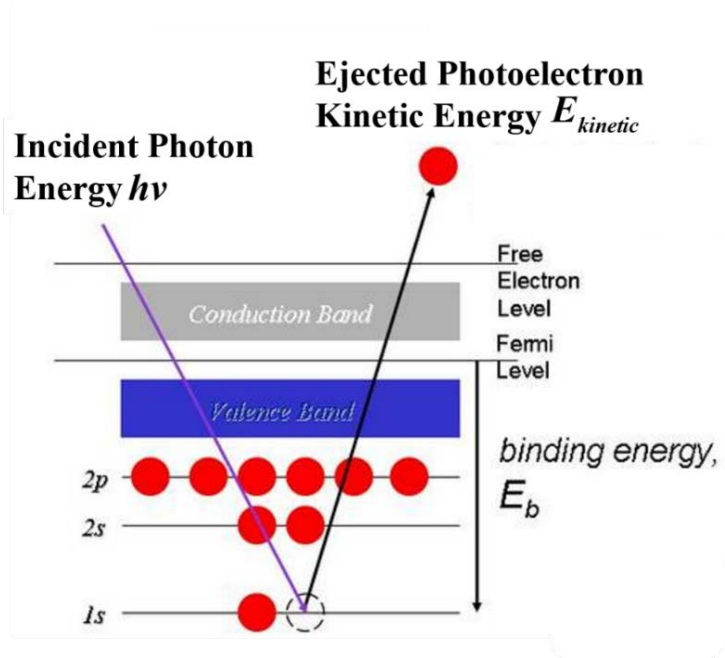

Figure 3.14 Schematic illustration of the photoemission process.

3.5.2 Experimental Setup

The XPS components include a UHV chamber, a hemispherical electron energy analyzer, X-ray source and the electronic control system, as shown in Figure 3.15. The X-ray source includes a filament to emit thermal electrons to bombard the anode material, usually Al or Mg, to generate X-ray photons. The energy of emitted photons for Al and Mg is 1486.6 eV and 1253.6 eV, respectively.[170, 171] The line width of the energy distribution of the incident X-ray beam is an important parameter determined by the resolution of the XPS spectrum. The line width can be reduced by a quartz crystal monochromator. The typical line width values of the Al and Mg anodes are about 0.85eV and 0.7eV.

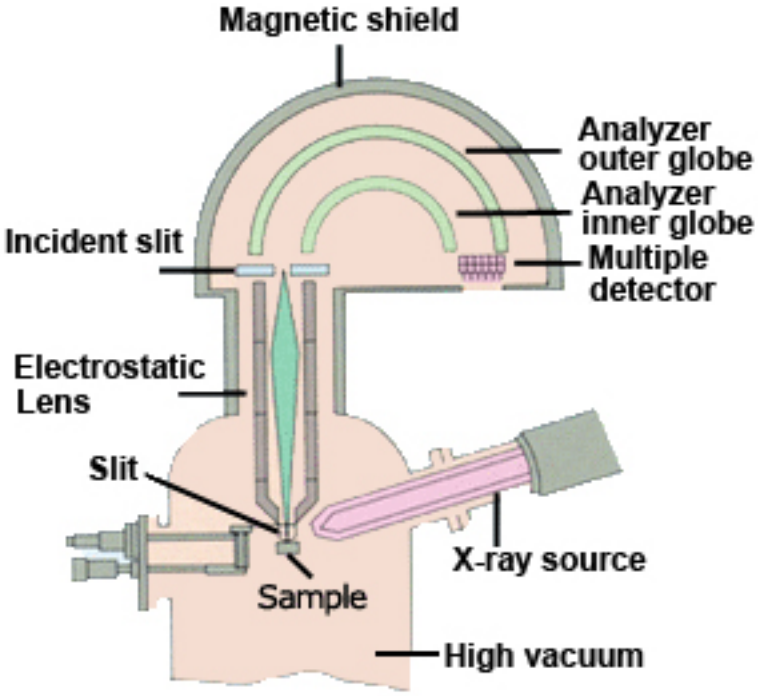

Figure 3.15 Schematic drawing of the XPS setup.

A hemispherical electron energy analyzer is used to detect ejected electrons from the sample surface. It commonly includes a group of electrostatic lenses, two concentrically positioned hemispheres analyzers and a detector. The electrostatic lenses are employed to slow down the speed of the ejected electrons, and the deflection voltage between the two hemispheres only permits electrons traveling at a certain speed to pass through the hemisphere analyzer to the detector. The typical detector used to detect the electrons that pass through the analyzer is an electron multiplier to amplify the signal to about 10^8, permitting even a single electron to be counted. Hence, the analyzer selects the electrons with specific energy and the detector counts their number.

3.5.3 Reference Level

In the simple case of the gas phase, based on the free atom models, the binding energy of the molecules are referenced at the vacuum level. However, for the solid phase, the reference of the binding energy is more complicated. A convenient method is to select the Fermi level as the reference level. The energy level diagram for solids is shown in Figure 3.16. Equation 3.8 can be written as:

$$h\nu = E_{kinetic} + E_B^F + \Phi_S = E_{kinetic} + E_B^V \tag{3.9}$$

where $\boldsymbol{E_B^F}$ and $\boldsymbol{E_B^V}$ are the binding energy referred to as the Fermi level and the vacuum level. If the sample is in electrical contact with the detector, in the condition of equilibrium, the Fermi level should be at the same energy level. The kinetic energy of the photoelectron will be perturbed by the contact potential between the sample and the spectrometer, and is given by:

$$E_{kenitic}^{'} = E_{kinetic} - (\Phi_{SP} - \Phi_S) \tag{3.10}$$

Combining Equations 3.9 and 3.10, binding energy $\boldsymbol{E_B^V}$ and $\boldsymbol{E_B^F}$ can be expressed as:

$$\boldsymbol{E_B^F = h\nu - E_{kinetic}^{'} - \Phi_{SP}} \tag{3.11}$$

$$\boldsymbol{E_B^V = h\nu - E_{kinetic}^{'} - (\Phi_{SP} - \Phi_S)} \tag{3.12}$$

The measured binding energy $\boldsymbol{E_B^F}$ depends on the work function $\boldsymbol{\Phi_{SP}}$, which is a fixed value of a certain detector. However, $\boldsymbol{E_B^V}$ depends on both $\boldsymbol{\Phi_{SP}}$ and $\boldsymbol{\Phi_S}$, and $\boldsymbol{\Phi_S}$ usually varies up to several eV due to the existence of impurities. Hence, $\boldsymbol{E_B^F}$ is

usually adopted as the reference.

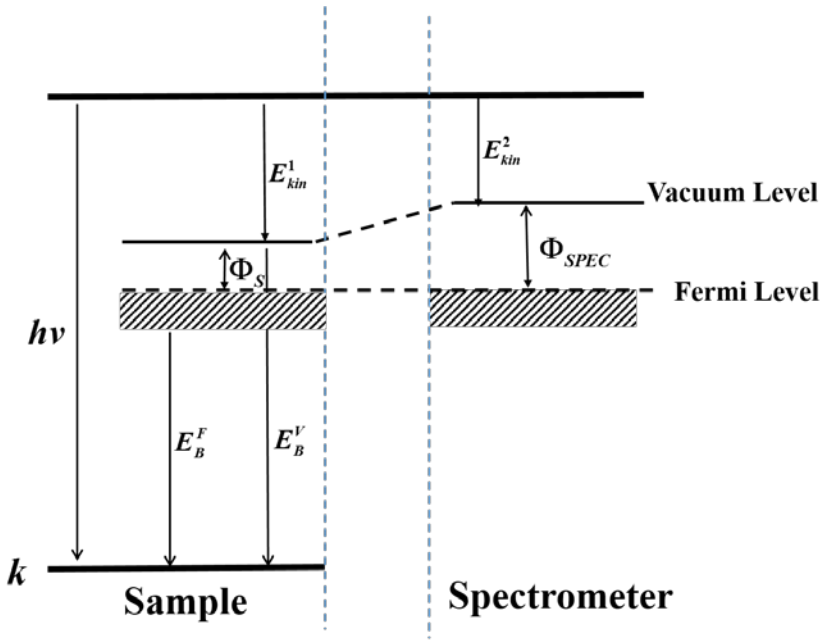

Figure 3.16 Schematic diagram of reference levels.

3.5.4 Quantitative XPS Analysis

XPS elemental spectra provide the qualitative information for the elemental composition a few nanometers from the surface, since the number of detected photoelectrons for a certain kinetic energy is proportional to the number of atoms of corresponding binding energy. Relative concentrations can be calculated from the areas under the corresponding peaks in the XPS spectra, which are proportional to the measured photoelectron current.[169] Assuming that the sample composition is uniform and the X-ray flux is set at a fixed value, the photoelectron current can be

expressed by the equation:

$$I_A(X) = K\sigma LN_A\lambda_m \sin(\theta)GD \tag{3.13}$$

where K is the X-ray flux, σ is the cross section of the photoionization, L is the angular asymmetry factor of the photo emission from a certain core level, N_A is the distribution of atoms, λ_m is the inelastic mean free path (nm), G is the spectrometer etendue, D is the detector efficiency and θ is the emission angle. According to Equation 3.13, the intensities of elements depend on the properties of a certain material. The relative sensitivity factor is the normalization factor referred to as the fluorine F1s peak. The sensitivity factor can be extracted from Equation 3.14.

$$\frac{I_A}{I_F} = \frac{K\sigma LN_A\lambda_A \sin(\theta)GD}{K\sigma LN_F\lambda_F \sin(\theta)GD} = S_A \frac{N_A}{N_F} \tag{3.14}$$

where $G\ D\ K$ are reductions for the same instrument, and other terms can be put together as the sensitivity factor relative to F atom. If the intensity of F atom is regarded as one, the intensity of atom A is S_A times the ratio of the atom number of A to F.

Another more common method used to determine the sensitivity factor is to measure the sensitivity factors of a specific system in a lab, which is a more accurate method of considering slight modifications for a specific system. Nevertheless, the determination of sensitivity factors in the lab requires high-purity standard materials, and these sensitivity factors are usually provided by manufacturers. The relative number of the specific atoms can be calculated by dividing the peak intensity by the relative sensitivity factor, and the concentration of the specific element is obtained by

dividing the number of the specific atoms by the total number of atoms. The atoms' number of elements is proportional to the intensity of the photoelectron current measured by XPS, thus the concentration can be written as:

$$C_A = \frac{I_A / S_A}{\sum_n \left(I_n / S_n \right)} \tag{3.15}$$

where C_A is the concentration of element A, I_A and I_n are the signal intensity of element A and n, and S_A and S_n are the sensitivity factors of element A and n.

3.5.5 Valence Band Offset Measurement

The valence band maximum (VBM) can be measured by XPS in the energy range from -5 eV to 30 eV. All of the valence electrons from the surface of the sample are detected in this region. The VBM, with respect to the Fermi level, is determined by the intersection between the linear fits to the leading valence band edge and the baseline, as shown in Figure 3.17.[172-174] The energy of photoelectrons cannot be higher than the energy level of the valence band maximum due to the fact that electrons only fill in the valence bands, instead of conduction bands for semiconductors. Because of the lattice interruption, the energy level of the crystal interface has a deviation from the bulk materials. The Fermi level must align to be equal for different materials in contact, thus band bending exists at the interface of different materials for electron conduction.

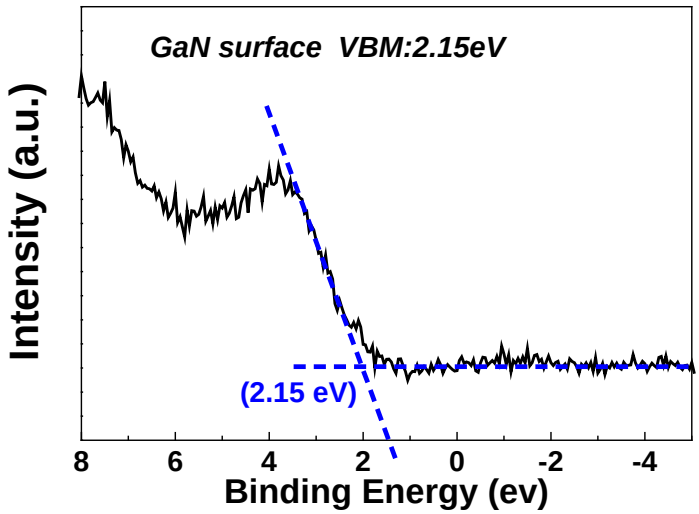

Figure 3.17 XPS spectra of the valence band of GaN.

To measure the VBM offset at the interface by XPS, an ultra-thin layer of material needs to be deposited on the substrate to measure the relative shift at the interface of two materials. The valence band offset ΔE_v can be written as:

$$\Delta E_v = \left(E_N - E_v^A\right) - \left(E_M - E_v^B\right) - \left(E_N^i - E_M^i\right) \tag{3.16}$$

where E_N and E_M are the binding energy of the core level of materials A and B, E_v^A and E_v^B are binding the energy of the valence band of materials A and B, E_N^i and E_v^B are the binding energy of the core level of materials A and B at the interface. The conduction band offset can be obtained by adding the band gap difference to the valence band offset.[175, 176]

3.6 Low Frequency Noise Measurements

3.6.1 Spectral Analysis

Noise in semiconductor devices is a random, spontaneous fluctuation of measured signals. Disturbances in electronic systems generated from exterior sources, such as influences from adjacent circuits, light and vibrations, as well as radio transmitters, are not discussed in this work, as the external disturbances can be eliminated by shielding, filtering or the specific design of an electronic system. Noise from internal disturbances, such as electron scattering and electron-hole pair generation or recombination, can be reduced by the proper design of a device, but it is impossible to be completely eliminated. The electronic signal fluctuation due to noise can be written as a function of time $x(t)$, where t is the time. An important statistical function for the noise study is the power spectral density, which is written as:[177, 178]

$$S_X(f) = \lim_{T\to\infty} \frac{2|X_T(f)|^2}{T} \tag{3.17}$$

where $X_T(t)$ is the Fourier transform of $x_T(t)$,

$$x_T(t) = \begin{cases} x(t), & |t| \le T/2 \\ 0, & |t| \ge T/2 \end{cases} \tag{3.18}$$

The unit of the spectral density is $[x]^2/\mathrm{Hz}$. For the theoretical study of noise, the autocorrelation function is commonly used to indicate the stochastic process and is defined as:

$$\Phi_x(t) \equiv < x(\tau)\, x(\tau + t) >= \lim_{T\to\infty} \frac{1}{T} \int_{-T/2}^{T/2} \mathrm{d}\tau\; x(\tau)\, x(\tau + t) \tag{3.19}$$

where the angle brackets denote the ensemble average. Considering the assumption of the ergodic random variable, the ensemble average is equivalent to a time average. The autocorrelation is independent of time t, but associated with the time difference τ. Based on the Winener-Khinthcine theorem, the power spectral density is connected to the autocorrelation through the Fourier transform,

$$S_X(f) = 2\int_{-\infty}^{\infty} \mathrm{d}\tau\; \Phi_x(\tau) \exp(-j2\pi f\tau) = 4\int_0^{\infty} \mathrm{d}\tau\; \Phi_x(\tau) \cos(2\pi f\tau) \tag{3.20}$$

$$\Phi_x(\tau) = \int_0^{\infty} \mathrm{d}f\; S_x(f) \cos(2\pi f\tau) \tag{3.21}$$

A factor of two locates before Fourier integrals by assuming the frequency is in the positive range.

3.6.2 Noise Classification

According to the physical origins and the spectral density, noise in semiconductors can be classified as the following types:[179]

(1) Thermal noise, also known as Johnson noise, originates from the thermal agitation of carriers. At the condition of thermal equilibrium, the thermal noise for a resistor is given by Nyquist's formula, $S_v = 4k_B TR$, where k_B is the Boltzmann constant, T is the device temperature and R is the resistance.

(2) Shot noise results from the random transit of carriers in an electronic device. This kind of fluctuation is commonly statistically negligible except in the case of a rare number of transit carriers. Both shot noise and thermal noise are

independent of frequency and are called white noise.

(3) Generation-recombination (G-R) noise arises from the capture and emission of carriers by traps in a semiconductor, resulting in a local carrier density fluctuation. The power spectrum of G-R noise can be expressed in a Lorentzian form, as follows:

$$S_i = \frac{B\tau}{1+(2\pi f\tau)^2} \tag{3.22}$$

where τ is a time constant and B is a function of current in a device.

(4) $1/f$ noise, also known as the flicker noise, is normally characterized by a power-law spectrum, $S \propto 1/f^{\gamma}$, where γ remains constant. The origin of $1/f$ noise is still debated.

Thermal noise and shot noise, which dominate at high frequencies, are white noise. However, G-R noise and $1/f$ noise are commonly found at low frequency ranges and will be discussed in the following sections.

3.6.3 Generation-Recombination Noise Theories

The capture and release of carriers by traps and the random transitions of charge carriers between different energy states in a semiconductor results in fluctuations of carrier concentration, which may vary several orders of magnitude. Thus, G-R noise is inherently owing to the fluctuations in carrier numbers, generally maintaining the charge neutrality of the device.[180-182] Traps exist in various forms, consisting of

shallow and deep levels of donors and acceptors, impurities and crystal defects, etc. The trap sites introduce energy levels in the energy band diagram of semiconductors. The transition of the carriers between the trap energy level and the conduction band and valance band includes the following processes: a) the capture of electrons in the conduction band by traps; b) the emission of electrons from the trap to the conduction band; c) the capture of holes from the valence band by traps; and d) the emission of holes from the trap to the valence band.[183, 184] A schematic illustration of these transition processes is shown in Figure 3.18.

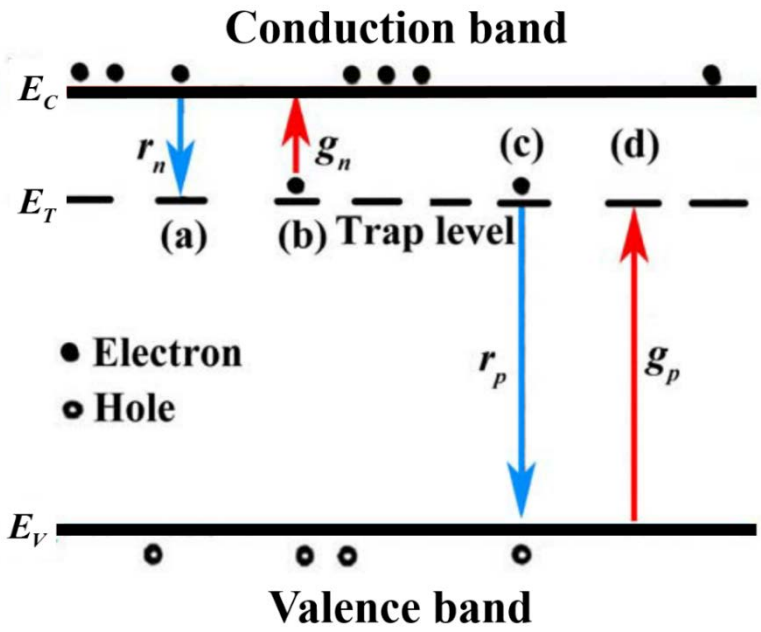

Figure 3.18 Schematic illustration of the transition processes in the semiconductor.

The electron transition rate between the trap level ($\boldsymbol{E_T}$) and the conduction band ($\boldsymbol{E_C}$) is given by: [185]

$$g_n = e_n n_T \tag{3.23}$$

$$r_n = c_n n(N_T - n_T) \tag{3.24}$$

where c_n is the electron capture coefficient with the unit of $cm^{-3}s^{-1}$, e_n is the electron emission coefficient with the unit of s^{-1}, n is the density of electrons, N_T indicates the trap density, and n_T indicates the density of the filled traps with the unit of cm^{-3}. In a similar way, the hole transition rate between the trap level (E_T) and the valence band (E_V) can be written as:

$$r_p = c_p p n_T \tag{3.25}$$

$$g_p = e_p(N_T - n_T) \tag{3.26}$$

where c_p is the hole capture coefficient with the unit of s^{-1}, e_p is the electron emission coefficient with the unit of $cm^{-3}s^{-1}$, and p is the density of the holes.

All the capture and emission processes influence the fluctuations of n_T ; thus, the net change rate of n_T can be written as:

$$\frac{dn_T}{dt} = r_n - g_n - r_n + g_p \tag{3.27}$$

Under the equilibrium condition, the net rate change of n_T is equal to zero,

$$r_n - g_n - r_p + g_p = 0 \tag{3.28}$$

Considering there is a steady state, the accumulation of holes and electrons in the valence band and conduction band should be equal to zero, thus:

$$r_p - g_p = c_p p_o n_{T_o} - e_p (N_T - n_{T_o}) = 0 \tag{3.29}$$

$$r_n - g_n = c_n n_o (N_T - n_{T_o}) - e_n n_{T_o} = 0 \tag{3.30}$$

where the subscript o indicates the equilibrium condition. Then the emission coefficients can be written with the capture coefficients as:

$$e_n = c_n n_o \frac{N_T - n_{T_o}}{n_{T_o}} = c_n n_o \frac{1 - f_T}{f_T} \tag{3.31}$$

$$e_p = c_p p_o \frac{n_{T_o}}{N_T - n_{T_o}} = c_p p_o \frac{f_T}{1 - f_T} \tag{3.32}$$

where $f_T = n_{T_o} / N_T$ is the fraction of the filled traps and can be expressed in the form of the Fermi-Dirac distribution function:

$$f_T = \frac{1}{1 + g \exp\left(\frac{E_T - E_F}{k_B T} \right)} \tag{3.33}$$

where E_T is the energy level of traps, E_F is the Fermi level and g is the trap degeneracy factor. Substituting Equation 3.33 into Equation 3.31 and 3.32, the emission coefficients can be written as:

$$e_n = g c_n n_o \exp\left(\frac{E_T - E_F}{k_B T} \right) \equiv c_n n_s \tag{3.34}$$

$$e_p = \frac{1}{g} c_p p_o \exp\left(\frac{E_F - E_T}{k_B T} \right) \equiv c_p p_s \tag{3.35}$$

where n_s and p_s are defined as:

$$n_s \equiv g n_o \exp\left(\frac{E_T - E_F}{k_B T} \right) \tag{3.36}$$

$$p_s \equiv \frac{1}{g} p_o \exp\left(\frac{E_F - E_T}{k_B T} \right) \tag{3.37}$$

Therefore, the change rate of n_T can be written as:

$$\frac{dn_T}{dt} = c_n\left(nN_T - nn_T - n_s n_T\right) - c_p\left(pn_T - \frac{1}{g}p_s N_T + p_s n_T\right) \tag{3.38}$$

For n-type extrinsic semiconductors, the electron concentration is considerably greater than the hole concentration. Therefore, the transitions of holes between trap level and the valance band can be neglected. Thus, Equation 3.38 can be written as:

$$\frac{dn_T}{dt} = c_n\left(nN_T - nn_T - n_s n_T\right) \tag{3.39}$$

By considering the fluctuation of n_T with the equilibrium value n_{T_0}, n_T can be written as:

$$n_T = n_{T_0} + \Delta n_T \tag{3.40}$$

$$n = n_0 - \Delta n_T \tag{3.41}$$

Since there is little deviation of n_T from the equilibrium value n_{T_0}, the relaxation rate from n_T to n_{T_0} is given as:

$$\frac{dn_T}{dt} = \frac{d\Delta n_T}{dt} = -c_n\left[\left(N_T - n_{T_0}\right) + n_0 + n_s\right]\Delta n_T \equiv -\frac{\Delta n_T}{\tau_T} \tag{3.42}$$

where τ_T is the time of the relaxation process, which is given as:

$$\tau_T = \frac{1}{cn\left[\left(N_T - n_{T_0}\right) + n_0 + n_s\right]} \tag{3.43}$$

Based on the above equations, the kinetics of the electron trapping in an n-type semiconductor can be entirely described by four parameters: c_n, N_T, g, and n_s.

3.6.4 Generation-Recombination Noise Statistics

Random transitions of electrons and holes among the trap levels, the conduction band and the valance band are considered in the G-R noise, leading to a considerably complex calculation of the noise statistics. However, an approximation that each trap level interacts independently with either the conduction band or the valence band is made to simplify the calculation of noise properties. There are two criteria that need to be satisfied to make this approximation valid: 1) the difference between the Fermi level and the trap level is no less than the number of $k_B T$; and 2) the carrier concentration is significantly higher than the trap concentration.[186]

For the electron transition between a single trap level and the conduction band, the random electron trapping can be considered as free electrons $N(t)$, and the current $I(t)$ is written as:

$$I(t) = \xi\left[N(t)\right] = \xi\left[N_0 + \Delta N(t)\right] \tag{3.44}$$

The power spectra of $\Delta I(t)$ and $\Delta N(t)$ satisfy the proportional relationship:

$$S_I(f) = S_{\Delta I}(f) = 4\int_0^\infty dt\Phi_{\Delta I}(t)\cos(2\pi ft) = (\Delta I_0)^2 S_{\Delta N}(f) \tag{3.45}$$

The autocorrelation function of the random variable of free electrons $N(t)$ is:

$$\Phi_{\Delta I}(\tau) = \left\langle \Delta N^2 \right\rangle \exp(\frac{\tau}{\tau_T}) \tag{3.46}$$

where τ_T is the relaxation time. Based on Wiener-Khintchine theory, the power spectral density of $N(t)$ is achieved through the Fourier transformation of $\Phi_{\Delta I}(\tau)$ as follows:

$$S_{\Delta N}(f) = 4\left\langle \Delta N^2 \right\rangle \frac{\tau_T}{1+4\pi^2 f^2 {\tau_T}^2} \tag{3.47}$$

By combining Equation 3.47 and Equation 3.45, the power spectrum of the current fluctuations is given as:

$$\begin{aligned} S_I(f) &= 4(\Delta {I_0}^2)\left\langle \Delta N^2 \right\rangle \frac{\tau_T}{1+4\pi^2 f^2 {\tau_T}^2} \\ &= 4(\Delta {I_0}^2)\Omega \frac{n_0\left(N_T - n_{T_0}\right)}{\left(N_T - n_{T_0}\right)+n_0+n_s} \cdot \frac{\tau_T}{1+4\pi^2 f^2 {\tau_T}^2} \end{aligned} \tag{3.48}$$

where Ω is the unit of active volume in cm^3.

Thus, the power spectral density of the current is in a Lorentzian form with the corner frequency of $f_c = 1/2\pi\tau_T$. Additionally, the kinetics of trapping is crucial for the spectral shape of $S_I(f)$.[184, 187]

3.6.5 1/*f* Noise Theories

Flicker $(1/f)$ noise exists in many different systems, including metal, semiconductor, biological, etc. In solid-state materials, a variety of theories have been developed to interpret the $1/f$ noise.

According to the research on low frequency noise in gold and semiconductor films, Hooger et al. proposed the $1/f$ noise formula:[188-191]

$$\frac{S_I(f)}{I^2} = \frac{\alpha_H}{N_c f} \tag{3.49}$$

where $S_I(f)$ is the spectral density of the noise of the current, I is the current

passing through the material, N_c is the density of the free carriers and α_H is the Hooge parameter of 2×10^{-3}. N_c, depending on $S_I(f)$, reveals that the $1/f$ noise is induced by bulk effect.[192] In general, the spectral density has no linear relationship with $1/f$, but is proportional to $1/f^{\alpha}$ ($0.8<\alpha<1.4$). Thus, Equation 3.49 is not a universal form in describing the current noise.

Handel [192-194] proposed a quantum $1/f$ noise model which suggested that the $1/f$ noise was caused by the interactions between scattered carriers and the electromagnetic field. Without considering inter-valley scattering, the Hooge parameter is in the range of 10^{-8} to 10^{-9}, whereas by including inter-valley scattering, the Hooge parameter is in the range of 10^{-5} and10^{-8}. The validity of the quantum $1/f$ noise model is still being disputed based on the reason that there is not enough evidence to support it. Similar to Hooge's model, Handel's model requires a strict $1/f$ dependence. Even so, the spectral density of the noise of many semiconductor materials is proportional to $1/f^{\alpha}$ in the low frequency range, where α is not equal to 1. But in some cases, the quantum $1/f$ noise may be overwhelmed by other noise sources.

For metal-oxide-semiconductor (MOS) systems, McWhorter [184] proposed that the $1/f$ noise comes from the fluctuations of carriers trapping in the localized states in the oxide. The main processes of the trapping and de-trapping of carriers are regarded as tunneling in this model. The power spectral density of the fluctuations of the occupied number of traps in a unit volume $\Omega = \Delta x \Delta y \Delta z$ is given as:[195]

$$S_{\Delta N}(f) = 4N_T(E,z) f_T(1-f_T)\Delta x \Delta y \Delta z E \frac{\tau_T}{1+4\pi^2 f^2 \tau_T^2} \tag{3.50}$$

where $N_T(E,z)$ is the trap density in the unit of cm^{-3}/eV and

$$\tau_T = \frac{1}{c_n\left[\left(N_T - n_{T_0}\right) + n_0 + n_s\right]} \exp(\kappa z) \equiv \tau_0 \exp(\kappa z) \tag{3.51}$$

where κz refers to the tunneling probability, κ is the WKB parameter and z is the distance from the trap to the surface of the semiconductor. The Fermi factor $f_T(1-f_T)$ mainly focuses on $E_T = E_F$. Thus, only the transitions that involve the trap levels within a few $k_B T$ towards the Fermi level make contributions to the $1/f$ noise.

Based on the trapping kinetics of the G-R noise, the power spectral density of the single trap level system can be written in a Lorentzian form. For the multiple trap level system, an approximation is made to get the total noise power spectral density, by assuming that trap levels independently interact with the valance band or conduction band. Therefore, the total power spectral density can be expressed in a Lorentzian form:[185]

$$S(f) = 4\int_x \int_y \int_z \int_E N_T(x,y,z,E) \times \frac{\tau_e \tau_c}{(\tau_e + \tau_c)^2} \cdot \frac{\tau}{1+\omega^2\tau^2} dx dy dz dE \tag{3.52}$$

where τ_e and τ_c are the capture and emission time constants. The total time constant τ is given as:

$$\tau = \frac{\tau_e \tau_c}{\tau_e + \tau_c} = \tau_0 \exp\left(\frac{E}{k_B T}\right) \tag{3.53}$$

where τ_0 indicates the inverse phonon frequency, E is the activation energy and

k_B is the Boltzmann constant. Assuming the distribution of E is uniform within the overall frequency, the power spectral density $S(f)$ can be expressed as:

$$S_I(f) = \int dE_\tau D(E_\tau) \frac{A\tau_T(E_\tau)}{1+4\pi^2 f^2 \tau_T^2(E_\tau)} \cong \frac{AD_0}{4f} \qquad for \ \ 1/2\pi\tau_1 >> f >> 1/2\pi\tau_2 \tag{3.54}$$

where τ_2 and τ_1 are the lower and upper limits of frequency and A is a constant. Actual $1/f$ dependence can be obtained from Equation 3.54 in the limited range of frequency.

3.6.6 Experimental Details

The experimental setup of a noise measuring system is shown in Figure 3.19. The device under test (DUT) was mounted in a metal shield box. The current fluctuations were amplified by a Stanford Research SR570 amplifier. All experiments were done in a shield room to eliminate external interference. The noise power spectral density was recorded by a HP3561A dynamic signal analyzer.

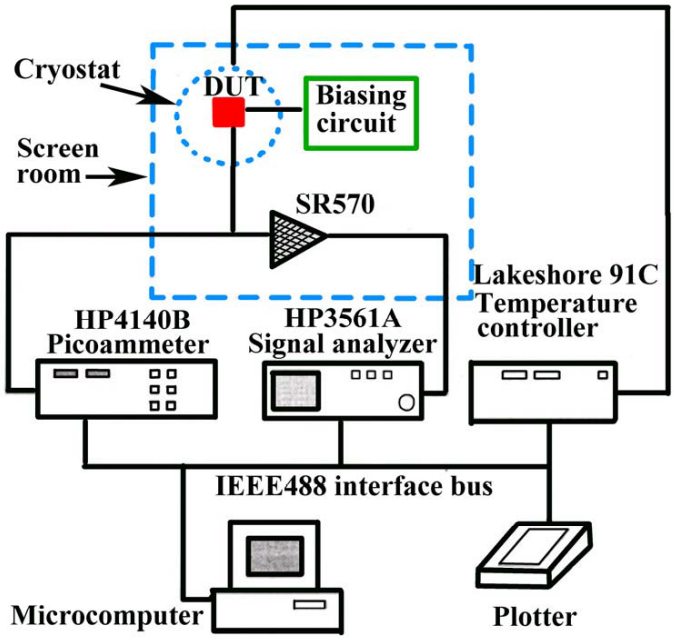

Figure 3.19 Schematic drawing of a low frequency noise measuring system.

CHAPTER 4 MOLECULAR BEAM EPITAXY OF WS_2

The crystal structure of WS_2 has the form of S-W-S with a hexagonal plane of W atoms between two planes of S atoms. The structure of the hexagonal plane is constructed by a trigonal prism of six S atoms with one W atom located in the center as shown in Figure 4.1.[41-43] The tri-layer sandwich construction with weak interlayer forces facilitates its exfoliation by chemical or mechanical methods to obtain micron-sized single layer or few layers materials. The exfoliation technique is proper for the basic investigation and the fabrication of proof-of-concept devices. Nevertheless, this technique is not suitable for large-scale commercial manufacturing. As one of the most extensively used techniques to grow high quality thin films, molecular beam epitaxy (MBE) can be used to grow large-area uniform WS_2 thin films.

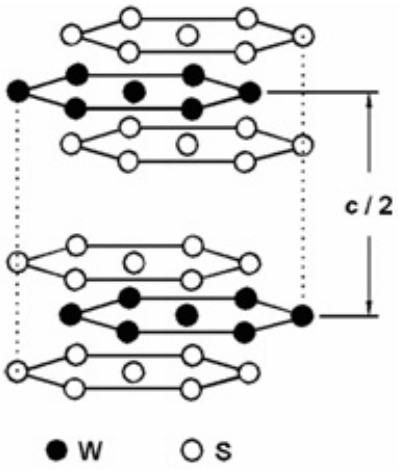

Figure 4.1 Crystal structure of hexagonal WS_2.

4.1 Experimental Details

4.1.1 Preparation of Source Materials and Growth Substrates

To ensure high-purity WS_2 thin films can be produced, high purity source materials have been used, including 99.95% tungsten pellets (Kurt J. Lesker Company) and 99.998% sulfur pieces (Sigma-Aldrich Company). In this study, mica sheets were chosen as the substrates for WS_2 growth, and they have the layered structure with relative weak van der Waals force between each layer. This kind of weak interaction benefits the van der Waals epitaxy growth and enables it to endure significant lattice mismatch,[196, 197] which makes mica an alternative to traditional 3D substrates for WS_2 growth. The chemical inertness, transparency for visible light, and electrical insulation properties of mica also make it convenient to measure the electrical and optical properties of the epitaxy growth material. Because of the weak van der Waals force between each layer, mica can be uniformly cleaved to provide a large, clean, atomically flat surface, as demonstrated in the atomic force microscope (AFM) image presented in Figure 4.2. However, the freshly cleaved mica is usually covered with inhomogeneous distribution potassium ions due to the damage to the potassium layer in the air.

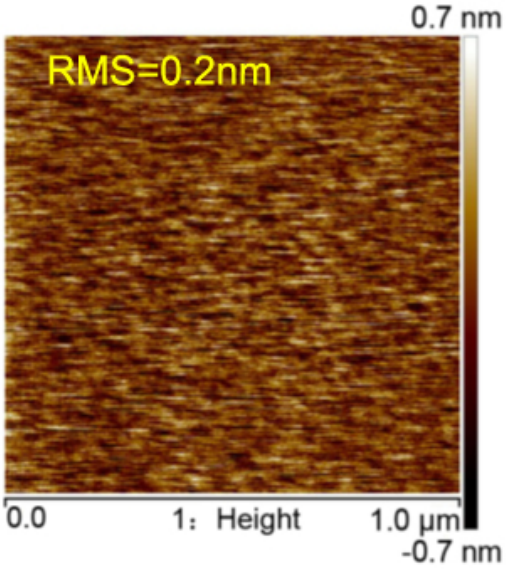

Figure 4.2 AFM image of a freshly cleaved mica surface.

Several methods have been employed to remove the residual potassium ion on the mica surface, such as evaporation of the potassium at a high temperature and laser irradiation. However, high temperatures and laser irradiation may damage the mica surface. Another gentler method is to allow the potassium to react with the CO_2 and the moisture in the air to form potassium carbonate that can be dissolved in water and rinsed away. The steps to prepare the mica substrates are as follows:

(1) Use a sharp blade or needle to penetrate the cross edge of the mica sheet, then quickly separate the mica into two sheets using tweezers.

(2) Expose the freshly cleaved mica to the air for more than 24 hours.

(3) Rinse the mica sheets with DI water several times and dry them using high purity nitrogen gas.

(4) After cleansing, immediately load the mica substrate into the growth chamber.

4.1.2 MBE Deposition of WS_2

As introduced in Chapter 2, MBE is used to grow high quality thin films beneficial to the ultra-high vacuum condition. In this work, a modified SVTA MBE system N35 was used to deposit WS_2 thin films. The MBE system consisted of a growth chamber and a load lock chamber isolated by an ultra-high vacuum gate valve. A CTI Cryo-Torr 8 cryopump and Varian titanium sublimation pump were attached to the growth chamber to achieve an ultra-high vacuum condition. The load lock chamber is equipped with an Agilent V550 turbo molecular pump backed by an oil-free Varian TriScroll 300 scroll pump. A Grandville Philips 350 ionization gauge controller was used to monitor the vacuum level of both chambers. The cryogenic shrouds attached to the growth chamber were filled by liquid nitrogen to achieve a base pressure of 8×10^{9} torr and avoid the cross contamination among the K-cells installed in the chamber.

An EBVV63 vertical UHV e-beam evaporator (Dr. Eberl Mbe-komponenten Gmbh Company) was used to evaporate the tungsten metal. During the evaporation process, the e-beam acceleration voltage was maintained at 6 kV and the emission current of the e-beam was altered to adjust the effusion flux. The sulfur source was evaporated by a VCS-63 valved cracker cell (Dr. Eberl Mbe-komponenten Gmbh Company), which was designed for sublimation or evaporation of elemental sulfur in MBE applications. The sulfur valved cracker cell provided precise sulfur flux control by the integrated all metal valve controlled by a servomotor. The independent

cracking module allowed the variation of the composition of the resulting sulfur vapor depending on the cracking temperature as shown in Figure 4.3. Generally, the high temperature cracked sulfur molecules of S_2, S_4 and S_6 were more reactive than the uncracked molecules of S_8 for chemical reaction. The cracker cell can provide more effective controllability and stability of the sulfur flux beam to control the composition of the film. Keeping the reservoir and cracker temperature at 130°C and 650°C, respectively, the S beam equivalent pressure (BEP) versus the micrometer valve position was measured by an ion gauge and plotted in Figure 4.4. The S-BEP was maintained at about 3×10^{-6} torr during the entire growth process. During deposition, the base pressure was below 8×10^{9} torr, then the substrate temperature was raised to the target value at a rate of 15°C per minute. Then, the substrate temperature was maintained for 15 minutes to thermally clean the substrate surface and achieve an equilibrium temperature before the W and S cell shutters were opened. The growth rate was about 1 nm/s, which was calibrated by measuring the film thickness by a surface step profilometer. After growth, the substrate was cooled down to room temperature at a rate of 15°C per minute.

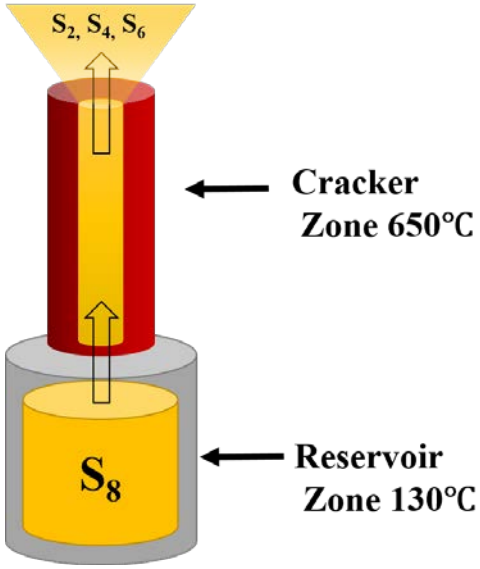

Figure 4.3 Schematic illustration of the thermal sulfur cracker cell in our experiment.

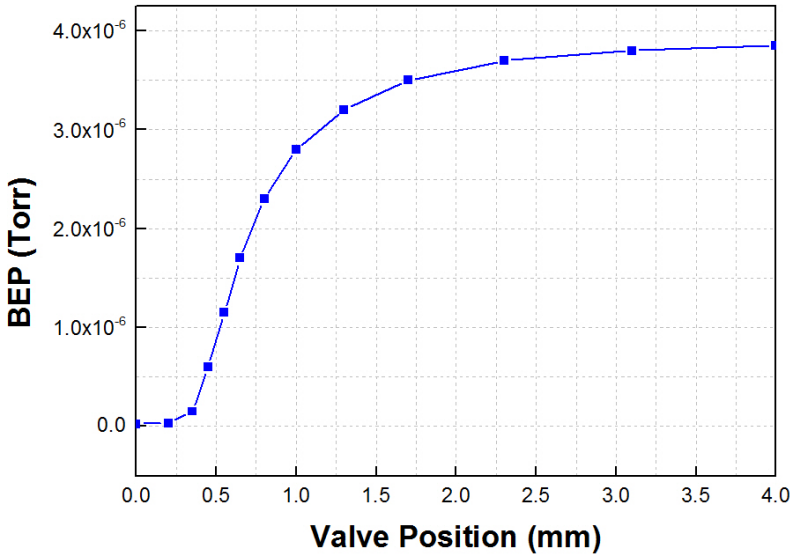

Figure 4.4 The S beam equivalent pressure (BEP) versus micrometer valve position, maintaining the reservoir and cracker temperatures at 130 ℃ and 650 ℃.

4.2 Sample Characterizations

The surface morphology of WS_2 thin film was characterized by AFM and SEM microscopy. The AFM was carried out with a Bruker NanoScope 8, employing a silicon cantilever with a 10 nm tip in tapping mode. A JEOL 6490 microscope was used to take SEM images to investigate film microstructures. The thin film crystal structure was investigated by high-resolution X-ray diffraction (HXRD) with a Rigaku SmartLab 9 kW X-ray diffractometer, using a Cu-$K_{\alpha 1}$ radiation source (λ = 1.5406 Å). Phonon behaviors were analyzed by a Raman microscope using a backscattering configuration and the excitation laser wavelength is 488 nm.

4.3 Results and Discussion

4.3.1 Optimization of Growth Temperature

Figure 4.5 shows the HXRD diffraction pattern of the WS_2 thin film grown on a mica substrate by MBE at 250°C, 350°C, 450°C and 700°C. Four strong diffraction peaks were at the angle of 14.2°, 28.6°, 43.5° and 59.4° in correspondence with the (002), (004), (006) and (008) planes of WS_2, respectively. Only the (002) family of diffraction peaks were detected in the X-ray diffraction, indicating strong preferential growth along the [001] crystal orientation. At temperatures higher than 350°C, significant enhancement of the crystallinity of the WS_2 thin films was detected. The peaks of WS_2 are sharper when growing at temperatures as high as 700°C, and the

peak intensity is higher at high temperatures, especially for the (004), (006) and (008) peaks, which indicates the better crystal quality of WS_2.

The surface morphologies of the WS_2 samples were analyzed by SEM microscopy. From the SEM image in Figure 4.6, it is apparent that the WS_2 thin films change from small vertical platelets to large parallel crystals when the growth temperature was increased from 450°C to 700°C.

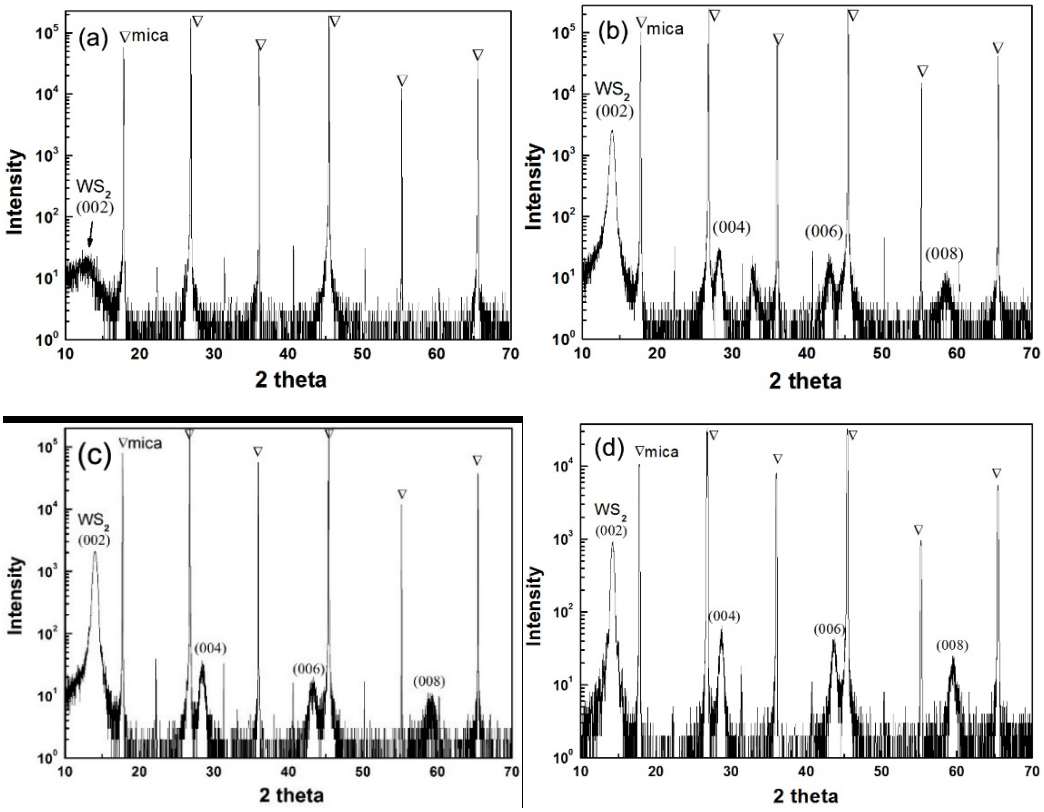

Figure 4.5 The high-resolution X-ray diffraction (HXRD) patterns of the WS_2 grown at temperatures of (a) 250°C, (b) 350°C, (c) 450 °C and (d) 700 °C by MBE.

The WS_2 polycrystalline films usually have an anisotropic structure, while the c-axis of the crystallite is parallel to the substrate (type-I) and perpendicular to the substrate

(type-II). Type-II films could be used as lubricants or absorbers in photovoltaic cells.

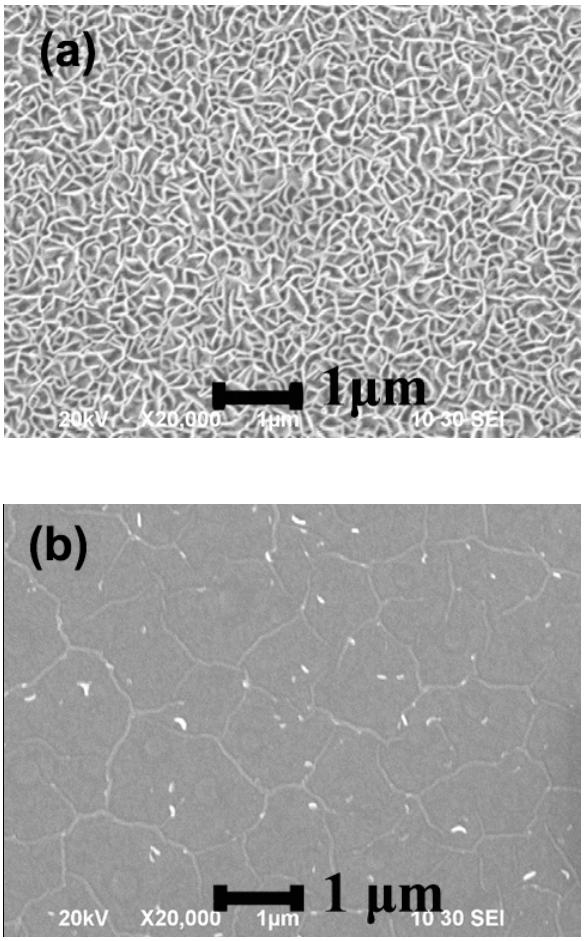

Figure 4.6 SEM image of the WS_2 thin films by MBE grown at temperatures of (a) 450 ℃ and (b) 700 ℃.

Many different kinds of methods, such as pulse laser deposition (PLD),[198] electro-deposition[199] and chemical bath deposition (CBD)[200] were employed to attempt to grow a pure type-II WS_2 thin film. However, in most cases the WS_2 film is grown in a mixed texture form by a combination of type-I and type-II crystal pieces. For our MBE growth of WS_2 at a lower growth temperature of 450°C, many random

vertical pieces (type-I) dominated at the surface of the WS_2 thin film; when the growth temperature was raised to 700°C, most of the surface crystallites changed into large parallel crystal planes (type-II). It is noted that a growth temperature of 700°C is close to the dissociation temperature of mica substrate. Hence, the highest growth temperature was limited to 700°C in the study of WS_2 grown by MBE.

4.3.2 Growth Mechanism Study of Type-II WS_2

The SEM image in Figure 4.6(b) shows many cracks in the WS_2 thin films. Such cracks resulted from lattice mismatch and the different thermal expansions of the WS_2 thin film and the growth substrate. During the high temperature growth, a large force was exerted on the continuous WS_2 film to form the cracks. The existence of the stems along the cracks indicates that cracks are likely to form when the film reaches a certain thickness. We verified our hypothesis by systematically reducing the film thickness to less than 1.5 nm. In the AFM images shown in Figure 4.7, the root mean square roughness (RMS) of the film surface decreased from 10.1 nm to 0.621 nm with the reduced film thickness from 60 nm to less than 1.5 nm. The crystals become larger with fewer vertical pieces when the thickness is reduced. The cracks were totally eliminated by reducing the thickness down to less than 1.5 nm, which indicates that at the initial stage of growth, the crystal planes should be parallel to the substrate.

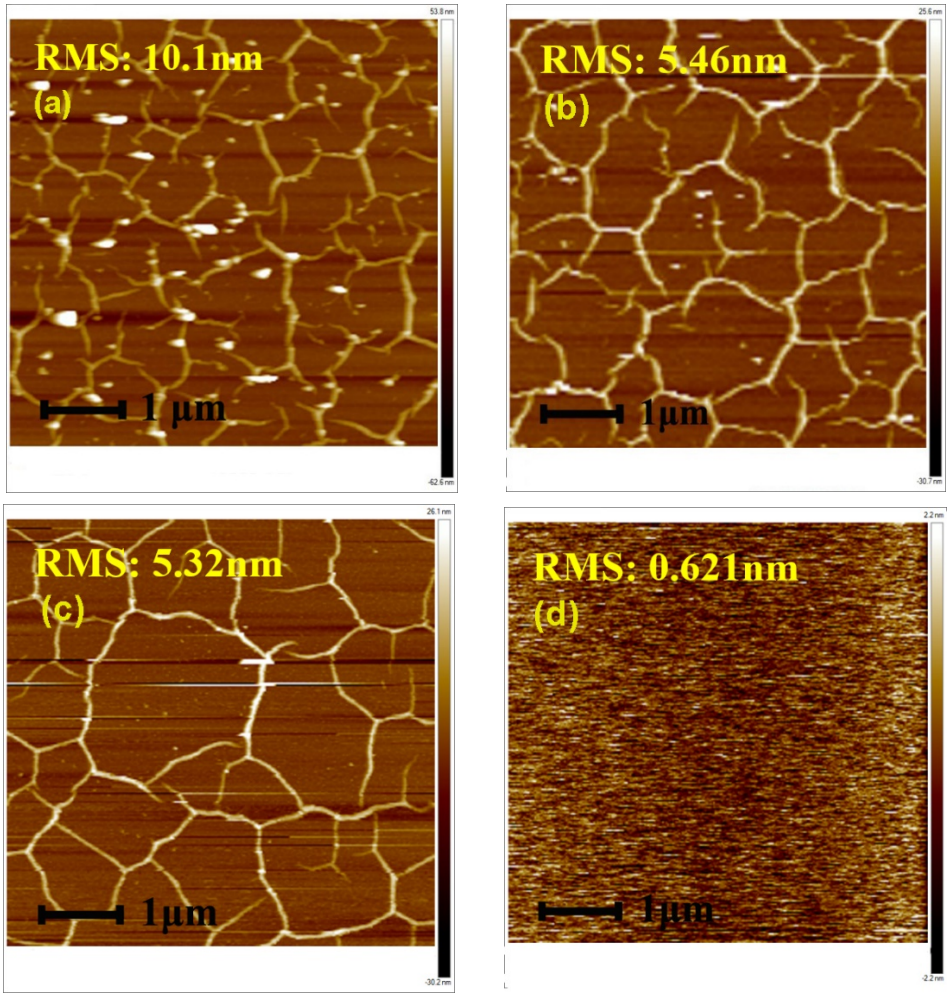

Figure 4.7 AFM images of WS_2 thin-film surfaces according to different film thickness: (a) 60 nm; (b) 30 nm; (c) 15 nm; (d) 1.5 nm. The root mean square roughness (RMS) of the film surfaces decreased from 10.1 nm to 0.621 nm, and fewer vertical platelets accompanied the reduced thickness.

Figure 4.9 shows the Raman spectrum of WS_2 thin films of different film thickness from 60 nm down to 1.5 nm. WS_2 thin film has a special thickness dependence on two typical Raman modes—A_{1g} and E^1_{2g}—which show contrary tendencies by increasing the number of layers. The A_{1g} mode represents an out-of-plane vibration including only the S atoms, whereas the E^1_{2g} mode comprises the in-

plane vibration of W and S atoms, as shown in Figure 4.8.[201, 202] The E_{2g}^{2} mode usually represents the vibration of two atom layers versus each other and is located at rather low frequencies of less than 50 cm^{-1}.[203, 204] LA(M) is considered a first-order phonon mode and the LA phonons at the M point of the Brillouin zone provide the second-order phonon mode labeled as 2LA(M).[205]

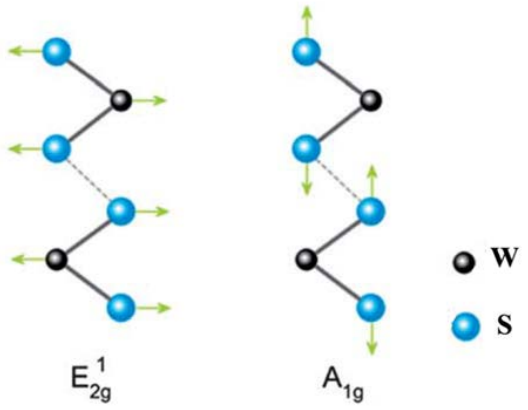

Figure 4.8 Schematic illustration of A_{1g} and E_{2g}^{1} modes of WS_2.

The differences between the A_{1g} and E_{2g}^{1} modes of different thickness are as follows:

60 nm: A_{1g} - E_{2g}^{1} = 420 cm^{-1} - 355 cm^{-1} = 65 cm^{-1}

30 nm: A_{1g} - E_{2g}^{1} = 420.5 cm^{-1} -355.5 cm^{-1} = 65 cm^{-1}

15 nm: A_{1g} - E_{2g}^{1} = 420.1 cm^{-1} -355.5 cm^{-1} = 64.6 cm^{-1}

1.5 nm: A_{1g} - E_{2g}^{1} = 419.5 cm^{-1} -357.5 cm^{-1} = 62 cm^{-1}

The enhanced interlayer interactions with the increased thickness result in the upshift of A_{1g}, whereas the downshift of E_{2g}^1 with the increased number of layers was normally owing to the elevated dielectric screening of the long-range Coulomb force that is able to weaken the recovery force on the atoms.[206]

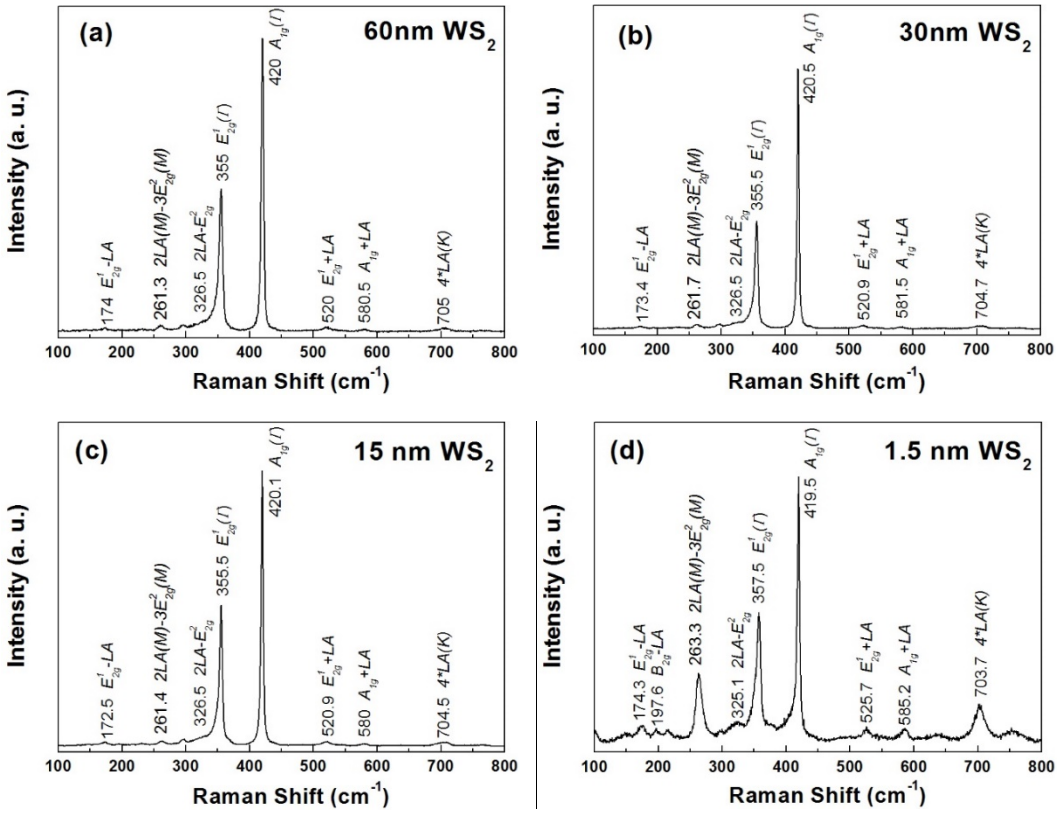

Figure 4.9 Raman spectrum of WS_2 spectrum of different film thickness from 60 nm to 1.5 nm: (a) 60 nm; (b) 30 nm; (c) 15 nm; (d) 1.5 nm.

The Raman intensity ratio of the E_{2g}^1 and A_{1g} modes ($I(E_{2g}^1)/I(A_{1g})$) increases first and then decreases with the thickness of WS_2, as shown in Figure 4.10. Different groups reported contradictory results as the intensity ratio increased or decreased or randomly varied with the thickness of the WS_2 thin film. The optical interference

between the incident and scattered light improved by the substrate are thought to possibly explain the complicated behavior of the Raman intensity ratio altered by the thickness of WS_2 thin film.[207]

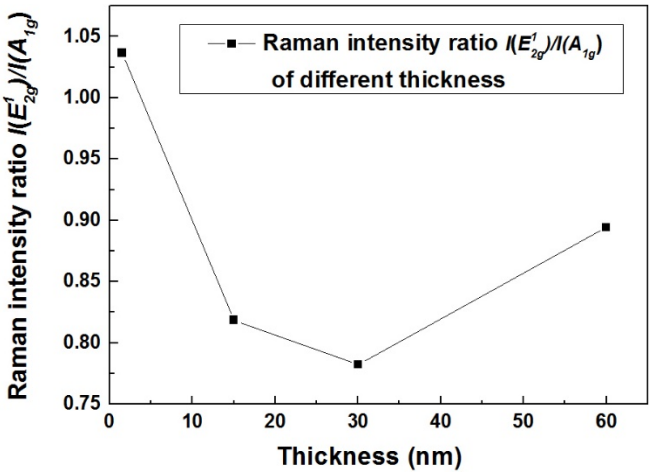

Figure 4.10 Raman intensity ratio of the E^1_{2g} and A_{1g} mode altered by the thickness of WS_2 thin film.

4.3.3 Crystal Quality Enhancement by Adjusting Sulfur

The issue of small vertical crystal pieces on the WS_2 thin film can be alleviated through providing more reactive sulfur molecules by increasing the cracker zone temperature of the S cracker cell during the deposition process. The reservoir zone temperature of the S cracker cell was increased from 130°C to 160°C and the cracker zone temperature was increased from 650°C to 750°C to provide more reactive sulfur. The cracked sulfur molecules of S_2, S_4 and S_6 by high temperature were more reactive than uncracked molecules of S_8. These more reactive S molecules have much lower

energy barriers for chemical reactions and more easily move into the crystal vacancy site, thereby leading to a reduction in the crystal defects during the WS_2 thin film deposition process. As discussed above, the WS_2 film is very smooth in the initial growth stage. As the thickness increases, more surface defects and stress accumulate and these defects can serve as seeds for the growth of random vertical crystal pieces in the later stage. More reactive S molecules can remarkably reduce the surface defects during the deposition process and finally effectively decrease the density of vertical pieces on the surface of WS_2 thin film. This is demonstrated in the AFM image of the surface of WS_2 thin film grown with different reactive sulfur fluxes in Figure 4.11.

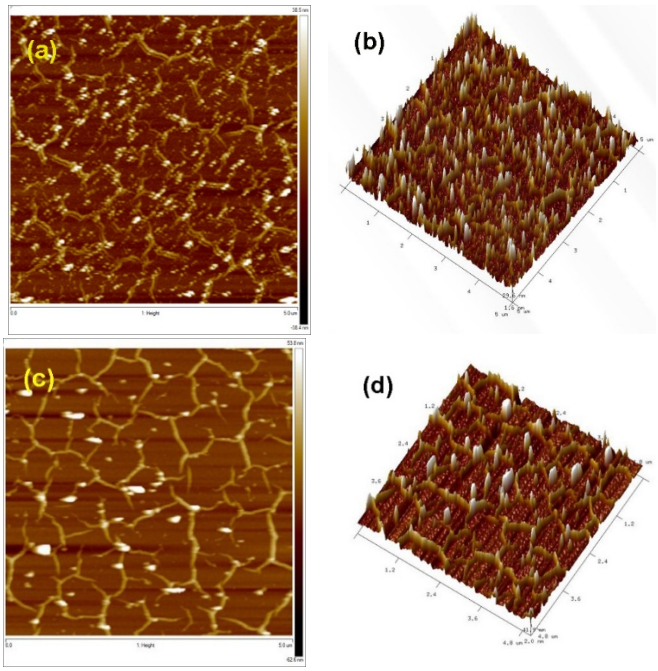

Figure 4.11 AFM image of WS_2 thin film surface grown with different reactive sulfur fluxes: (a) (b) normal sulfur flux; (c) (d) more reactive sulfur flux provided during deposition.

Figure 4.12(a) shows that the HXRD rocking curve of the WS_2 thin film changes from a wide peak to a sharp peak with a wide base by increasing the amount of reactive sulfur molecules with the increased cracker temperature. The FWHM is remarkably decreased from 1.0151 to 0.1319 indicating high quality WS_2 crystals were formed by providing more reactive sulfur source during the deposition process. As mentioned above, by increasing the temperature of the cracker cell, sulfur molecules changes from S_8 to S_2, S_4, S_6 which are more reactive to fill into the crystal vacancy site to remarkably reduce defects in the WS_2 crystals. It is noted that, by providing more reactive sulfur, the peak of the rocking curve can be divided into a sharp peak embedded with another wide peak by using the Voigt profile function. The fitting result (red solid line) exhibits very fine agreement with the measured diffraction pattern (green dot), as shown in Figure 4.12(b). The FWHMs of the sharp and wide peaks were calculated as 0.1159° and 1.5406°, thereby indicating that high quality large grains co-exist with small- to medium-sized crystallites that have a higher level of disorientation. The wide peak is generally related to disorientation among sub-grains because small-sized sub-grains will increase the possibility of sub-grain disorientation, and smaller-sized crystallites are another factor that widen the FWHM in rocking curves. The sharp peak is related to the appearance of high quality WS_2 crystals in the thin film by providing more reactive sulfur molecules during the deposition process. However, the intensity ratio of the sharp peak and the wide peak is 0.258 indicating that the high quality WS_2 crystals is only about 20% of the total

volume and the film still suffered from a high level of disorientation. Thus, more reactive sulfur source, higher temperature are required to enhance the crystal quality of the WS_2 thin film.

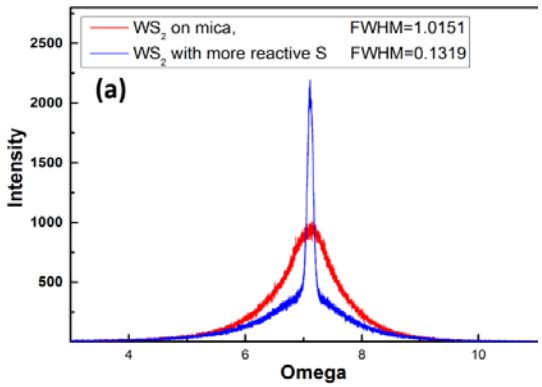

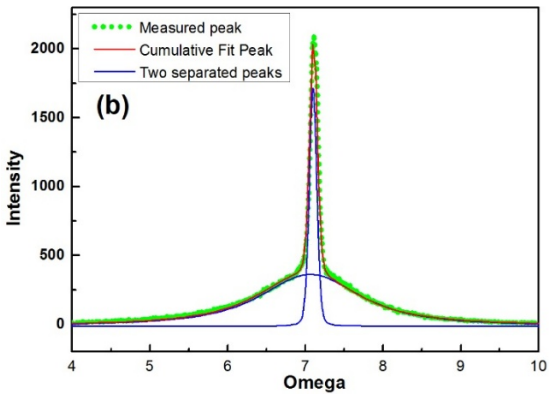

(c)

		Value	Standard Error
Peak1(Voigt)	y0	-13.72036	0.25989
	xc	7.04466	6.79545E-4
	A	880.84569	3.10839
	wG	0.54476	0.01563
	wL	1.33571	0.00927
	FWHM	1.54064	0.00426
Peak2(Voigt)	y0	-13.72036	0.25989
	xc	7.1142	4.03884E-5
	A	227.54901	0.63964
	wG	0.10549	3.8075E-4
	wL	0.01878	6.13265E-4
	FWHM	0.1159	1.07134E-4

Figure 4.12 (a) The full width at half maximum (FWHM) of the rocking curve by using different amounts of reactive S atoms; (b) The peak of the rocking curve was separated into a sharp peak that was embedded with another broader peak. The fitting result (red solid line) shows excellent agreement with the measured diffraction pattern (green dot); (c) Fitting parameters by using the Voigt profile function.

4.4 Summary

In the X-ray diffraction of the WS_2 thin film, only the (002) family diffraction peaks were detected, indicating preferential growth along the [001] crystal orientation of the WS_2 film. At substrate temperatures higher than 350°C, significant enhancements in the crystallinity of the WS_2 thin films are detected. The peaks of WS_2 are sharper at higher growth temperatures up to 700°C. The WS_2 thin films change from small vertical platelets (type-I) to large parallel crystals (type-II) when the growth temperature is increased from 450 °C to 700 °C. With decreased film thickness, the root mean square roughness of the film surface decreases from 10.1 nm to 0.621 nm, and the crystals become larger with fewer vertical pieces. The full width at half maximum of the rocking curve was reduced to 0.13° by increasing the amount of reactive S atoms.

CHAPTER 5 CHEMICAL VAPOR DEPOSITION OF WS_2

Chemical vapor deposition (CVD), another large-scale thin film growth technique, is extensively used for the growth of large-area TMDC thin films.[83, 208] In this thesis, the CVD technique was adopted to grow WS_2 thin films, using WO_3 films as the precursor, on sapphire substrates. Figure 5.1 shows that WS_2 thin films commonly exist as a mixture of type-I and type-II crystals with their c-axis parallel or perpendicular to the surface of the substrate. Highly textured type-II WS_2 thin films were successfully synthesized on sapphire substrates by using a thin Ni layer as texture promoter, because the formation of molten NiS_x droplets during the deposition process has the significant effect of minimizing the interface energy of the film and the substrate, resulting in the van der Waals rheotaxy (vdWR) of WS_2.[209, 210] Our experiment proved that the crystal quality of WS_2 thin films can be greatly enhanced by utilizing a pre-deposited thin Ni layer as texture promoter. We systematically investigated the growth of WS_2 thin films by the CVD technique on sapphire and n-type GaN substrates.

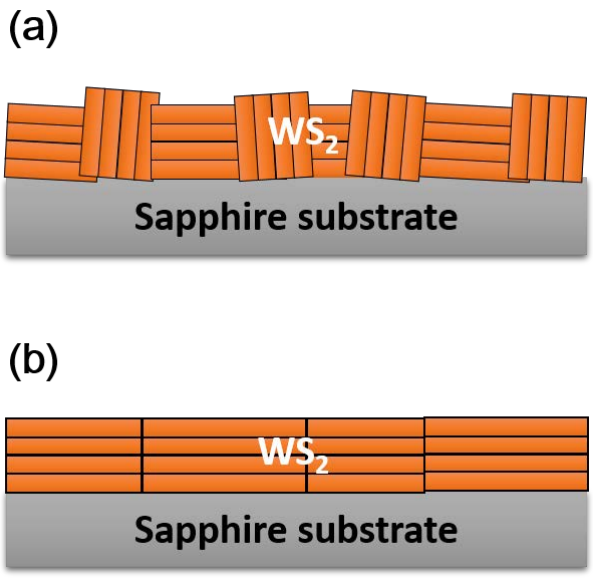

Figure 5. 1 Schematic drawing of (a) the mixture of type-I and type-II WS_2 crystallites and (b) pure type-II WS_2 crystallites.

5.1 Experimental Details

Three types of WS_2 films were deposited at the temperature of 1000°C via the CVD method: 1) WS_2 thin films grown on sapphire substrates without using a thin Ni layer as texture promoter (type A film), 2) WS_2 thin films grown on sapphire substrates using a 5 nm Ni layer as texture promoter (type B film), and 3) WS_2 thin films grown on n-type GaN substrates using a 5 nm Ni layer as texture promoter (type C film). To grow type A films, the sapphire substrate was cleaned by ultrasonic cleaning in acetone, isopropanol and deionized water before the growth of the WO_3 layer by e-beam evaporation. To grow type B films, a 5 nm Ni layer was deposited by e-beam evaporation before depositing the WO_3 layer. To grow type C films, an n-

type GaN thin layer on sapphire was used as the substrates for the deposition of a 5 nm Ni layer followed by the WO_3 layer by e-beam evaporation. The WO_3 film was 400 nm thick, as measured by a quartz crystal thickness detector during the deposition process. The thickness of the film was also confirmed by a surface profiler after growth. Thereafter, the samples were transferred to a tube furnace to grow the WS_2 layers. The growth substrates and sulfur pieces were placed at different positions inside the quartz tube, as shown in Figure 5.2. A quartz boat filled with 5 g sulfur pieces (99.998%, Sigma-Aldrich) was placed upstream, while the substrates were placed downstream. The sulfur source was heated by an independent heating belt wrapped around the quartz tube.

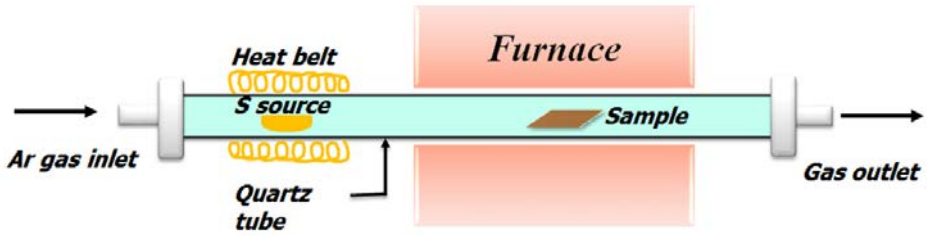

Figure 5.2 Schematic illustration of the experimental CVD setup.

Ultra-high-purity Ar gas was employed as the carrier gas, and its flow rate was maintained at 100 sccm during the deposition process by using a high-precision mass flow controller (MFC). The pressure in the chamber of quartz tube was pumped to

3×10^{-2} torr. The reaction zone, where the substrates were located, was heated to 1000°C for 5 hours to ensure that the WO_3 precursor thin layer completely reacted with the S vapor. The temperature of the entire reaction process is shown in Figure 5.3. Following that, the furnace was cooled to room temperature at a rate of 3°C/min. The final thickness of the WS_2 film was approximately 400 nm, as measured by a surface profiler.

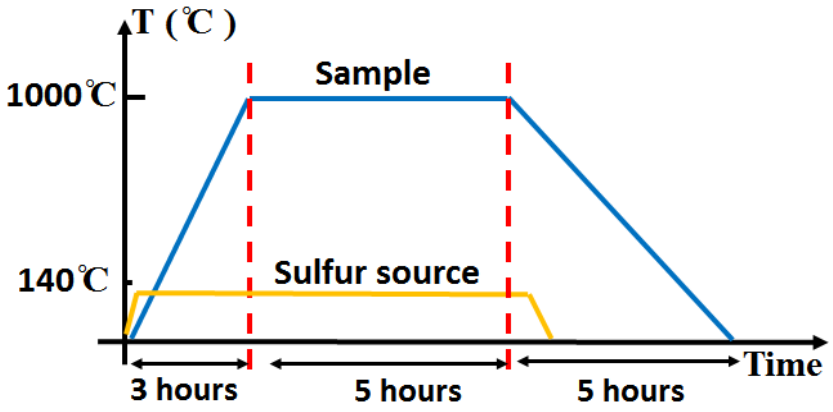

Figure 5.3 Temperature profile for the growth of the WS_2 thin films.

5.2 Sample Characterizations

The surface morphology of the WS_2 thin film was characterized by scanning electron microscopy (SEM). A JEOL 6490 microscope was employed to obtain SEM images to investigate the microstructure of the WS_2 thin films, and the electron accelerating voltage was 30 kV. The crystal structure of the WS_2 thin film was

investigated by high-resolution X-ray diffraction (HXRD), employing a Rigaku Smartlab X-ray diffractometer with a Cu-$K_{\alpha 1}$ X-ray source (λ = 1.5406 Å). The phonon behaviors were characterized by using a backscattering Raman microscope, and the excitation wavelength of the laser was 488 nm.

In 2D layer crystals, while the electron transportation exists in both vertical and lateral directions, the lateral transportation rate is commonly faster than the vertical transportation rate.[211] However, our layer structure WS_2 thin films are polycrystalline thin films which contain a large number of vertical grain boundaries and provided the paths for the vertical electron transportation across different crystal layers. Thus, our 400 nm WS_2 thin films can be considered as typical 3D semiconductor thin films for the resistivity and Hall mobility measurements. Additionally, the WS_2 thin films with the thickness more than 20 layers are commonly considered as bulk materials as they exhibit the electronic and optical properties of the bulk materials. For example, the 20-layer WS_2 thin film had an indirect energy bandgap of bulk materials of 1.3 eV, while the monolayer WS_2 crystal showed a direct energy bandgap of 2.1 eV.[50-52] In addition, the Raman spectra of the WS_2 thin films with thickness more than 20 layers are same as the bulk WS_2 crystals, whereas the monolayer WS_2 crystal showed a smaller difference between $\boldsymbol{E}_{2g}^{1}$ and $\boldsymbol{A}_{1g}$ peaks than that of the bulk materials.[206] Therefore, standard methods for characterization of resistivity and hall mobility for the bulk materials were employed.

5.3 Results and Discussion

5.3.1 Surface Morphology of the WS_2 Thin Film

To change the crystal structure from WO_3 to WS_2 by replacing the O atoms with S atoms, high reaction energy is required for the sulfurization of the thin WO_3 layer. Therefore, the CVD growth of WS_2 requires a high sulfurization temperature (between 800°C and 1000°C). In general, random crystallites with c-axis perpendicular or parallel to the surface of the substrate normally exist in WS_2 film grown at low temperatures. Larger layered crystals with c-axis perpendicular to the substrate surface are favored by high sulfurization temperatures. Sapphire is a good choice of substrates to grow WS_2 due to its good thermal stability and chemical inertness in high temperatures up to 1000°C. Furthermore, sapphire has a similar thermal expansion coefficient as WS_2, which avoids large strains at the growth interface.[212] In depth studies were conducted on three types of WS_2 films: 1) WS_2 thin films grown on sapphire substrates without a Ni layer (type A film), 2) WS_2 thin films grown on sapphire substrates using a pre-deposited 5 nm Ni layer as texture promoter (type B film), and 3) WS_2 thin films grown on n-type GaN thin films using a pre-deposited 5 nm Ni layer as texture promoter (type C film).

SEM was utilized to analyze the surface crystal structure of the WS_2 thin films. Figure 5.4 shows the SEM images of the type A and type B WS_2 thin films grown at different temperatures of 900°C and 1000°C for 5 hours. During the CVD growth of

WS_2, at a lower temperature of 900°C, the crystallization process was not completed, as no obvious crystallites were observed. The carrier mobilities of the type A and type B WS_2 thin films grown at 900°C were only 0 and 1.75 $cm^2/V \cdot s$.

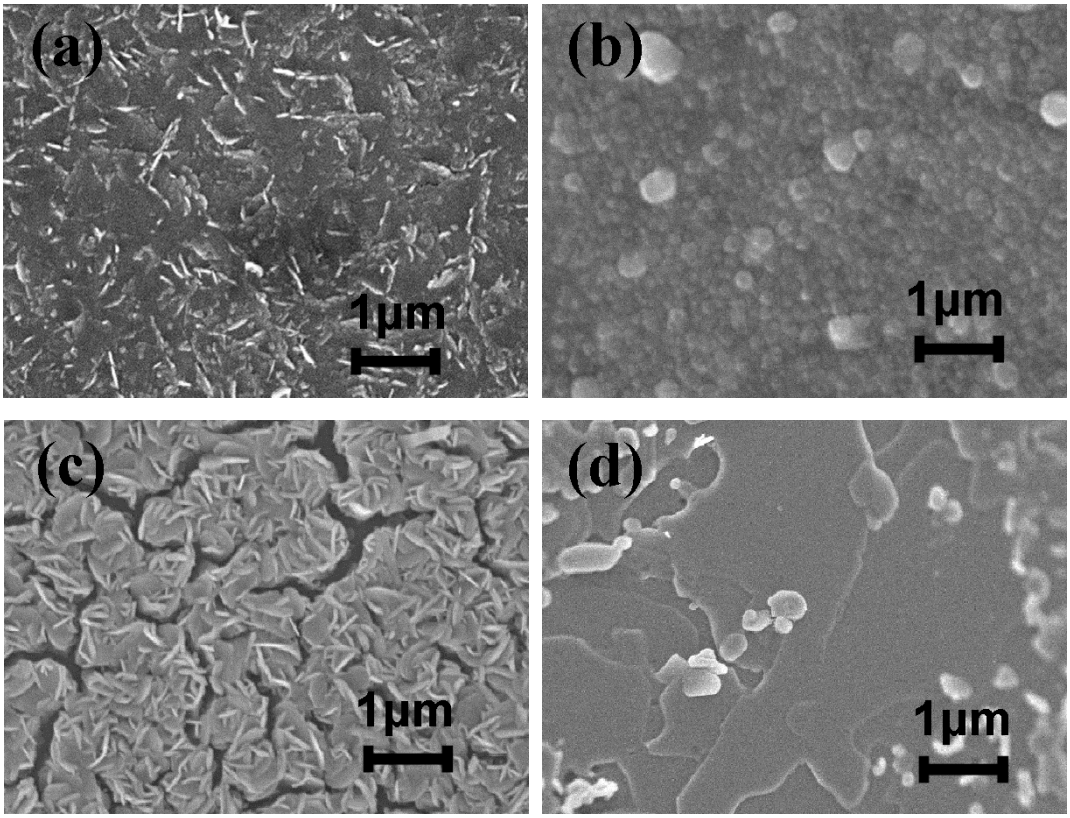

Figure 5.4 SEM images of WS_2 thin films grown (a) without Ni promoter (type A film) and (b) with Ni promoter (type B film) at 900°C and WS_2 thin films grown (c) without Ni promoter (type A film) and (d) with Ni promoter (type B film) at 1000°C.

When the growth temperature was increased to 1000°C, the degree of crystallinity was greatly increased. The carrier mobilities of the type A and type B WS_2 thin films were remarkably increased to 3.25 $cm^2/V \cdot s$ and 63.3 $cm^2/V \cdot s$.

Three types of WS_2 films were grown at the optimized temperature of 1000°C,

and their surfaces and cross sections were investigated by SEM, as shown in Figure 5.5. Many micro cracks and type-I crystal pieces can be observed on the type A film, as shown in Figure 5.5a. However, the SEM image in Figure 5.5b shows that the vdWR-grown WS_2 thin film (type B film), using a 5 nm pre-deposited Ni layer as texture promoter, has a uniform surface with large layered type-II crystals and a few small crystallites distributed on the surface.

At the initial growth stage, surface diffusion of the adatoms cannot be sufficiently achieved, which leads to numerous dangling bonds at the surface and grain boundaries between the crystallites. Consequently, the dangling bonds bond to the substrate surface, forming type-I WS_2 crystallites. In comparison with the type A film, the carrier mobility of the type B film was greatly enhanced from 3.25 cm^2/Vs to 63.3 cm^2/Vs with the carrier concentration of 7.12×10^{16} cm^{-3}. The crystallinity of the type B film was greatly improved by using the Ni texture promoter, which forms liquid NiS_x at its melting point of 637°C. The liquid NiS_x exists at the grain boundaries of the WS_2 crystallites during sulfurization.[209, 210] Liquid NiS_x droplets can be considered as the nucleation seeds for liquid epitaxy, which lead to the horizontal growth of WS_2 crystals with a greatly reduced micro-strain and low level of defects.

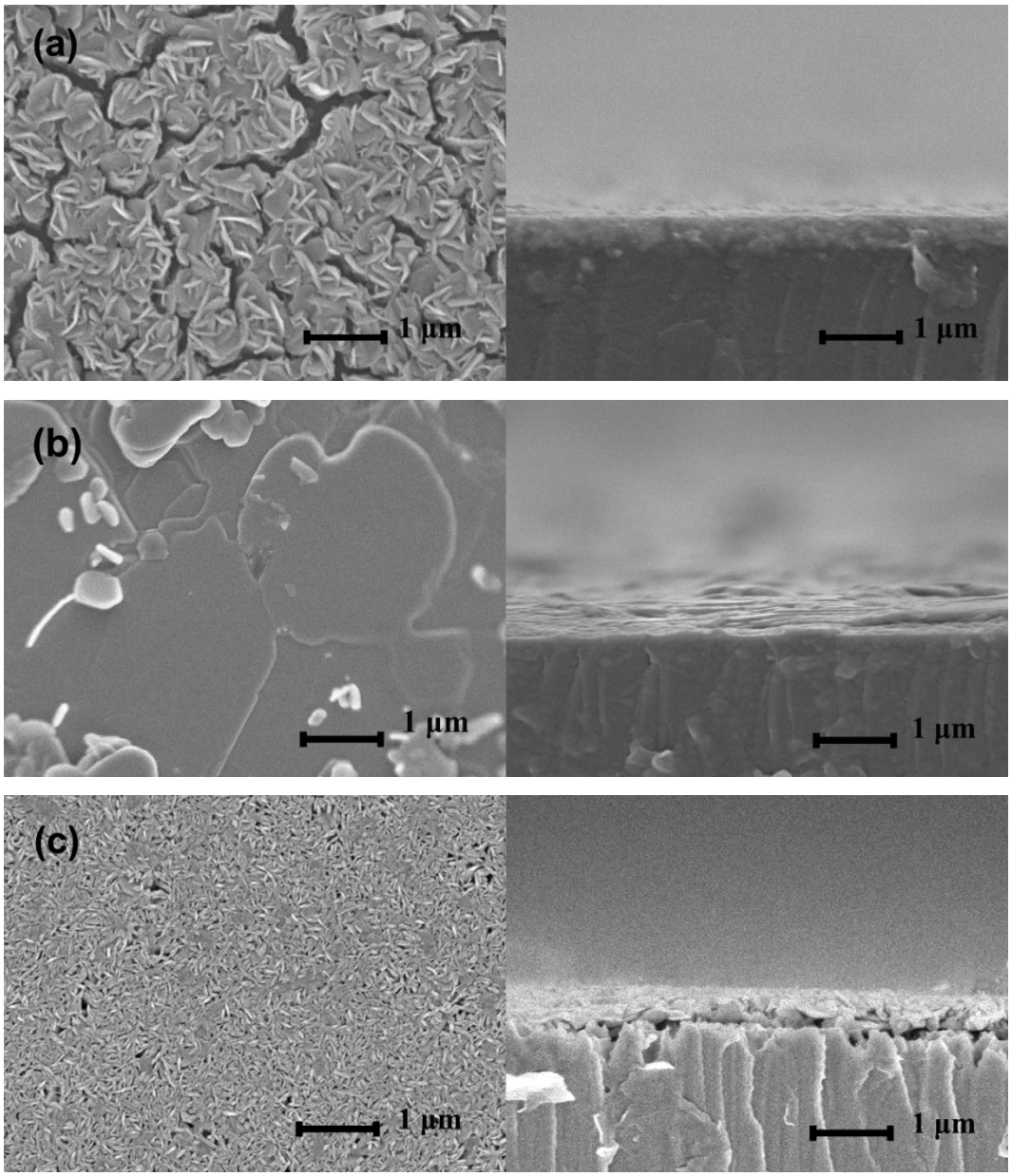

Figure 5.5 SEM images of the surfaces and cross sections of the WS_2 thin films grown on a sapphire substrate (a) without Ni promoter (type A film) and (b) with Ni promoter (type B film) and (c) WS_2 film grown on n-GaN/sapphire substrate with Ni promoter (type C film).

In addition, the thin Ni layer, as the texture promoter, has the reliable and stable effect of increasing the carrier mobility of the WS_2 thin film. The carrier mobility of the

type B WS_2 film fluctuated at an acceptable level. Table 5.1 shows the carrier mobility of three different type B WS_2 films using the same growth parameter.

Table 5.1 Carrier mobility of three different WS_2 thin films grown with Ni texture promoter under the same growth conditions.

WS_2 thin film with Ni promoter	**Carrier mobility [cm^2/Vs]**
1	**63.3**
2	**58.7**
3	**60.1**

The type C film is composed of compact small crystallites. Though the thermal expansion coefficients and lattice constant of the GaN and sapphire substrates are similar to those of the WS_2 film,[213, 214] the thermal stability of sapphire at the temperature of 1000°C is considerably better than that of GaN. The sapphire shows chemical inertness and excellent thermal stability at high temperatures of 1000°C.[215] Nevertheless, the degradation of the GaN crystalline at 1000°C has been proven by Raman spectroscopy and photoluminescence (PL) spectroscopy[216] and is thought to be the major reason resulting in the substandard crystalline quality of WS_2 deposited directly on GaN. Therefore, the transfer of p-type WS_2 onto an n-type material should be a favorable approach to fabricate p-n junctions, as this method allows a broader selection of n-type materials, including those unlikely to endure high temperatures.

5.3.2 Crystal Quality of the WS_2 Thin Film

The high-resolution X-ray diffraction (HXRD) patterns of the type A and type B films are shown in Figure 5.6a and 5.6b, respectively. Four diffraction peaks at 14.4°, 28.9°, 43.9° and 59.8°, indicating the (002), (004), (006) and (008) crystal planes of WS_2 film, are detected for the type B WS_2 film. Nevertheless, only two major peaks with much lower intensity are detected for the type A WS_2 film. The (002) family diffraction peaks can be observed in the HXRD pattern of the type B film, indicating preferential growth in the [001] crystal orientation. The full width at half maximum (FWHM) of the (002) peaks of the type A and type B films were 0.566° and 0.189°, respectively. This shows remarkable improvements of the type B film quality. The HXRD pattern also indicates that there are no diffraction peaks corresponding to the NiS_x phase in the film, which implies that the percentage of the NiS_x phase in the WS_2 film is extremely low. The residual NiS_x phases are commonly thought to distribute at the grain boundaries and do not have significant effects on the electronic properties of the WS_2 film.[209] The intensity of the HXRD pattern of the type C film is considerably lower than that of either the type A or type B films, as shown Figure 5.6c. The FWHM of the (002) WS_2 peak of the type C film is 0.255°, which is 35% broader than that of the type B film, implying the lower crystallinity of the type C film.

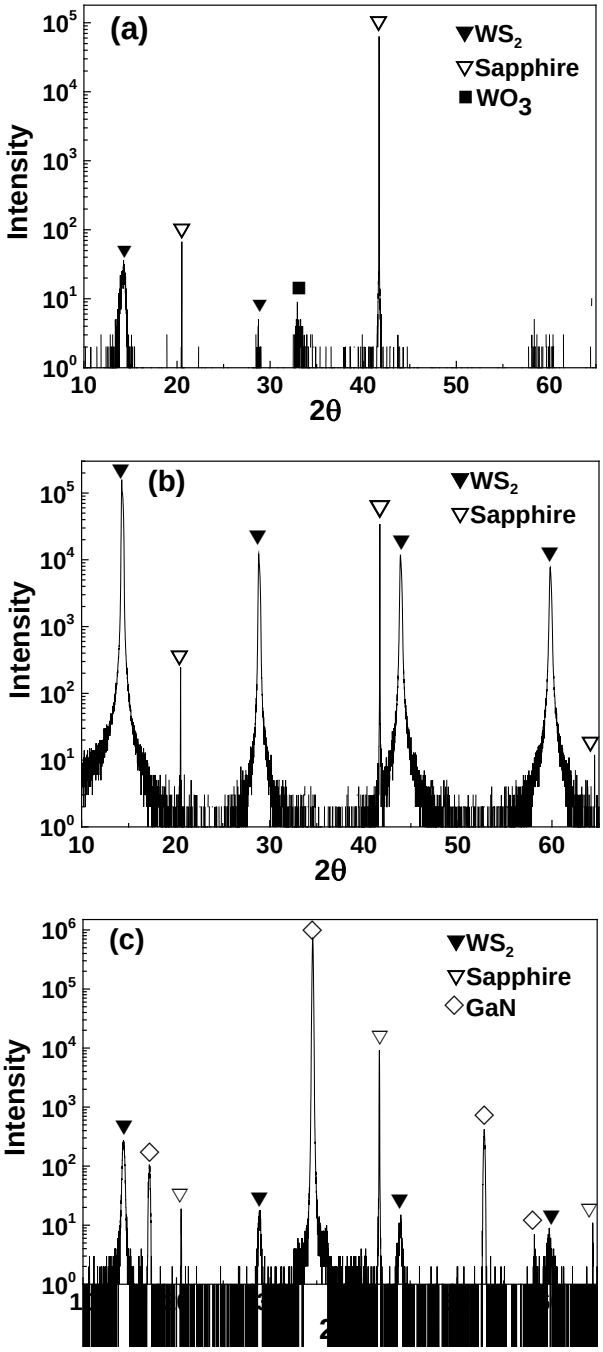

Figure 5.6 HXRD patterns of WS_2 grown (a) without and (b) with thin Ni layer as texture promoter on a sapphire substrate and (c) WS_2 grown with thin Ni layer as texture promoter on an n-type GaN/sapphire substrate.

The HXRD result is consistent with the Raman spectrum shown in Figure 5.7.

The A_{1g} mode at 421.8 cm^{-1} corresponds to the out-of-plane vibration of the S atoms,

while the E_{2g}^1 mode at 356.9 cm^{-1} corresponds to the in-plane vibration of both W and S atoms, and the second-order phonon mode is labelled 2LA.[217-219] The FWHM of the A_{1g} mode of the type A WS_2 film is 4.03 cm^{-1}, which is 52% broader than that of the type B WS_2 film of 2.65 cm^{-1}. The intensity ratio of the E_{2g}^1 mode to the A_{1g} mode, $I(E_{2g}^1)/I(A_{1g})$, of the type B WS_2 film is 0.617, while the intensity ratio for the type C film is lower at 0.454 (Figure 5.8), indicating that the in-plane vibration was depressed in comparison with the out-of-plane vibration, owing to the small crystallites and disoriented crystallites in the type C WS_2 film.

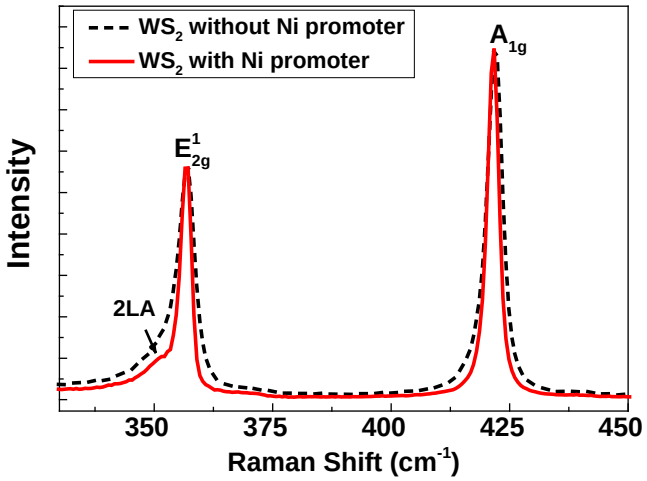

Figure 5.7 Raman spectra of WS_2 grown without (black dashed line, type A film) and with (red solid line, type B film) Ni promoter on a sapphire substrate.

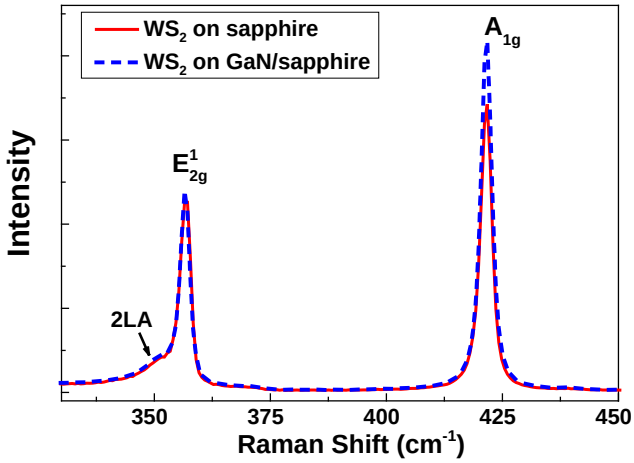

Figure 5.8 Raman spectra of WS_2 grown on a sapphire substrate (red solid line, type B film) and on a GaN/sapphire substrate (blue dashed line, type C film) with Ni promoter.

5.3.3 WS_2 Growth on SiO_2/Si Substrates

We also compared the effect of different substrates on WS_2 growth by the CVD method, such as a 300 nm SiO_2/Si substrate. During a long, 5 hour sulfurization at the high temperature of 1000 ℃, Si reacted with S to form SiS_x, which is in the gas phase at high temperature, resulting in holes on the Si substrate, as shown in Figure 5.9. Therefore, the 300 nm SiO_2/Si substrate is not suitable for large-scale WS_2 growth by the CVD method. Considering that the films are actually produced from a chemical reaction, the selected substrate must be inert to chemical reaction with WO_3, Ni and S at the temperature of 1000 ℃. To avoid strain at the interface caused by a large difference in the expansion coefficients, the substrate and film must also have comparable expansion coefficients. Considering these requirements, the most

suitable substrates are sapphire and mica. Unfortunately, mica is not stable at temperatures above 700℃, due to the loss of water molecules in between the layers of the layered structure of mica, which leads to the destruction of the surface structure.

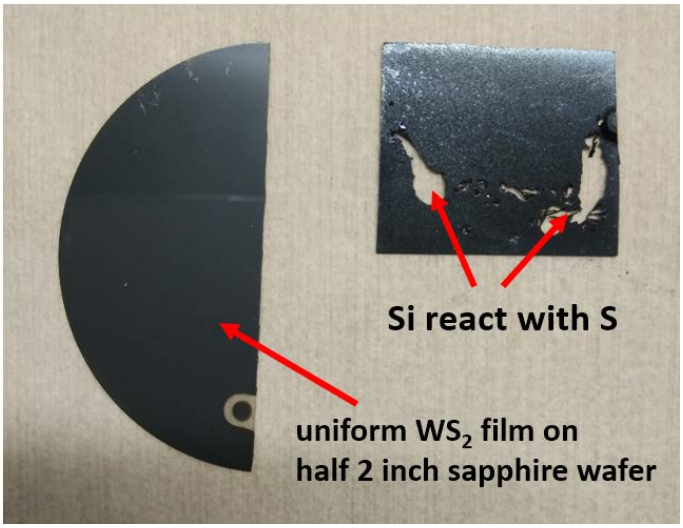

Figure 5.9 Uniform WS_2 film on half of a 2 inch sapphire wafer and holes on the Si substrate formed from a reaction between Si and sulfur.

5.4 Summary

High-quality p-type WS_2 thin films were grown by the CVD technique using a thin Ni layer as texture promoter and showed carrier mobility as high as 63.3 cm^2/Vs. Without the Ni promoter, the WS_2 film consisted of numerous randomly oriented crystallites, and a large number of micro cracks were observed on the film surface, while the WS_2 thin film with Ni promoter was found to be uniform with large layered crystals with c-axis oriented perpendicular to the substrate. The liquid NiS_x phase during the sulfurization process served as the liquid crystallization seed for van der

Waals rheotaxy, resulting in the horizontal growth of WS_2 layered crystals with enhanced crystal size. The intensity of the X-ray diffraction (XRD) peaks of the WS_2 film grown using Ni promoter are much stronger than those of the film without Ni promoter, and the full width at half maximum (FWHM) of the WS_2 film grown using Ni promoter is only about one third of that of the film without Ni promoter, indicating the enhanced crystallinity. Degradation of the crystalline of the GaN layer at 1000 °C led to poor WS_2 film quality during the 5 hour growth process.

CHAPTER 6 FABRICATION OF WS_2/GAN P-N JUNCTION BY WAFER-SCALE WS_2 THIN FILM TRANSFER

The majority of semiconductors and conductors are unstable during the high-temperature growth of WS_2 at 1000°C. This imposes significant restrictions on the fabrication of WS_2-based heterojunctions and hence significantly constrains the WS_2 thin films application. However, transfer of the as-grown WS_2 thin film to an appropriate substrate is an effectual method to overcome this restraint. The wafer-scale transfer of WS_2 films is important for electronics and optoelectronics applications, as WS_2-based heterojunctions can be fabricated without worrying about lattice mismatch and different thermal coefficients and the growth parameters do not need to be optimized for a specific substrate. The transfer of graphene has been extensively studied; nevertheless, the process cannot be simply followed for the transfer of WS_2, because the graphene transfer technique uses substrate etchants, for instance, HF and KOH, which commonly contaminate or damage the film surface, which results in considerable degradation in the device performance.[220, 221] Hence, we employed an etching-free transfer method to exfoliate the wafer-scale WS_2 thin film from the sapphire substrate and transfer the exfoliated film to another target substrate. This etching-free transfer approach greatly broadens the applications of WS_2 in electronic devices. The wafer-scale etching-free transfer of WS_2 thin films

was studied in detail. By systematic optimization of the transfer processes, wafer-scale transfer of WS_2 thin films can be achieved without producing any noticeable cracks or wrinkles. Additionally, we accomplished the fabrication of WS_2/GaN p-n junctions using the transfer method, and the devices showed considerably reduced leakage current density in comparison with the direct growth of WS_2 on GaN p-n junctions.

6.1 Experimental Details

6.1.1 Wafer-Scale Transfer of WS_2 Thin Films

An etching-free transfer method was adopted to transfer the wafer-scale WS_2 thin films to other substrates with no noticeable cracks or wrinkles. Utilizing the different surface properties of the growth material and substrate, the hydrophobicity of the WS_2 film and the hydrophilicity of the sapphire substrate, water molecules can be introduced into the interface between the WS_2 film and the sapphire substrate to separate the film from the substrate. The carrier polymer and microstructure (type-I or type-II textured crystallites) of the film are the two most critical factors for the wafer-scale exfoliation of WS_2 films from sapphire substrates. Our results showed that type-II textured WS_2 is vitally important for the successful wafer-scale etching-free exfoliation. WS_2 thin films composed of type-I crystallites cannot be completely exfoliated due to the strong forces between the dangling bonds of the type-I textured

crystallites and the surface of the substrate. This method does not use any corrosive chemical etchant, making it possible to reuse the sapphire substrates. The transfer process was carried out as follows. A polystyrene solution was spin-coated on the WS_2 film at a speed of 4000 rpm. Then, the sample was baked at a temperature of 80 °C for 10 minutes to evaporate the solvent from the polymer. The polymer surface was cut along the edge using a sharp cutter to let water to penetrate into the interface between the film and the substrate. Then, the sample was immersed in deionized water for a few minutes to separate the polymer-coated WS_2 film from the sapphire substrate. By using this technique, the polymer-coated WS_2 film was completely seperated from the sapphire substrate and afterwards transferred to the target substrate. In comparison with the general transfer method for graphene, which permits the transfer of only the back surface (the growth interface) of the film onto the target substrate, our method enables the transfer of thin films with both the back surface and the top surface onto the target substrate. For back surface transfer, the polymer-coated WS_2 film was picked up by the target substrate and then baked at 70 °C for 15 minutes for removing water residue. Following that, a baking at the temperature of 130 °C for 15 minutes was performed to spread the wrinkles in the polymer layer and achieve good adhesion. Finally, the polystyrene layer was dissolved in toluene for 30 minutes. For top surface transfer, immerse the polymer-coated WS_2 film in toluene for 30 minutes to remove the polystyrene layer. The free-standing WS_2 film maintained its integrity and turned over in the toluene solution. Then, the overturned WS_2 film was

picked up by a temporary substrate and washed with acetone, IPA and DI water to remove the toluene. Finally, the free-standing WS_2 thin film was transferred to the target substrate and baked at the temperature of 70 °C for 15 minutes, followed 130 °C for 15 minutes to achieve strong adhesion.

6.1.2 Fabrication of WS_2/GaN p-n Junctions

To demonstrate the practicability of the etching-free transfer approach to fabricate p-n junctions, we transferred the type B WS_2 film onto an n-type GaN substrate. The doping concentration of the n-type GaN layer is approximately 3×10^{18} cm^{-3}. For comparison, a p-type WS_2 layer was directly grown on an n-type GaN layer using a thin Ni layer as texture promoter. An Ni/Au (5 nm/300 nm) bi-layer was evaporated by e-beam to form ohmic contact with the top surface of the WS_2 film, and a 300 nm Al layer was evaporated on the back surface of the WS_2 film to form ohmic contact.

6.2 Sample Characterizations

The I-V and C-V characteristics of the WS_2/GaN p-n junctions were measured using an Agilent B1500A semiconductor device parameter analyzer. The crystal structure of the WS_2 thin film was characterized by high-resolution X-ray diffraction (HXRD), employing a Rigaku Smartlab X-ray diffractometer with a Cu $K_{\alpha1}$ X-ray source (λ = 1.5406 Å) and a two-bounce, hybrid Ge (220) monochromator. The

phonon behaviors were analyzed using a backscattering Raman microscope, and the excitation wavelength of the laser was 488 nm. XPS measurements were performed on a SKL-12 spectrometer with an Al K_α X-ray source. The XPS spectra were calibrated with the C 1s peak (284.6 eV) to determine the valence band maximum (VBM) relative to the Fermi level.

6.3 Results and Discussion

6.3.1 Wafer-Scale Transfer of WS_2 Thin Films

Hydrophilic or hydrophobic property of a material surface depends on its surface energy. The surface energy is determined by the surface chemical composition, minimum surface energy will produce maximum hydrophobic nature and vice versa. Metal oxides are typically hydrophilic because their electronic structure favors the formation of hydrogen bonds with water molecules. For instance, Al_2O_3 is a hydrophilic material, as the Al atoms covering the surface of Al_2O_3 are electron deficient and can form hydrogen bonds with interfacial water molecules.[222] However, MoS_2 and WS_2 crystals are chemically inert and show a hydrophobic nature due to their low surface energy.[223] Utilizing the different surface properties of WS_2 and the sapphire substrate, water molecules can be introduced into the interface between the WS_2 thin film and the sapphire substrate, as shown in Figure 6.1. Surface tension forces will separate the WS_2 thin film from the substrate, since water has a

high surface tension of 72.8 mN/m at 20 °C compared to that of most other liquids.[224]

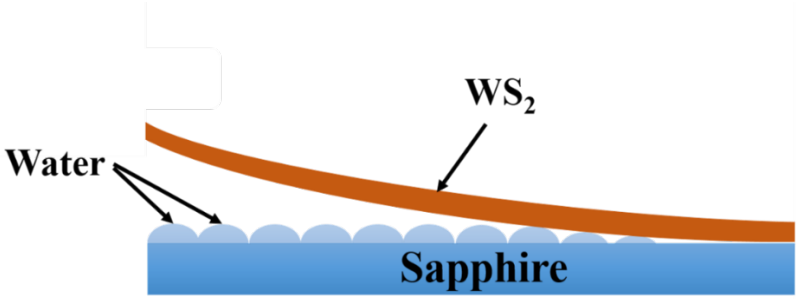

Figure 6.1 When water penetrates into the interface of the WS_2 film and the sapphire substrate, surface tension forces will separate the WS_2 thin film from the substrate.

Employing this method, wafer-scale WS_2 thin films can be sepeated from the sapphire substrate and transferred to other flat substrate keeping integrity. The exfoliation of type A films cannot be achieved on the wafer-scale owing to the coexistence of type-I and type-II crystallites. The etching-free transfer is superior due to the preservation of the high integrity of the film without introducing any types of cracks or wrinkles, in comparison with ordinary chemical etching transfer approaches, such as the transfer of graphene.[81, 225] Figure 6.2 shows the following: (a) a type B WS_2 thin film grown on a 2 inch sapphire substrate, (b) the exfoliated polystyrene-coated WS_2 thin film floated on the surface of water, (c) pick up of the WS_2 thin film with a 4 inch SiO_2/Si wafer, and (d) the 2 inch WS_2 thin film transferred to the SiO_2/Si wafer without cracks or wrinkles.

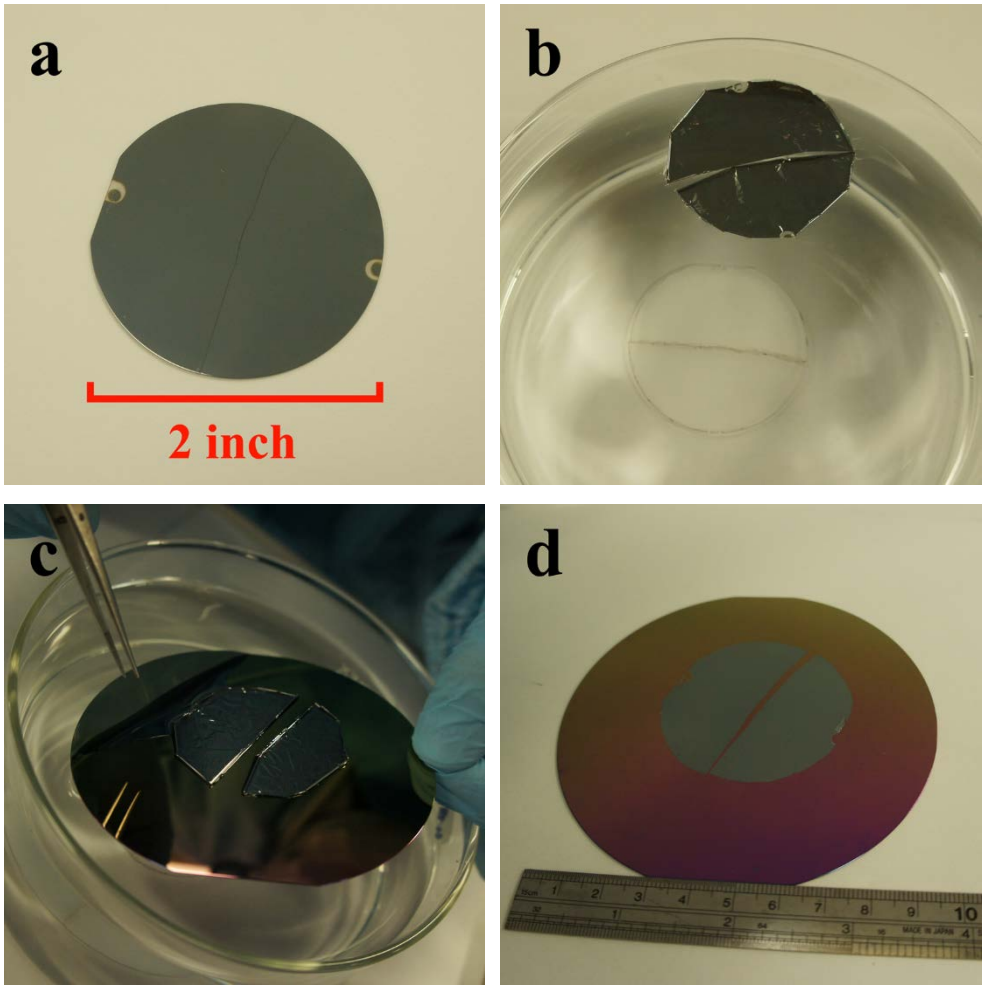

Figure 6.2 (a) The as-grown WS_2 film on a 2 inch sapphire wafer, (b) exfoliated polystyrene-coated WS_2 film floated on water, (c) pick up of the WS_2 thin film with a 4 inch SiO_2/Si wafer, and (d) the 2 inch WS_2 thin film transferred to the SiO_2/Si wafer without cracks or wrinkles.

Figure 6.3 shows the optical image of the WS_2 film transferred onto the SiO_2/Si wafer, which shows good integrity and no wrinkles or cracks. The whole wafer-scale WS_2 thin film can be completely transferred to the target substrate keeping high integrity utilizing this etching-free transfer technique. No remaining WS_2 material was detected on the substrate by the optical microscope and Raman microscope, even

though Raman microscopy is an extremely sensitive technique, which has the capacity to detect monolayers of a material. Thus, it is possible to reuse the sapphire substrates.

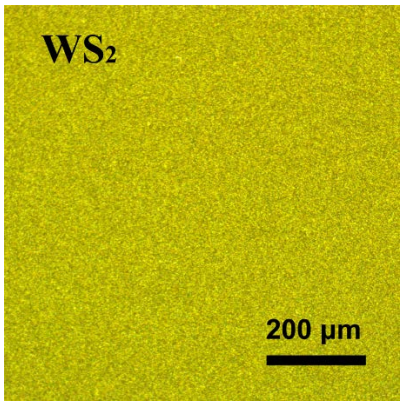

Figure 6.3 Optical image of the WS_2 thin film transferred to the SiO_2 substrate.

The XRD peak positions and peak intensities of the WS_2 film before transfer were almost the same as those of the WS_2 film after transfer to the target substrate. The FWHMs of the (002) peak of the WS_2 film before and after transfer were 0.191° and 0.189°, respectively. The Hall mobility of the type B WS_2 film was also maintained at 63.1 cm^2/Vs after transfer to another substrate. This is because the transfer process did not employ any kind of corrosive chemical etchant, which would damage the WS_2 thin film. The WS_2 thin film grown on the reused sapphire substrate had the same quality as that grown on the fresh sapphire substrate, as confirmed by the FWHM of the (002) peak in the HXRD spectrum of 0.189°, and its Hall mobility was as high as 62.1 cm^2/Vs, which is in the same level as the WS_2 film grown on the

fresh sapphire substrate, which showed a carrier mobility of 63.3 cm^2/Vs.

The exfoliation speed depends on the thickness of the spin-coated polystyrene layer, which can be effectively controlled by adjusting the polystyrene concentration and the spin-coating speed. By controlling the thickness of the polystyrene layer, the exfoliation time of a 2 inch wafer-scale film was only a few minutes. Figure 6.4 illustrates the etching-free transfer process of a WS_2 thin film onto a GaN substrate. It should be emphasized that only type B WS_2 films can be completely separated from the substrate in wafer scale. The presence of type-I textured crystallites in type A WS_2 films impedes water molecules to penetrate into the interface between the film and the substrate. In the typical wet chemical etching transfer approach, the chemical etchants, typically HF or KOH, will corrode or contaminate the surface of the film to cause critical problems in the resultant electronic devices. Nevertheless, the WS_2 thin film showed good stability in water during the etching-free transfer process and avoided the destructive exfoliation of the WS_2 film on the sapphire substrate.

The stronger adhesive force of the polystyrene layer on the WS_2 film compared with the force between the WS_2 film and the substrate is another key factor in the exfoliation process. If the adhesive force is weak, the WS_2 thin film cannot be wholly separated by water introduced between the WS_2 film and the substrate, which causes crack in the film during the exfoliation process. An adequate adhesive force can be attained through careful optimization of the baking time of the polystyrene layer.

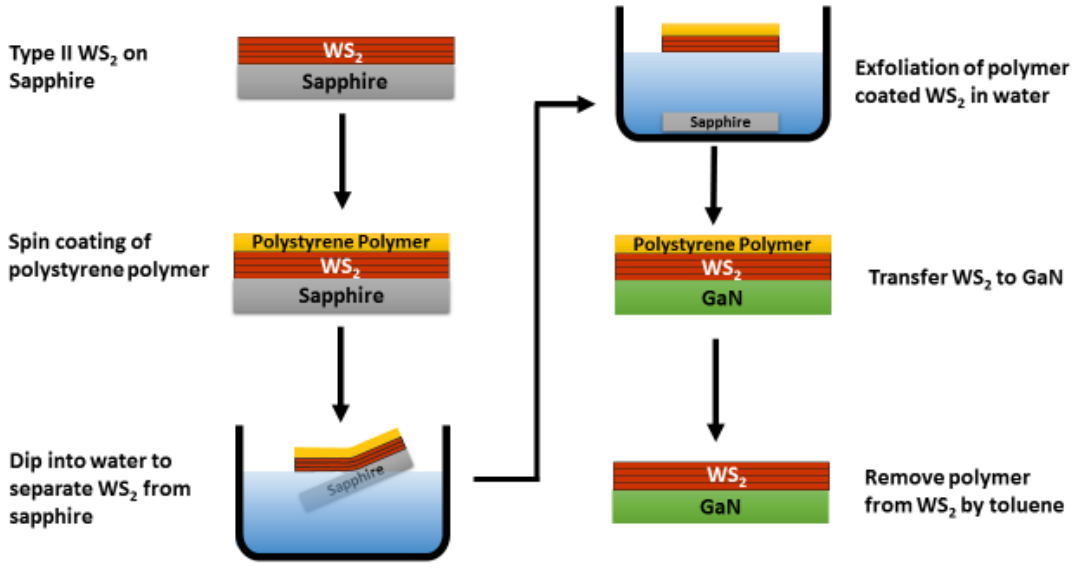

Figure 6.4 Schematic drawing of the etching-free transfer process of type-II WS_2.

The hydrophobicity of the carrier polymer is a significant factor to achieve exfoliation with no cracks or wrinkles. The separated polymer-coated WS_2 thin film was soft and very susceptible to breakage or folding. Every fold will produce a wrinkle after transfer. The high hydrophobicity of the polymer repels water droplets from the polymer surface, which enables the film to float on the water surface after exfoliated from the substrate. This also permits the film to automatically straighten out on the water surface to efficiently avoid the generation of wrinkles during the transfer process. Polystyrene has outstanding hydrophobic properties, more than Poly(methyl methacrylate) (PMMA), effectively flattening out the WS_2 film on the water. PMMA was also employed as a carrier polymer in our experiment, but transfer to the target substrate with PMMA resulted in wrinkles in the WS_2 film.

Besides the selection of an appropriate carrier polymer, the success of wafer-scale transfer also strongly relies on the film microstructure. As discussed in Chapter 5, type A films consist of a mixture of type-I and type-II crystallites. In contrast, the type B film displayed uniformity with large layered crystals parallel to the substrate, wherein wafer-scale WS_2 thin films can be uniformly separated from the as-grown substrate and transferred to other flat substrates. As the crystal planes of the layered WS_2 thin film are parallel to the substrate, water molecules can uniformly penetrate into the interface between the film and the substrate, leading to the homogeneous exfoliation of the WS_2 thin film from the substrate. Nevertheless, it is not easy to completely separate the type A film from the growth substrate. In general, the type A film was partly exfoliated from the substrate with a significant concentration of cracks. This is because the presence of type-I crystallites leads to strong interaction forces between the dangling bonds of the type-I crystallites and the substrate surface, which hinder water molecules from homogeneously penetrating into the interface between the film and the substrate. Thus, only type B films can be perfectly transferred to n-type GaN substrates for p-n junction fabrication.

6.3.2 WS_2/GaN p-n Junctions Fabricated by the Transfer Method

To demonstrate the practicablity of the transfer process to fabricate high-performance devices, p-type WS_2 thin films (type B film), with both the back surface

(the growth interface) and the top surface, were transferred onto n-type GaN substrates to fabricate p-n junctions. These two types of p-n junctions are referred to as back-transferred p-n junction and top-transferred p-n junction, respectively. For further study of the transferred p-n junctions, a third type of p-n junction was also fabricated by directly growth of the WS_2 thin film on n-type GaN (type C film). Figure 6.5 shows the *I-V* curves of the back-transferred and top-transferred p-n junctions, which showed leakage current densities of 1.15 mA/cm^2 and 29.6 $\mu A/cm^2$ at -1 V, respectively, indicating the good adhesion of the transferred WS_2 film on the GaN substrate. In this study, the turn-on voltage is defined to be the value of the bias voltage when the current density reaches to 5 mA/cm^2, thus, the turn-on voltages of the two devices were 0.5 V and 1.2 V respectively. However, the p-n junction fabricated by the WS_2 film directly grown on the GaN substrate has a large leakage current density of 92.4 mA/cm^2 at -1 V. In addition, the reproducibility of the transferred p-n junctions can be well controlled, and the turn-on voltage and leakage current of the p-n junctions fabricated by our transfer method has a good repeatability. Table 6.1 gives the turn-on voltages and leakage current of the three different types of p-n junctions.

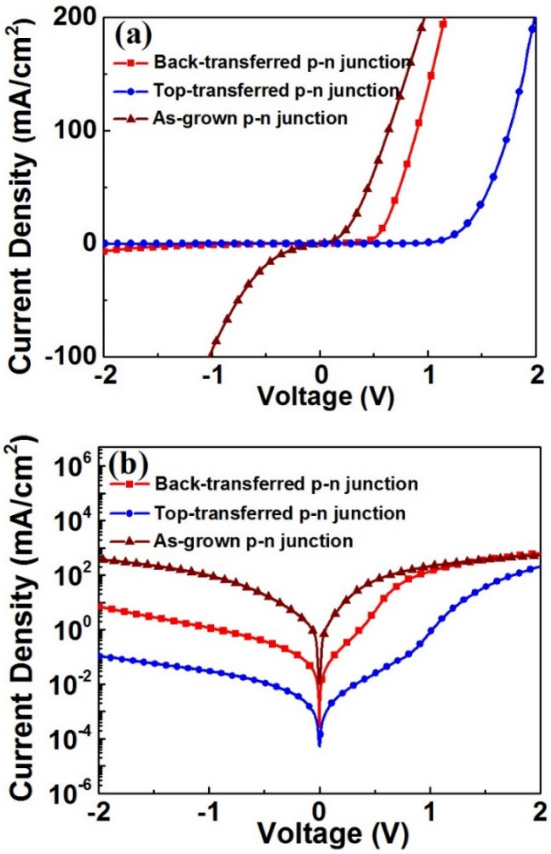

Figure 6.5 (a) I-V curves of the p-type WS_2 film on an n-type GaN p-n junction for the top-transferred p-n junction (blue solid circles), back-transferred p-n junction (red squares), and direct growth WS_2/GaN p-n junction (brown triangles). (b) I-V curves plotted on a semi-log scale.

The transferred devices show considerably lower leakage current than the as-grown WS_2/GaN p-n junction. This is due to the better crystal quality of the WS_2 thin films grown on sapphire substrates in comparison with the WS_2 thin films grown on GaN substrates, as proved by the SEM and XRD results in Chapter 5. The defect density of the WS_2 film grown on GaN is thought to be much higher than that of the WS_2 film grown on sapphire, which led to considerable degradation of the device performance. It should be noted that the leakage current of the top-transferred p-n

junction was almost two orders of magnitude lower than the back-transferred p-n junction. This is because the crystallinity of the top surface of the WS_2 film is better than that of the back surface.

Table 6.1 The leakage current density and turn-on voltage of the back-transferred, top-transferred and as-grown p-n junctions.

Back-transferred p-n junction	**Leakage current [mA/cm^2]**	**Turn-on voltage [V]**
1	***1.15***	***0.50***
2	***2.88***	***0.45***
3	***3.75***	***0.51***
Top-transferred p-n junction	**Leakage current [mA/cm^2]**	**Turn-on voltage [V]**
1	***0.0296***	***1.20***
2	***0.0971***	***1.07***
3	***0.0187***	***1.22***
As-grown p-n junction	**Leakage current [mA/cm^2]**	**Turn-on voltage [V]**
1	***92.4***	***0.17***
2	***80.6***	***0.16***
3	***73.8***	***0.17***

During the initial stage of the deposition process, large amount of step defects and dislocation defects are accumulated due to stacking faults of the islands and lattice mismatch between the film and the substrate.[226-228] The comparatively larger leakage current of the back-transferred device is due to the higher defect

concentration on the growth interface. The different turn-on voltages of the two transferred devices can be interpreted by the different surface energy level of the WS_2 films, which is characterized by XPS analysis in a subsequent section.

The forward resistances of the back-transferred and top-transferred p-n junctions were 118.8 Ω and 314.0 Ω at 2 V, respectively. The forward resistance of the directly grown device was 101.8 Ω which is smaller the transferred devices, this is because the compact small crystal pieces of the WS_2 grown on GaN can increase both the leakage current and the forward current. The reverse resistances of the back-transferred and top-transferred p-n junctions were 9.0×10^3 Ω and 5.99×10^5 Ω at -2 V, respectively. The reverse resistance of the top-transferred p-n junction was approximately two orders of magnitude higher than the back-transferred p-n junction, this is consistent with the analysis of lower leakage current of the top-transferred p-n junction. However, the reverse resistance of the directly grown device was only 173 Ω corresponding with the large leakage current of the device. The ideality factors of these three diodes can be calculated based on the linear region of the I-V curves on Figure 6.5. The ideality factors of the back-transferred and top-transferred p-n junctions were 2.92 and 3.57, respectively. For typical p-n junctions, ideality factors are commonly between 1 and 2. However, the ideality factors of some heterojunctions can be greater than 2 due to large series resistances or high recombination at the interface of the heterojunction.[229] As mentioned above, the forward resistance of the top-transferred p-n junction was larger than the back-transferred device. The

larger resistance contributed to the higher ideality factor of the top-transferred device. The ideality factor of the directly grown p-n junction was 4.17 which is much higher than the transferred devices. The high recombination at the interface of the heterojunction due to the higher defect density of the WS_2 thin film directly grown on GaN should be the reason of the higher ideality factor value of the directly grown p-n junction.

The C-V measurement results are consistent with the *I-V* measurement results. The C-V curves of the three different types of p-n junctions are shown in Figure 6.6. The capacitance of a p-n junction commonly contains two main components: 1) the space charge capacitance originating from the accumulation of charge in the depletion region, which is the dominant capacitance at reverse bias, and 2) the diffusion capacitance originating from surplus carriers, which is the dominant capacitance at forward bias because of the large diffusion current.[230] With an increase of the reverse bias, the capacitance of the p-n junction is decreased, because the reverse bias broadens the depletion region, leading to a reduction in the capacitance. The lower capacitance of the top-transferred p-n junction at reverse bias in comparison with the back-transferred p-n junction is consistent with its lower leakage current. The capacitance of the as-grown p-n junction increased when the reverse bias was below -0.5 V. In the case that the voltage bias was above -0.5 V, the space charge capacitance is the dominate capacitance, which decreased with the voltage bias. At a voltage below -0.5 V, the capacitance increased with reverse bias,

indicating that diffusion capacitance was the dominate capacitance because of the large leakage current due to interface defects. The results show that the high concentration of defects in the as-grown p-n junction is the main cause of the larger leakage current compared with that of transferred p-n junctions.

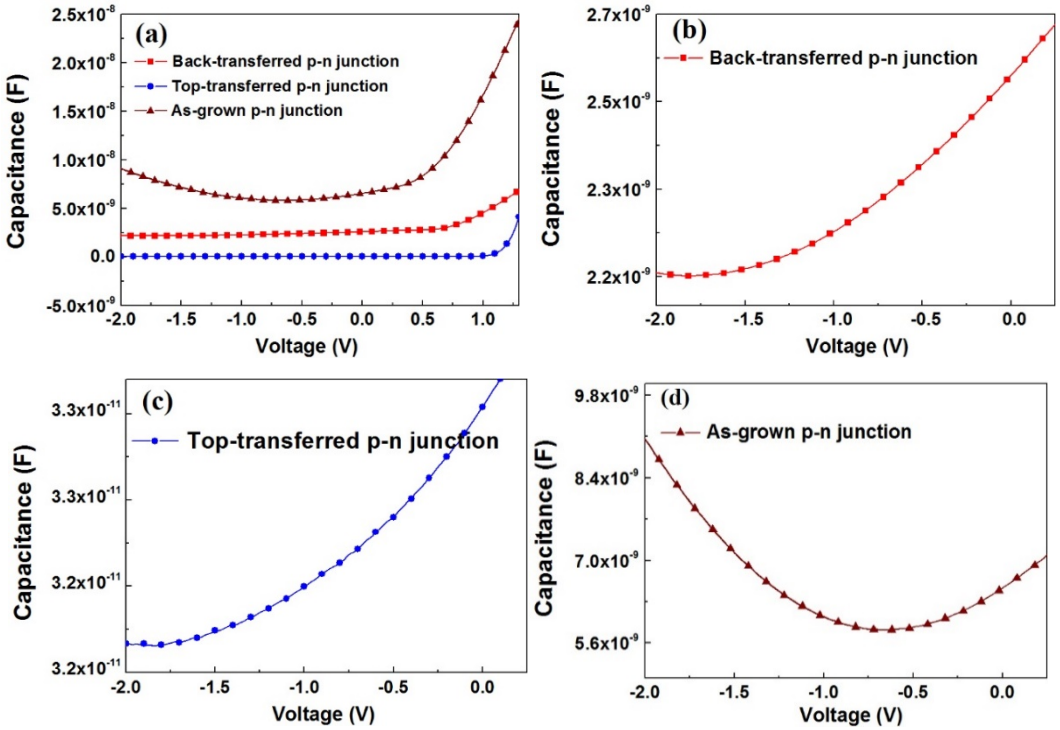

Figure 6.6 C-V curves of three types of WS_2/GaN p-n junctions: (a) back-transferred p-n junction (red squares), top-transferred p-n junction (blue solid circles) and as-grown p-n junction (brown triangles). (b), (c), (d) Magnified view of the three C-V curves.

6.3.3 Band Diagrams of the WS_2/GaN p-n Junctions

The XPS spectra, showing the valence band maximum (VBM) of the top surface and back surface (the growth interface) of the type B WS_2 film, type C WS_2 film and n-type GaN film, are shown in Figure 6.7. The C 1s peak (284.6 eV) was used to calibrate the XPS spectra to offset surface charge effects. The position of the VBM

relative to the Fermi level was determined by the intersection of the linear fit to the leading edge of the photoemission and the background. The bandgap of WS_2 and GaN are approximately 1.4 eV and 3.4 eV at room temperature.[22, 231] Figure 7.8 shows the band diagrams of three films based on the values measured by XPS. The VBM of the top surface and back surface of the type B film are 0.27 eV to 0.86 eV, respectively, and the film surface was altered from p-type to weak n-type conduction. As previously discussed, the growth interface of the WS_2 thin film usually contains more defects than the top surface. As a result, monolayer or few layer WS_2 grown on sapphire is commonly n-type because of the presence of S-vacancies, which are n-type defects.[227, 228, 232] The n-type band diagram of the growth interface of our 400 nm type B WS_2 film was also confirmed by XPS. The slight change in the valence band offset at the interface of the transferred WS_2 film on GaN can be neglected, since the interface interaction is dominated by weak van der Waals forces, the surface energy of WS_2 and GaN is thought to be maintained at the original level. The ΔE_V of the top-transferred p-n junction is 1.88 eV, which is nearly 50% larger than the ΔE_V of the back-transferred p-n junction of 1.29 eV. The larger ΔE_V value results in a greater built-in voltage, which is consistent with the higher turn-on voltage of the top-transferred p-n junction. The ΔE_V values of the back-transferred and top-transferred p-n junctions are 1.29 eV and 1.88 eV, respectively, which are in accordance with the change of the turn-on voltage from 0.5 V to 1.2 V. The larger ΔE_V also has the effect of reducing the leakage current. The VBM of the top surface

of the type C WS_2 film is slightly higher than that of the top surface of the type B WS_2 film, which results from the higher concentration of surface defects due to the poor crystal quality of WS_2 induced by the instability of the GaN substrates at 1000 °C during growth.

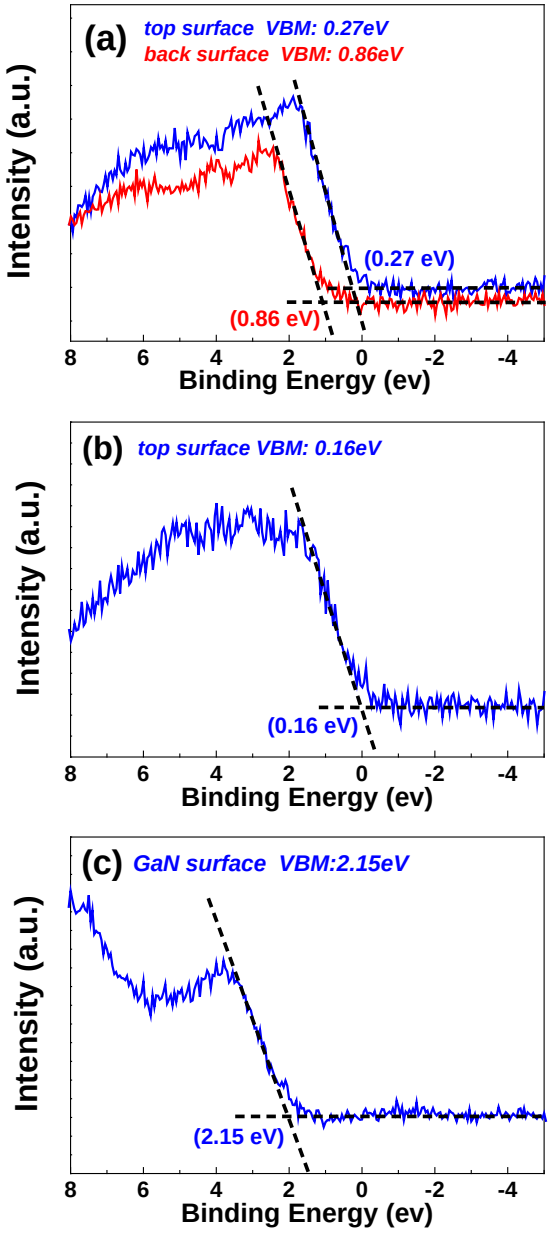

Figure 6.7 Valence band XPS spectra of (a) the top surface and back surface (growth interface) of WS_2 grown on sapphire (type B film), (b) the top surface of WS_2 grown on GaN (type C film), and (c) the GaN film.

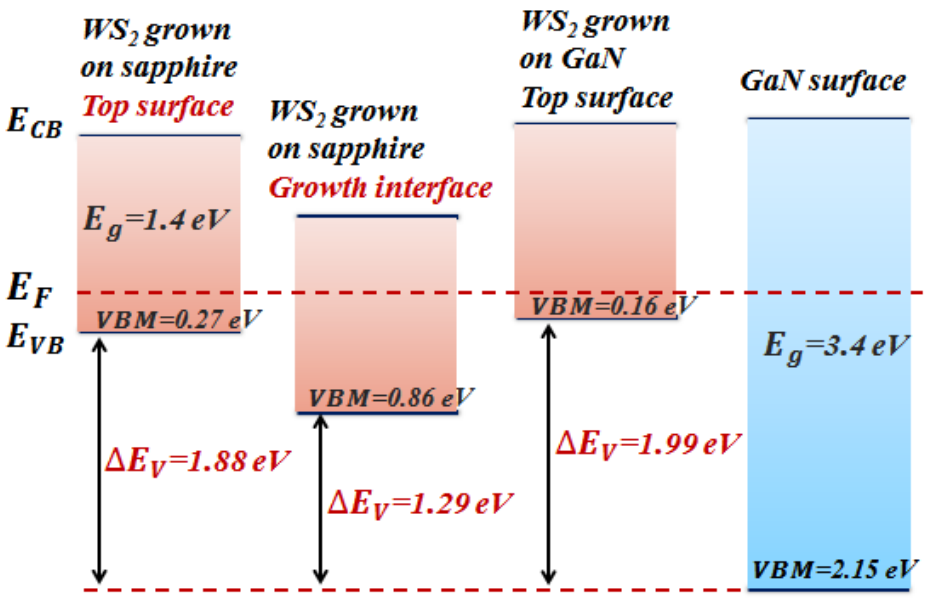

Figure 6.8 Band diagrams of the different WS_2 and GaN film surfaces.

At the interface of WS_2 and n-GaN, due to the Fermi level difference, some of the electrons in the GaN layer will be injected into WS_2, shifting the Fermi level of two materials in the same position. Neglecting the slight change of the conduction band offset at the interface of the transferred WS_2 film on GaN due to the weak van der Waals forces, the surface energy of the WS_2 and GaN is thought to be maintained at the original level. According to Figure 6.8, ΔE_C of the top-transferred and the back-transferred p-n junctions are 0.12 eV and 0.71 eV, and ΔE_C of the directly grown p-n junction is 0.01 eV. When a forward bias is applied to the device, majority electrons in the n-type GaN diffused into the p-type WS_2. The larger ΔE_C would benefit the electron transportation to increase the diffusion current. This is consistent

with the higher current density of the back-transferred device than the top-transferred device at forward bias, as shown in Figure 6.5. When the device was at reverse bias, a barrier was generated to block the electrons to diffuse from n-type GaN to p-type WS_2. The smaller ΔE_C would result in a higher barrier to block the electron transport to decrease the leakage current. This is consistent with the lower leakage current of the top-transferred device than the back-transferred device at reverse bias. The WS_2 directly grown on GaN had a high defect density due to the lower crystallinity. The large defect density will result in the large leakage current of the p-n junction, as the large number of defects at the interface provide a channel for the electron transport across the barrier, especially for the directly grown WS_2/GaN heterojunction. In layered materials, current transport exists in both vertical and lateral directions and the carrier mobility in the lateral direction is typically much higher than the vertical direction.[211] At the interface of the 2D/3D heterojunction, significant lateral carrier transport will result in a high probability of the carriers being captured by defects at the grain boundary. Thus, the directly-gown WS_2/GaN p-n junction showed a much larger leakage current than the transferred devices.

6.4 Summary

Employing the etching-free transfer method, wafer-scale WS_2 thin films were separated and transferred onto arbitrary, smooth substrates with no noticeable

wrinkles or cracks. The etching-free transfer approach utilizes the different surface properties of the WS_2 film and the sapphire substrate and does not use any corrosive chemical etchants. Consequently, the transferred film maintained the superior integrity of the WS_2 film, which allows the fabrication of good quality p-n junctions and for the substrates to be recycled. The carrier polymer and the microstructure of the film are two key factors for the successful wafer-scale transfer of WS_2 thin films. The WS_2/GaN p-n junctions fabricated by our transfer method had a quite low leakage current density of 29.6 $\mu A/cm^2$ at -1 V, whereas the direct growth WS_2/GaN p-n junction had a large leakage current density of 92.4 mA/cm^2 at -1 V. This is due to the degradation of the GaN layer at the temperature of 1000 °C, which leads to the poor crystal quality of the WS_2 film. The leakage current density of the top-transferred p-n junction was much lower than that of the back-transferred p-n junction owing to the better crystal quality of the top surface of the WS_2 film. The VBM of the top surface and the back surface (the growth interface) of the WS_2 film deposited on sapphire with Ni texture promoter was altered from 0.27 eV to 0.86 eV, and the conduction type was altered from p-type to weak n-type. This etching-free exfoliation approach is expected to greatly expand the applications of WS_2 thin films for optoelectronic and electronic devices. In addition, this technique is also compatible with other layered materials, such as MoS_2, WSe_2, SnS_2, etc.

CHAPTER 7 FABRICATION OF WS_2 FIELD-EFFECT TRANSISTORS BY THE CHEMICAL ETCHING METHOD

The most widely studied 2D material is graphene due to its superior physical properties, such as high mechanical strength, high optical transmittance and high mobility.[16-18] However, graphene does not have a bandgap between its valence and conduction bands, which limits its application in semiconductor devices. [15, 19] Engineering a graphene bandgap by doping complicates the device fabrication process and reduces its mobility.[233] Two-dimensional semiconducting TMDCs, which have fewer dangling bonds, stable crystal structure and high mobility, are attractive for use as the channel layer in thin-film FETs. An ultra-thin channel layer in an FET allows lower power consumption than classical transistors.[234] In this study, uniform large-area ultra-thin WS_2 thin films, down to 40 nm, were obtained by a chemical etching method to fabricate ultra-thin FETs. To passivate the defects generated during the etching process, the acid-etched WS_2 thin film was annealed under S atmosphere to recover its original quality, and the defect density was studied by noise measurements. The device performance of the ultra-thin WS_2-based FET can be further improved by surface passivation by depositing a 2 nm Al_2O_3 layer on the surface of the WS_2 film.

7.1 Experimental Details

7.1.1 Chemical Etching of the WS_2 Thin Films

The WS_2 thin films used to fabricate ultra-thin FETs were prepared by the CVD method, as described in Chapter 5. The original thickness of the WS_2 thin films was approximately 400 nm. To fabricate the FETs, the WS_2 films were etched down to 40 nm by a mixed chemical etchant of 7.5% H_2CrO_4 and 3.8% HF. Employing the chemical etching method, uniform large-area 40 nm ultra-thin WS_2 thin films can be obtained for fabricating ultra-thin FETs. The fabrication of WS_2-based FETs was based on the transfer method described in Chapter 6. The 40 nm WS_2 thin film is quite fragile and delicate, thus, during the etching and transfer process, the WS_2 thin film was supported by a polystyrene film. The etching and transfer process of the WS_2 thin film is shown in Figure 7.1. First, the WS_2 thin film was immersed in a chemical solution of 7.5% H_2CrO_4 and 3.8% HF in order to smooth the film surface. After 15 minutes, the film was picked up and washed with deionized water. Then, a polystyrene solution was spin-coated on the WS_2 film at a speed of 4000 rpm. Then, the sample was baked at a temperature of 80 °C for 10 minutes to evaporate the solvent of the polymer. The polymer surface was cut along the edge using a sharp blade to allow water to penetrate into the interface between the film and the substrate. Then, the sample was immersed in deionized water for a few minutes to separate the polymer-coated WS_2 film from the sapphire substrate. The polymer-coated WS_2 thin

film was transferred to a chemical solution of 7.5% H_2CrO_4 and 3.8% HF. The film floated on the surface of the chemical solution, and the WS_2 film uniformly contacted the chemical solution. It normally takes ~ 45 minutes to etch the WS_2 film from 400 nm to 40 nm, and the etching rate is ~8 nm/min. The final thickness of the etched WS_2 was 40 nm, as measured by surface profiler. The acid-etched polymer-coated WS_2 film was then transferred to deionized water to wash away the chemical solution and picked up by the target substrate, followed by soft baking at 70 ℃ for 15 minutes to remove the water residue and hard baking at 130 ℃ for 15 minutes to achieve good adhesion. Finally, the polystyrene was dissolved in toluene for 30 minutes and washed sequentially with acetone, IPA and deionized water.

7.1.2 Fabrication of WS_2 Field-Effect Transistors

The fabrication of WS_2 thin-film FETs was based on the transfer method described in Chapter 6. To passivate the defects generated during the etching process, the acid-etched WS_2 thin film was annealed under S atmosphere to recover its electronic properties. After annealing, the film was transferred to a heavily doped Si substrate covered with a 300 nm SiO_2 layer. Electrical contacts were fabricated by depositing 5 nm Ni and 100 nm Au layers as electrodes. For further passivation of the surface defects of the WS_2 thin film, a 2 nm Al_2O_3 layer was deposited on the surface of the WS_2 film by atomic layer deposition (ALD).

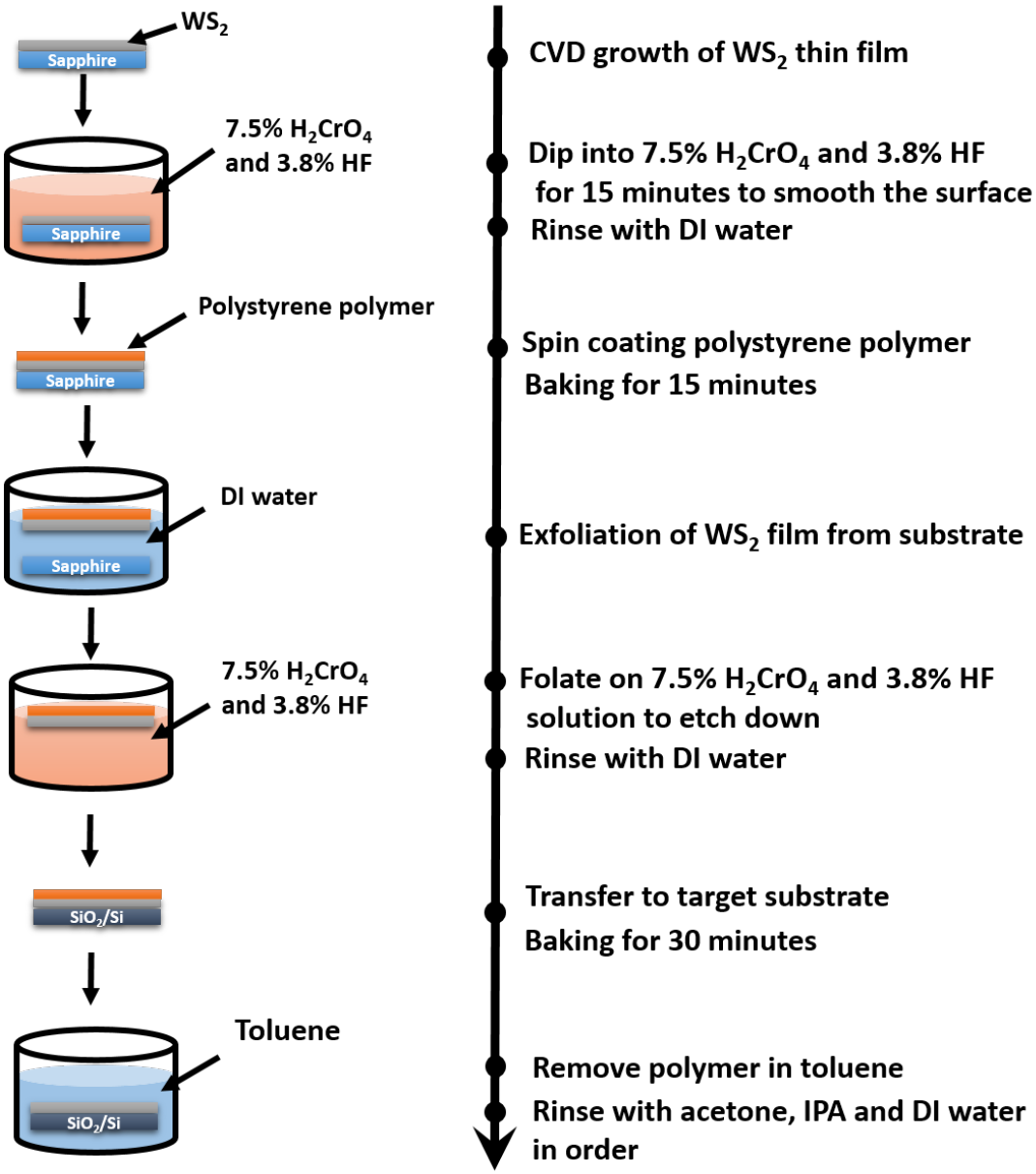

Figure 7.1 Schematic illustration of the etching and transfer process of the WS_2 thin films.

The construction of the WS2-based FETs is illustrated in Figure 7.2. For systematic study of the WS2 thin-film FETs, three types of WS2 thin films were used to fabricate FETs: 1) WS2 thin films etched by chemical etchant, 2) acid-etched and

re-annealed WS2 thin films, and 3) acid-etched and re-annealed WS2 thin films with a 2 nm Al2O3 layer on the film surface. All WS2 thin films used for the fabrication of FETs were p-type materials.

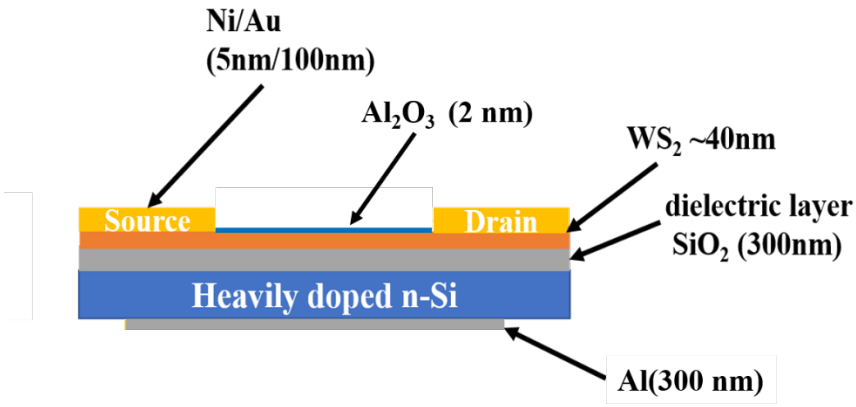

Figure 7.2 Illustration of the construction of the WS_2-based FET.

7.2 Sample Characterizations

The surface morphologies of the WS_2 thin films were characterized by SEM. A JEOL 6490 microscope was employed to obtain SEM images to investigate the microstructures of the WS_2 thin films, with an electron accelerating voltage of 30 kV. The phonon behaviors were investigated using a backscattering Raman microscope, and the excitation wavelength of the laser was 488 nm. XPS measurements were performed on a SKL-12 spectrometer with an Al K_α X-ray source. The XPS spectra were calibrated by the C 1s peak (284.6 eV) to determine the VBM relative to the Fermi level. The electrical characterizations of our devices were performed at room

temperature using an Agilent B1500A semiconductor device parameter analyzer and shielded probe station with voltage sources. Noise analysis was performed with a noise measuring system consisting of a current amplifier and a dynamic signal analyzer. The noise power spectral density was recorded by a HP3561A dynamic signal analyzer, and the current fluctuations were amplified by a Stanford Research SR570 amplifier. All noise measurements were performed in a shielded room to eliminate external interferences.

7.3 Results and Discussion

7.3.1 Etching Down of WS_2 Thin Films

For chemical etching, 400 nm thick WS_2 thin films with type-II layered crystals grown by CVD method were selected. A mixed solution of H_2CrO_4 and HF is thought be an effective chemical etchant to etch WS_2 crystals.[235] The etching rate was dependent on the temperature and the concentration of the etchant. The SEM images of the WS_2 thin films at different etching times, including 10 minutes, 20 minutes, 30 minutes, and 40 minutes, are shown in Figure 7.3.

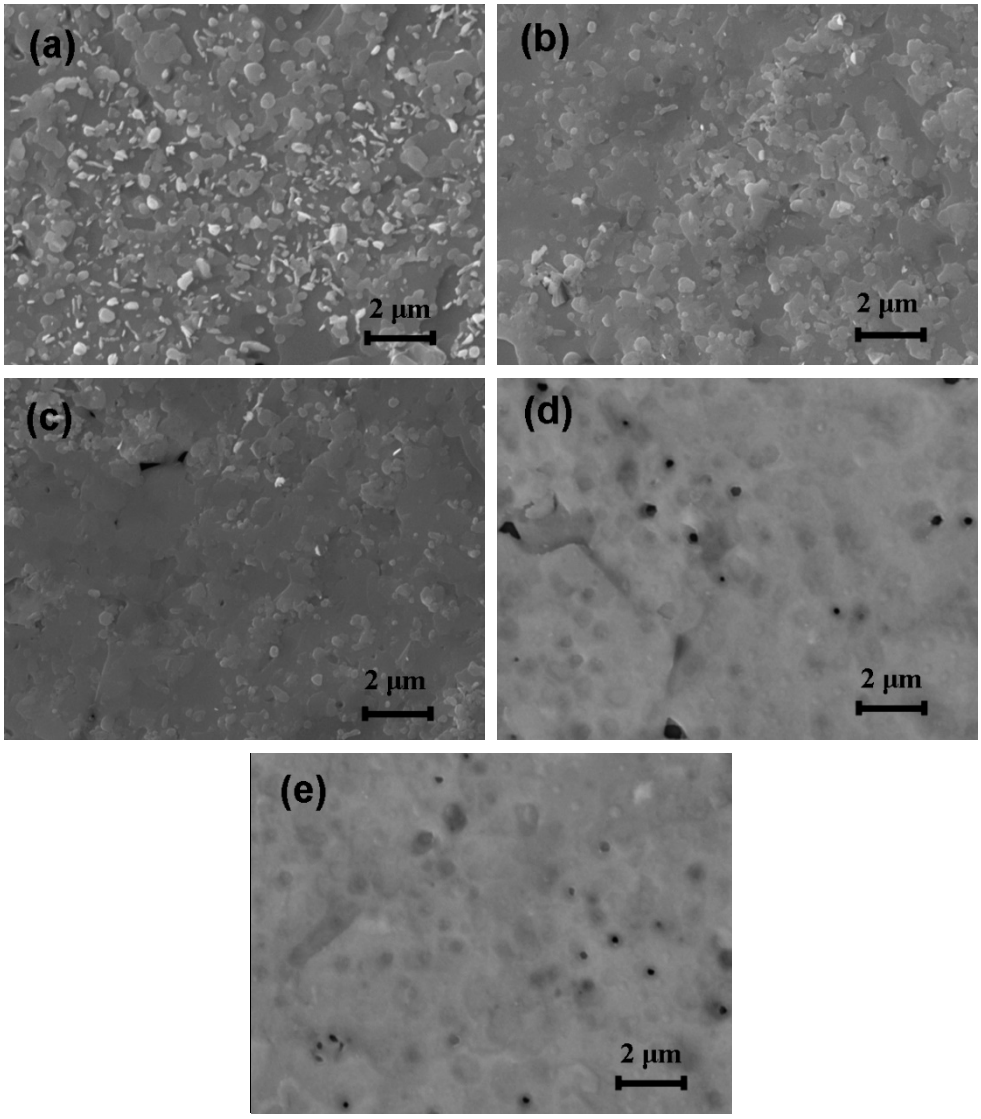

Figure 7.3 SEM images of the WS_2 thin films at different etching times: (a) without etching, (b) 10 minutes of etching, (c) 20 minutes of etching, (d) 30 minutes of etching, and (e) 40 minutes of etching.

For the layered structure WS_2 crystals, the etching rates are different for different crystal orientations, and the lateral etching rate of the layered crystal is typically faster than vertical etching rate.[235] As seen in the SEM images of the original and acid-etched WS_2 film surface, many small crystallites were observed on the film surface

at the initial stage. With an increase in the etching time, the small crystallites reduced and then disappeared, which indirectly confirmed the anisotropic etching of WS_2 crystals by H_2CrO_4 and HF acid. The 40 minute acid-etched WS_2 thin film was uniform with a thickness of approximately 40 nm. After 30 minutes of etching, some pinholes appeared on the film surface, but the density of pinholes is in an acceptable range for the fabrication of transistors.

7.3.2 Electronic Properties of the Acid-Etched WS_2 Thin Films

Figure 7.4 shows the I-V curves of the original, acid-etched and re-annealed WS_2 thin films measured by a parameter analyzer with a shielded probe station, in which the distance between the two contacts was 1 cm. The ohmic contacts were formed on the original and re-annealed WS_2 thin films during the measurement. However, there was a small barrier in the I-V curve of acid-etched WS_2 thin film indicating the change of electronic properties after etching process. To exclude the effect of contact resistance, the resistivity of the original, acid-etched and re-annealed WS_2 thin films were measured by four point resistivity measurement. The measured resistivity of these three kinds of WS_2 thin films are listed in table 7.1.

Table 7.1 Resistivity of the original, acid-etched and re-annealed WS_2 thin films.

Sample	Resistivity [Ω•cm]
Original WS_2 thin film	2.12
Acid-etched WS_2 thin film	6.20
Acid-etched and re-annealed WS_2 thin film	1.06

The resistivity of the original WS_2 thin film without etching was 2.12 Ω•cm, however, the resistivity of the acid-etched WS_2 thin film was remarkably increased to 6.20 Ω•cm. The substantially increased resistivity of the acid-etched WS_2 thin film was due to the large number of defects generated during the etching process. S-vacancies are the most common defects in WS_2 crystals due to the deficiency of S atoms during the reaction process. During the etching process, a significant number of S-vacancies were generated in the WS_2 films. S-vacancies are n-type defects and thus are anti-dopants for our p-type WS_2 thin films, resulting in a large increase of the film resistivity. However, by annealing the film under S atmosphere, the resistivity of the acid-etched film can be recovered to 1.06 Ω•cm, which is even lower than that of the original film of 2.12 Ω•cm. S-vacancies can be eliminated by annealing the film under S atmosphere. S vapor provides an S atom source to fill S-vacancies, leading to the recovery of the resistivity of the WS_2 film.

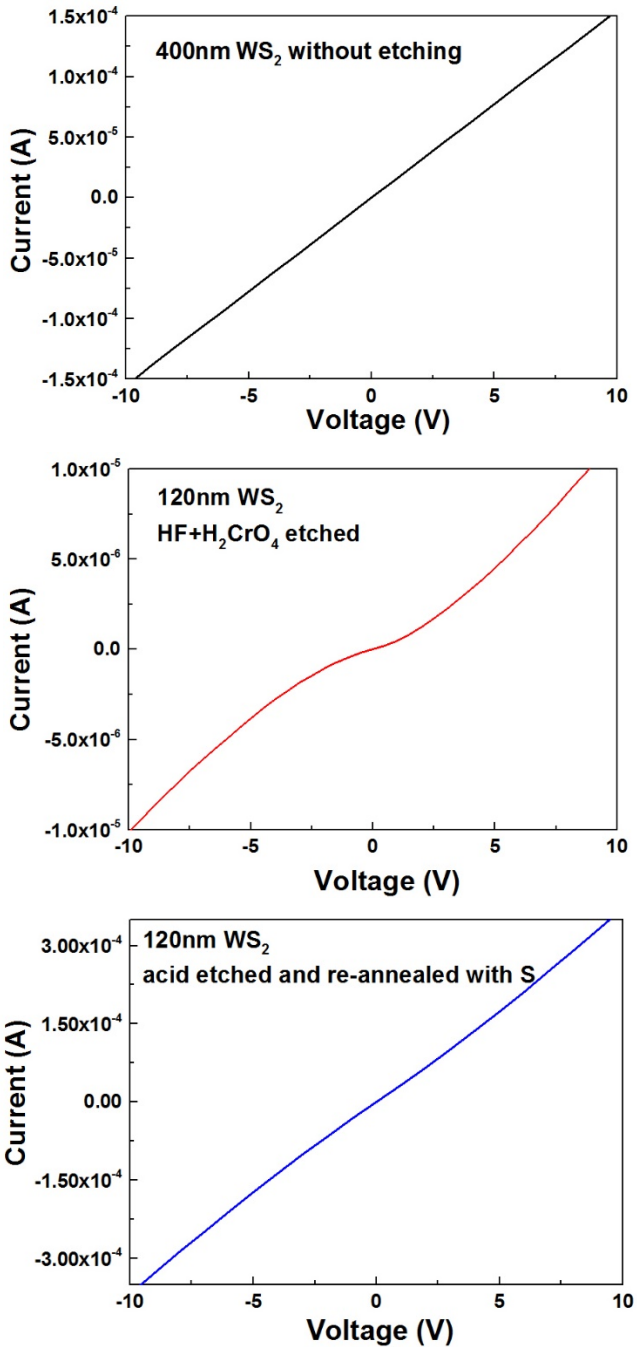

Figure 7.4 I-V curves of the (a) 400 nm original WS_2 thin film, (b) 120 nm acid-etched WS_2 thin film, and (c) 120 nm acid-etched and re-annealed WS_2 thin film, with the contact distance of 1 cm.

It is noted that, after annealing, the resistivity of the WS_2 film was even lower than that of the original film. This can be explained by the SEM images of the original and acid-etched WS_2 thin films in Figure 7.3, in which the small crystallites on the film surface contain a large density of defects at grain boundaries and dislocations, which will trap free carriers and degrade electron transport properties. During the etching process, the small pieces were removed from the film surface, and thus, after the S-vacancies were passivated by annealing, the resistivity was even lower than that of the original film. The change of the defect density after the etching process was confirmed by low-frequency noise measurement, as shown in Figure 7.7. The noise data indicates that, after chemical etching, the defect density was about one order of magnitude higher than that of the original film, which is in accordance with our analysis of the increased film resistivity resulted from the increased defect density after etching process. N-type S-vacancies are anti-dopants for our p-type WS_2 thin films leading to a large increase of the film resistivity. By annealing the acid-etched WS_2 film in S atmosphere, the defect states density was even lower than that of the original film by passivating defect states in the WS_2 thin film. Detailed discussion and interpretation on the noise data is given on the section of the low-frequency noise measurement.

The striking change in resistivity of the acid-etched WS_2 film can be explained by the change in the energy band diagram, as confirmed by the XPS result. The XPS spectra showing the VBM of the original and acid-etched WS_2 thin films are given in

Figure 7.5. The C 1s peak (284.6 eV) was employed for the calibration of the XPS spectra to offset surface charge effects. The position of the VBM relative to the Fermi level was determined by the intersection of the linear fit to the leading edge of the photoemission and the background. The bandgap of WS_2 is 1.4 eV at room temperature.[58] Figure 7.6 shows the band diagrams of the original, acid-etched and etched and re-annealed WS_2 thin films, based on the values measured by XPS. The VBMs of the original and acid-etched WS_2 thin films are 0.27 eV to 0.67 eV, respectively. As in the previous discussion, a great number of defects with a large proportion of S-vacancies were introduced into the WS_2 thin film during the etching process. N-type S-vacancies are anti-dopants for the p-type WS_2 thin films, and thus, the films were compensated from typical p-type to weak p-type, and the Fermi level was nearly in the middle of the bandgap. Therefore, the resistivity was similar to that of the intrinsic WS_2 material. After annealing under S atmosphere, S-vacancies were filled by S atoms, leading to the WS_2 thin film recovered to a typical p-type material with the VBM of 0.33 eV.

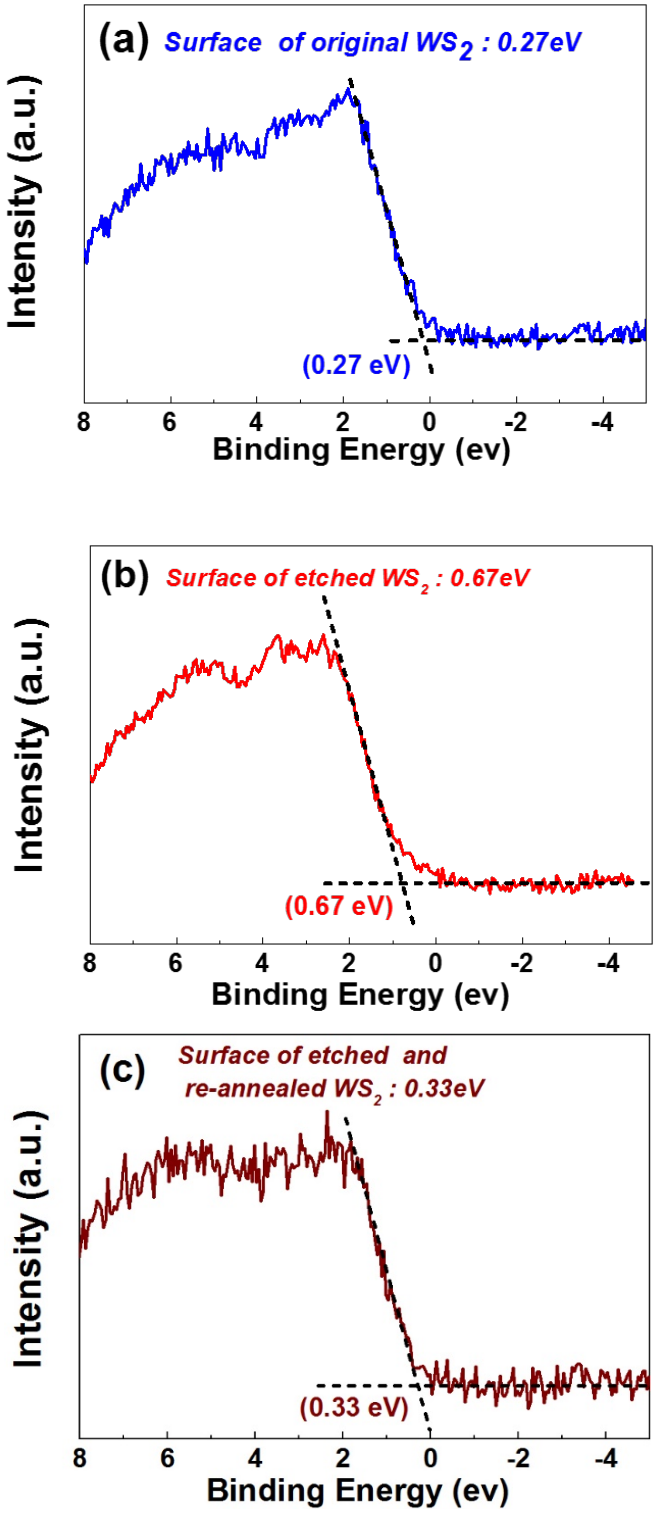

Figure 7.5 Valence band XPS spectra of the surface of (a) the initial 300 nm WS_2 thin film, (b) the acid-etched 120 nm WS_2 thin film and (C) etched and re-annealed 120 nm WS_2 thin film.

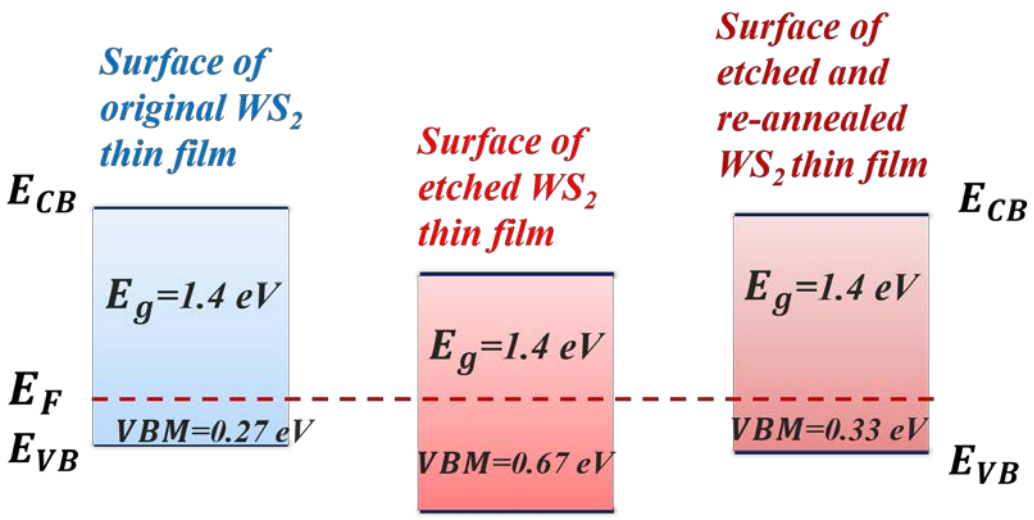

Figure 7.6 Band diagrams of the initial 400 nm, acid-etched 120 nm and etched and re-annealed 120 nm WS_2 thin films.

Defect densities of the WS_2 thin films were analyzed by measuring the low-frequency noise, which is a powerful technique for the characterization of defect states inside a material. The low-frequency noise in the device conductance originates from the random trapping and detrapping of the carriers by the localized defect states in the material. When a trap captures a carrier, its charge state will be modified resulting in the corresponding variation in the local band bending at the vicinity of the trap. This leads to a modulation in the local carrier density. Furthermore, the change in the charge state of the trap will also lead to a variation in the columbic scattering rate and thereby resulting in the fluctuation in the carrier mobility. Hence, the correlated fluctuations in both the carrier density and mobility lead to the fluctuation of the conductivity. For the resistive WS_2 thin film, the random trapping and detrapping of the carriers by the localized defect states result in the fluctuation of

the conductivity of the film, expressed as the fluctuation of the current at a fixed voltage. Using the thermal activation model introduced in Chapter 3, the current noise power spectral density can be expressed as:

$$S_I(f) = AI^2 \int_x \int_y \int_z \int_E N_T(E, x, y, z) \frac{\tau}{1 + 4\pi^2 f^2 \tau^2} dE dz dx dy \tag{7.1}$$

where I is the current applied to the device, $N_T(E)$ is the trap density and τ is the time constant, which can be written as:

$$\tau = \tau_0 \exp\left(\frac{E}{\kappa_B T}\right) \tag{7.2}$$

where E is the activation energy of the localized state, κ_B is Boltzmann constant, and T is the absolute temperature. The Lorentzian at an arbitrary frequency ω, is shown to peak sharply under the condition where $\omega\tau = 1$. In this case, the Lorentzian peaks are sharply at $E_p = -k_B T \ln(\tau_0 \omega)$. For a smooth trap distribution $N_T(E)$ around E_p, by the approximation of $N_T(E) \cong N_T(E_p)$, the trap distribution $N_T(E)$ at the energy E_p can be expressed in terms of $S_I(f)$:

$$N_T(E_p) \approx \frac{4Cf}{\kappa_B T} \frac{S_I(f)}{I^2} \tag{7.3}$$

where C is a proportionally constant, and it is important to note that the trap density is proportional to $S_I(f) / I^2$. Without considering the exact magnitude of the constant C, we are only interested in the relative changes in trap density of the WS_2 thin films by different treatment techniques. The current noise power spectral density $S_I(f)$ was measured with the applied voltage ranging from 1 V to 0.2 V for the three types of WS_2 thin films, as shown in Figure 7.4: (a) initial 400 nm WS_2 thin film, (b) acid-

etched 120 nm WS_2 thin film, and (c) etched and re-annealed 120 nm WS_2 thin film. A nearly proportional relation between $S_I(f)$ and $1/f^{\gamma}$ was observed, where $\gamma \approx 1$. Because the trap density is proportional to $S_I(f)/I^2$ as implied by Equation 7.3, for comparison of trap densities of all three types of WS_2 thin films, $S_I(f)/I^2$ versus frequency of these three types of WS_2 thin films with the applied voltage of 1V were plotted in Figure 7.4(d). The current noise signal of the acid-etched WS_2 film is about one order of magnitude higher than the original film before etching that implies the higher trap densities after the etching process, which is in accordance with our analysis of the increased film resistance, in which the corrosive effect of the chemical enchant commonly generates a large number of crystalline defects at the grain boundaries in the WS_2 material. The low-frequency noise data strongly suggest that reduction of the defect states density was achieved through the passivation of the localized states within the bulk and at the grain boundaries of the WS_2 material, by annealing the acid-etched WS_2 film under S atmosphere, which is even lower than that of the original film. Thus, the S-vacancies as the majority defects can be passivated by annealing under S atmosphere. Small crystallites on the surface of the original WS_2 thin film contain a large number of grain boundaries and dislocations, however, these small crystallites can be removed during the etching process, thus after chemical etching and re-annealing under S atmosphere for defects passivation, the noise level for the WS_2 thin film was reduced below than that of the original film.

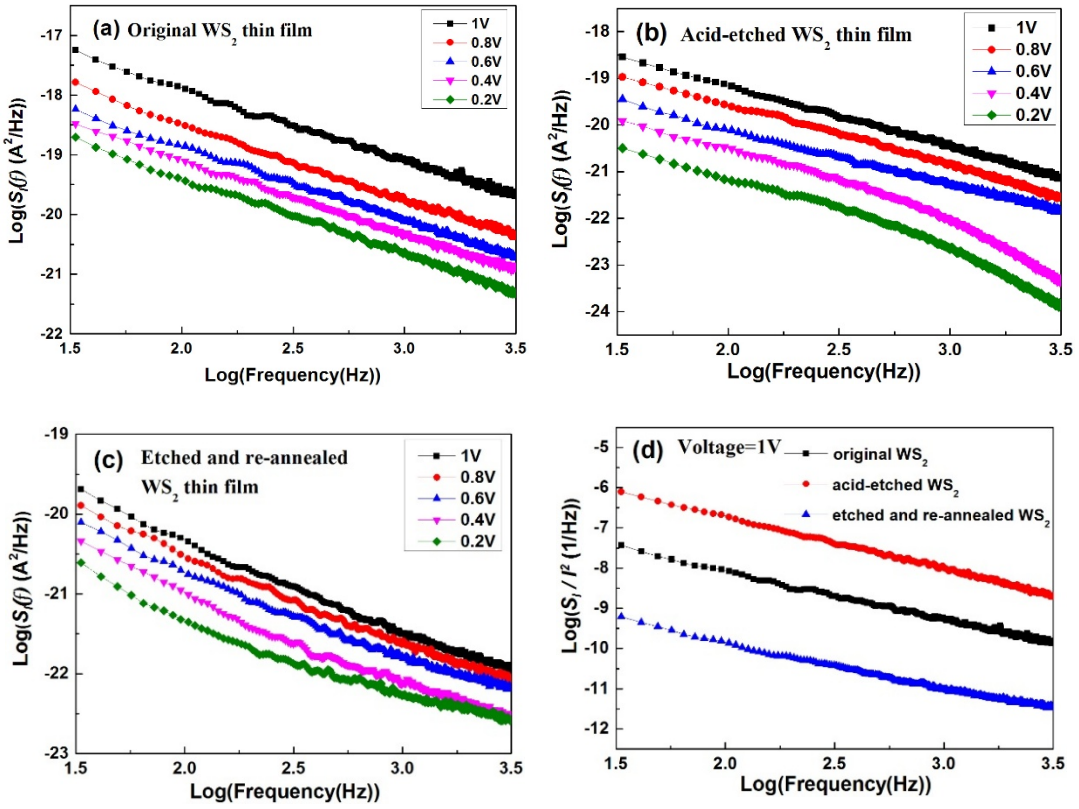

Figure 7.7 (a)(b)(c): S_I versus frequency on the log-log scale for three types of WS_2 thin films, with the applied voltage ranging from 1 V to 0.2 V: (a) initial 400 nm WS_2 thin film, (b) acid-etched 120 nm WS_2 thin film, and (c) etched and re-annealed 120 nm WS_2 thin film. (d) S_I/I^2 versus frequency for all three types of WS_2 thin films with the applied voltage of 1V.

7.3.3 WS_2 Based Field-Effect Transistors

For systematic study of the electronic properties of WS_2-based FETs, three types of WS_2 thin films were used as the channel layer to fabricate FETs: 1) acid-etched WS_2 thin films, 2) acid-etched and re-annealed WS_2 thin films, and 3) acid-etched and re-annealed WS_2 thin films with a 2 nm Al_2O_3 layer on the surface. All WS_2 thin films are p-type materials with a thickness of 40 nm. The FET fabricated with the acid-etched WS_2 thin film as the channel layer did not show any variation in the drain-

source current with an applied gate bias ranging from -100 V to 100 V. This is because the large number of defects generated during the etching process trap the carriers to counteract the carrier accumulation effect of the gate bias, and thus, the WS_2 channel always remains in the off state. To solve this problem, the acid-etched WS_2 thin film was annealed under S atmosphere, which effectively passivates the traps. Using the acid-etched and re-annealed WS_2 thin film as the channel layer, a working FET can be fabricated. The I-V characteristics of this FET, shown in Figure 7.8, indicate that it is a typical p-channel FET device. The linear relationship between the current and drain-source bias voltage indicates that the gold contacts are ohmic. The field-effect mobility is commonly expressed as:

$$\mu_{EF} = \frac{L}{WC_iV_i}\frac{dI_{ds}}{dV_{bg}} \tag{7.3}$$

where L is the channel length, W is the channel width, C_i is the capacitance per unit area between the channel layer and the back gate and V_i is the voltage drop across the channel. An approximation is commonly made in which the contact resistance is neglected, leading to V_i equaling V_{ds}. From the data in Figure 7.8, we can extract the field-effect mobility of $\mu_{EF} = 0.31\, cm^2V^{-1}s^{-1}$ according to:

$$L = 35\mu m, W = 300\mu m,\ V_{ds} = 2V,\ dI_{ds}/dV_{bg} = 6.18 \times 10^{-8},$$
$$C_i = \varepsilon_0\varepsilon_r/d,\ \varepsilon_0 = 8.85\times10^{-12}\ F/m,\ \varepsilon_r = 3.9,\ d = 300\,nm.$$

The on/off ratio of this transistor is 410.

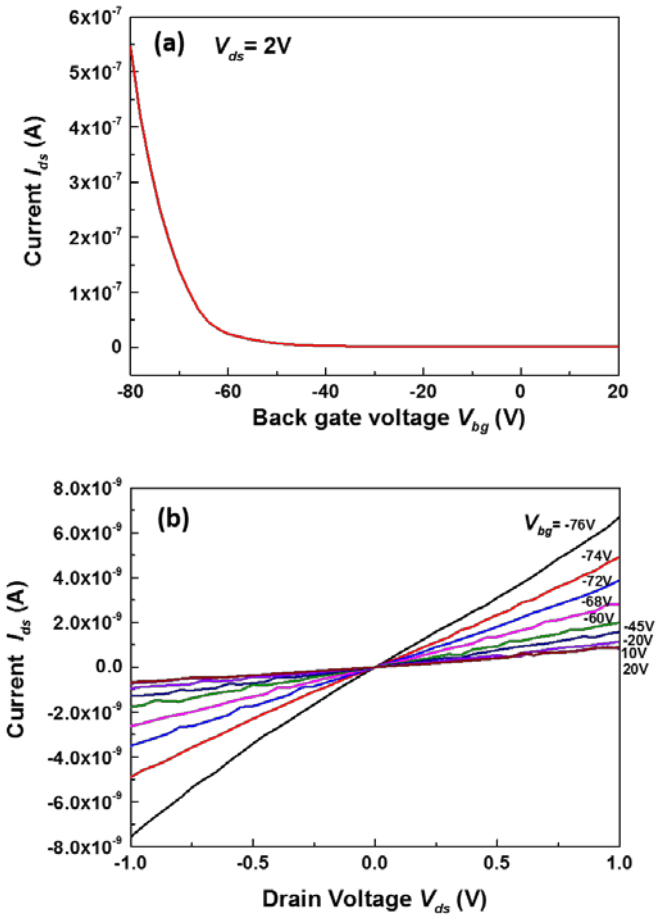

Figure 7.8 Characterization of the FET composed of the acid-etched and re-annealed WS_2 thin film as the channel layer: (a) I_{ds}-V_{bg} characteristics of the FET with a 2 V drain-source bias voltage and (b) I_{ds}-V_{ds} curves for different gate bias voltages.

To further improve the field-effect mobility and on/off ratio of the WS_2 thin film transistor, a 2 nm Al_2O_3 layer was deposited on the surface of the WS_2 channel layer by the ALD method to passivate the surface traps. The on/off ratio remarkably increased to 2700, which is an approximately 560% increase over that of the WS_2-based FET without an Al_2O_3 layer, as shown in Figure 7.9. Meanwhile, the field-effect mobility increased by approximately 70% to 0.54 $cm^2V^{-1}s^{-1}$. The improvement

in the device performance, especially in the on/off ratio, is attributed to the suppression of Coulomb scattering of the high-k (k is dielectric constant) environment of Al_2O_3 on the surface of the channel layer.[236, 237]

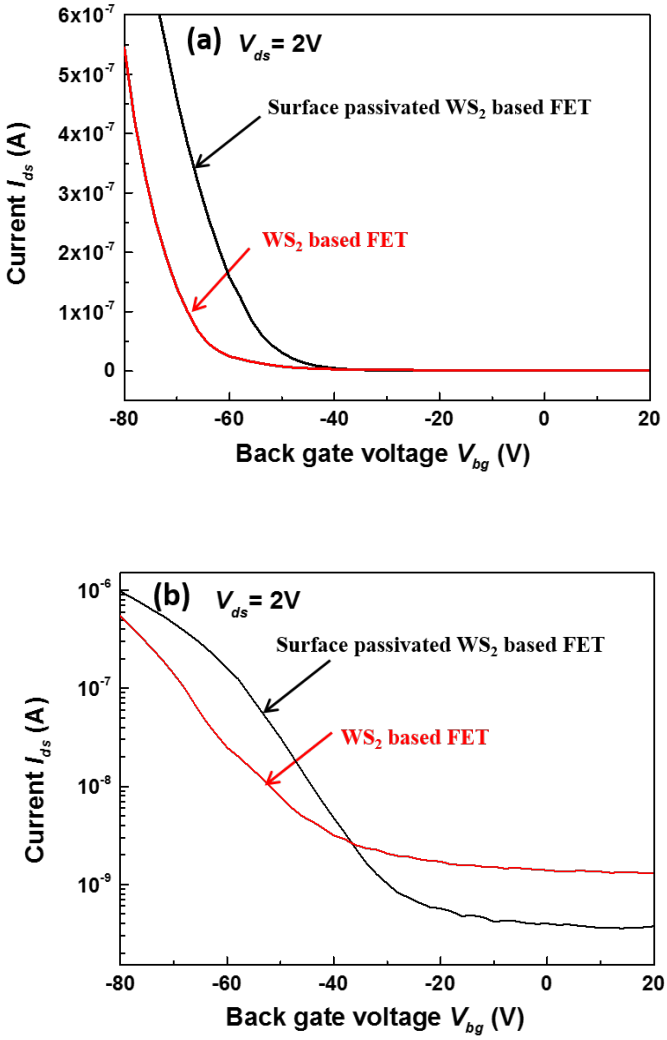

Figure 7.9 I_{ds}-V_{bg} curves of the FET containing the acid-etched and re-annealed WS_2 thin film as the channel layer (red line) and the surface-passivated FET with a 2 nm Al_2O_3 layer on the WS_2 film surface (black line) plotted in (a) linear scale and (b) log scale.

The exfoliated single layer MoS_2 from single crystals were used to fabricate the TMDC-based FET. The mobility of the FETs fabricated using the exfoliated single layer MoS_2 was commonly found to be around 200 $cm^2V^{-1}s^{-1}$,[238, 239] and the highest reported value reached 320 $cm^2V^{-1}s^{-1}$ with the on/off ratio of 10^7.[240] For the FETs fabricated using the exfoliated single layer WS_2, the typical mobility was around 50 $cm^2V^{-1}s^{-1}$,[241] and the highest mobility reached 214 $cm^2V^{-1}s^{-1}$ with the on/off ratio of 10^7.[242] The exfoliated single layer material possesses high crystal quality, thus the FETs fabricated with the exfoliated single layer MoS_2 and WS_2 usually have high mobility and on/off ratio. However, the FETs fabricated using the synthesized layer materials showed relatively low mobilities and on/off ratios. The highest mobility of the FET fabricated using the CVD grown MoS_2 was only 6 $cm^2V^{-1}s^{-1}$ with an on/off ratio about 10^5.[243] For the FETs fabricated with the CVD grown WS_2, the typical mobility 1 $cm^2V^{-1}s^{-1}$, and the highest mobility was only 4.1 $cm^2V^{-1}s^{-1}$ and its on/off ratio was 10^5.[244] Thus, significant work is needed for the development of high quality FETs over a large area for commercial application.

7.4 Summary

Uniform large-area ultra-thin WS_2 thin films, down to 40 nm, were obtained by the chemical etching method to fabricate ultra-thin FETs. The original WS_2 thin film contained many small crystallites scattered on the film surface. After etching the film

with a mixed acid solution of 7.5% H_2CrO_4 and 3.8% HF, the small crystallites were removed from the film surface. The etching rates of the layered WS_2 crystals are anisotropic, the lateral etching rate is faster than the vertical etching rate. The resistance of the acid-etched WS_2 thin film greatly increased and was higher than the calculated theoretical value due to the large number of defects generated during the etching process. By annealing the film under S atmosphere, the film resistance was recovered. The changes of the trap density after etching and annealing were analyzed by low frequency noise measurements. The current noise signal of the acid-etched WS_2 film is about one order of magnitude higher than that of the original film. After annealing under S atmosphere, the current noise signal was greatly reduced by about two orders of magnitude, which is even lower than that of the original film. Using the acid-etched and re-annealed WS_2 thin film as the channel layer, a working FET was fabricated, which showed a field-effect mobility of 0.31 $cm^2V^{-1}s^{-1}$ and an on/off ratio of 410. By depositing a 2 nm Al_2O_3 layer on the surface of the WS_2 channel layer, the on/off ratio and field-effect mobility remarkably increased to 2700 and 0.54 $cm^2V^{-1}s^{-1}$ due to the suppression of Coulomb scattering of the high-k environment.

CHAPTER 8 CONCLUSIONS AND SUGGESTIONS FOR FUTURE WORK

8.1 Conclusions

Tungsten disulfide, with its layered crystal structure, has great potential for the fabrication of ultra-thin and flexible electronic and optoelectronic devices due to its remarkable layer-dependent electrical and optical properties. The weak van der Waals force dominated layer interactions can accommodate large lattice mismatch with little interface defects, as the bonds within a unit layer are fully saturated, and this characteristic can be exploited for the growth of high-quality heterojunctions. Single-layer or few-layer WS_2 can be easily acquired by mechanical or chemical exfoliation from a single crystal for basic investigations and to fabricate proof-of-concept devices. However, the exfoliation method is limited to the microscale, which is not appropriate for large-scale production. In this thesis, we presented systematic experimental investigations of using MBE and CVD to grow wafer-scale p-type WS_2 thin films. In addition, WS_2/GaN p-n junctions with low leakage current were fabricated by the transfer of p-type WS_2 thin films onto n-type GaN, and ultra-thin WS_2-based FETs were fabricated using 40 nm WS_2 thin films as the channel layer.

For the MBE growth of WS_2, only the (002) family diffraction peaks were found in the XRD pattern of the WS_2 thin film, indicating strong preferential growth along the [001] crystal orientation of the WS_2 film. The WS_2 thin films change from small

vertical crystallites (type-I) to large parallel crystals (type-II) upon increasing the growth temperature from 450℃ to 700℃. The full width at half maximum of the rocking curve was reduced to 0.13° by increasing the amount of reactive S atoms.

For the CVD growth of WS_2, by using a thin Ni layer as texture promoter, the crystal structure of the WS_2 thin film changed from randomly oriented crystallites to large layered crystals with their c-axis oriented perpendicular to the substrate. By using Ni texture promoter, high-quality WS_2 thin films with carrier mobility as high as 63.3 cm^2/Vs can be obtained. The intensity of the XRD peaks of WS_2 with Ni promoter are much stronger than those of the film without a Ni layer, and the FWHM of the WS_2 with Ni promoter is only about one third of that of the film without a Ni layer, indicating the larger crystal size and better crystal quality. The liquid NiS_x phase, which has a melting point of 637 °C, in the sulfurization process served as liquid crystallization seeds for van der Waals rheotaxy, resulting in the horizontal growth of WS_2 layered crystals with enhanced crystal size.

The exfoliation and transfer the as-grown WS_2 thin films to arbitrary substrates is a key step for achieving practical devices. Compared to conventional epitaxial-grown heterojunctions, a wide range of semiconductors can be used for the fabrication of heterojunctions. Our etching-free transfer method utilizes the hydrophobicity of WS_2 and hydrophilicity of sapphire and maintains the integrity of the film without inducing cracks, in comparison with the conventional wet chemical etching transfer technique. Additionally, the etching-free approach does not require

the use of any destructive etchants and thereby permits the reuse of the substrates. The film quality and microstructure of the WS_2 layer are critical to the successful wafer-scale transfer of WS_2 thin films. It is extremely difficult to uniformly exfoliate WS_2 films without Ni promoter, and the separated film frequently cracked during the transfer process. Such phenomenon is believed to arise from the random orientation of the crystal structure, which hinders water molecules to uniformly penetrate into the interface between the film and the substrate. However, for the WS_2 film with Ni promoter, which contains large layered crystals parallel to the substrate, wafer-scale WS_2 thin films can be perfectly separated from the initial substrate and transferred to the target substrate.

The p-n junctions fabricated by the transfer of p-type WS_2 thin films onto n-type GaN had a quite low leakage current density of 29.6 $\mu A/cm^2$, whereas the direct-grown WS_2/GaN p-n junction had a large leakage current density of 92.4 mA/cm^2. This demonstrates the superior performance of the transferred device compared to the as-grown WS_2/GaN p-n junctions. The WS_2 films grown on sapphire substrates have larger crystal sizes and better crystal quality than the WS_2 films grown on GaN, which is the key reason for the lower leakage current of the transferred device. The degradation of the GaN layer at the high growth temperature of 1000 °C results in the WS_2 film having poor crystal quality. This etching-free transfer method is expected to enormously expand the applications of WS_2 thin films for optoelectronic and electronic devices.

Layered WS_2 thin films, which have fewer dangling bonds, are attractive for use as channel layers in ultra-thin FETs. In this thesis, uniform large-area ultra-thin WS_2 thin films, down to 40 nm, can be obtained by a chemical etching method to fabricate ultra-thin FETs. Using a mixed acid solution of H_2CrO_4 and HF, small crystallites can be removed from the surface of the WS_2 thin film. The etching rates of the layered WS_2 crystals are anisotropic, the lateral etching rate is faster than the vertical etching rate. The current noise signal of the acid-etched WS_2 film is about one order of magnitude higher than that of the original film. After annealing under S atmosphere, the noise signal of the WS_2 film was greatly reduced by about two orders of magnitude, which is even lower than that of the original film. The WS_2-based FET employing a 40 nm WS_2 thin film as the channel layer had a field-effect mobility and on/off ratio of 0.31 $cm^2V^{-1}s^{-1}$ and 410, respectively. By depositing a 2 nm Al_2O_3 layer on the surface of the WS_2 channel layer, the on/off ratio and field-effect mobility were greatly increased to 2700 and 0.54 $cm^2V^{-1}s^{-1}$, respectively, due to the suppression of Coulomb scattering of the high-k environment.

Layered materials can be exfoliated by mechanical or chemical methods to obtain high quality micron-sized single layer or few layers materials which are appropriate for fundamental investigations and the fabrication of proof-of-concept devices. However, the technique is not up scalable and hence it is not suitable for large-scale production. In this thesis, large-area WS_2 thin film growth using MBE and CVD were systematic investigated, and the wafer-scale p-type WS_2 thin films were sucussfully

obtianed. In addition, type-II WS_2 thin films with the layer WS_2 crystals parallel to the substrate were synthesised by CVD method using an ultra-thin Ni layer as texture promoter. These lay the foundation for the development of 2D electronic and optoelectronic devices. Most of the conductors and semiconductors become unstable at the growth temperature of WS_2. This presents a substantial barrier for the fabrication of WS_2-based heterojunctions and thereby greatly limiting the application of the material. The wafer-scale transfer method developed in this thesis is vital for electronic and optoelectronic applications due to its convenience for fabricating a wide range of heterojunctions without concerning the lattice mismatch, differences in the thermal expansion coefficient and optimization of the growth parameters on the target substrates. This approach greatly enhances the potential for applications of WS_2 thin films in electronic and optoelectronic devices and systems. For 2D layer materials, the force between cationic layers is dominated by van der Waals force, which theoretically provides the possibility of high tolerance in interface mismatch in a solid-state junction. In this thesis, the p-n junction was fabricated by transferring p-type WS_2 thin films onto the n-type GaN layer with a quite low leakage current density of 29.6 $\mu A/cm^2$ and the WS_2-based FET fabricated using 40 nm WS_2 thin films as the channel layer had a field-effect mobility of 0.54 $cm^2V^{-1}s^{-1}$ and on/off ratio of 2700. Though the performance of these devices cannot be comparable to traditional Si-based devices, it makes a big step forward. When scaling the gate length of a traditional Si-based FET, overlapping junctions lead to short channel effects which

degrade transistor performance. By introducing 2D materials in the channel of the FET, they could show superior immunity to short channel effects. Strong covalent bonds provide in-plane stability of 2D layer crystals, whereas relatively weak van der Waals forces are sufficient to keep the stack together. This makes it possible to fabricate multilayer van der Waals heterostructures and has been experimentally demonstrated.[245-247] 2D materials includes all necessary materials for the fabrication of 2D devices, such as graphene as conductor material, hexagonal boron nitride as dielectric material and MoS_2 and WS_2 as semiconductor material. The research on 2D materials is just at the beginning and it appears that it will remain an exciting research field. The 2D devices are promising candidates to next generation devices because of its high packing density, faster circuit speed and lower power consumption. We believed that eventually certain 2D materials will be widely used in electronics, such as 2D transistors, transparent electrodes, sensors, displays etc.

8.2 Suggestions for Future Work

In-depth studies are still needed to further improve the quality of the WS_2 thin film to achieve excellent electronic properties and make use of its novel layer-dependent electrical and optical properties, such as the lack of dangling bonds between each crystal layer and the layer-dependent bandgap, to fabricate high-quality electronic devices. The following are some promising research topics and directions

for future work.

1) Transfer of the wafer-scale p-type WS_2 film onto other n-type semiconductor materials to fabricate p-n junctions; in particular, wide bandgap n-type semiconductor materials could be used to fabricate solar cells with the as-made p-type WS_2 thin films. The transfer method permits versatile bandgap engineering for the fabrication of various p-n junctions.
2) The use of other two-dimensional materials, such as conductive graphene, dielectric hexagonal BN or other semiconducting TMDCs, with the p-type WS_2 thin films to fabricate novel 2D devices. The current microfabrication techniques of the semiconductor industry provide a good foundation for the fabrication of these novel devices.
3) The growth of n-type WS_2 by extrinsic doping, which can be used with the as-made p-type WS_2 thin films to fabricate homojunctions, or the growth of other n-type transition metal dichalcogenide materials, such as MoS_2, which is typically n-type in nature, to fabricate all chalcogenide p-n junctions.
4) The use of physical models to simulate and engineer the bandgap of heterojunctions fabricated with p-type WS_2 and other n-type materials to propose new designs for novel devices. First-principles calculations could be used to determine the possible n-type doping element for WS_2.

References

[1] Tilma B. W., Mangold M., Zaugg C. A., Link S. M., Waldburger D., et al., "Recent advances in ultrafast semiconductor disk lasers," *Light-Science & Applications*, vol. 4, pp. 14, 2015.

[2] Park D., Yang H., Jeong J., Ha K., Choi S., et al., "A comprehensive review of arsenic levels in the semiconductor manufacturing industry," *Annals of Occupational Hygiene*, vol. 54, pp. 869-879, 2010.

[3] Miller D. A. B., "Device requirements for optical interconnects to silicon chips," *Proceedings of the IEEE*, vol. 97, pp. 1166-1185, 2009.

[4] Zolper J. C., and Ieee, *Frontiers of compound semiconductor electronics*. IEEE Compound Semiconductor Integrated Circuit Symposium - 2007 IEEE Csic Symposium, Technology Digest. 2007, New York: Ieee. 7-10.

[5] Yamasaki K., and Horiguchi S., "Research trends and future directions in ultra-high-speed compound semiconductor IC technology," *Ntt Review*, vol. 8, pp. 10-16, 1996.

[6] Schaller Robert R, "Moore's law: past, present and future," *IEEE spectrum*, vol. 34, pp. 52-59, 1997.

[7] Watanabe Hiroshi, Yasuda Naoki, Toriumi Akira, Tanaka Tomoharu, and Tanzawa Toru, *Quantum tunneling effect device and semiconductor composite substrate*. 2001, Google Patents.

[8] Wang H., Yu L. L., Lee Y. H., Shi Y. M., Hsu A., et al., "Integrated circuits based on bilayer MoS_2 transistors," *Nano Letters*, vol. 12, pp. 4674-4680, 2012.

[9] Pu J., Yomogida Y., Liu K. K., Li L. J., Iwasa Y., et al., "Highly flexible MoS_2 thin-film transistors with ion gel dielectrics," *Nano Letters*, vol. 12, pp. 4013-4017, 2012.

[10] Perkins F. K., Friedman A. L., Cobas E., Campbell P. M., Jernigan G. G., et al., "Chemical vapor sensing with mono layer MoS_2," *Nano Letters*, vol. 13, pp. 668-673, 2013.

[11] Li H., Yin Z. Y., He Q. Y., Li H., Huang X., et al., "Fabrication of single- and multilayer MoS_2 film-based field-effect transistors for sensing no at room temperature," *Small*, vol. 8, pp. 63-67, 2012.

[12] Zhang W. J., Huang J. K., Chen C. H., Chang Y. H., Cheng Y. J., et al., "High-gain phototransistors based on a CVD MoS_2 monolayer," *Advanced Materials*, vol. 25, pp. 3456-3461, 2013.

[13] Roy K., Padmanabhan M., Goswami S., Sai T. P., Ramalingam G., et al., "Graphene-MoS_2 hybrid structures for multifunctional photoresponsive memory devices," *Nature Nanotechnology*, vol. 8, pp. 826-830, 2013.

[14] Yu Lili, Lee Yi-Hsien, Ling Xi, Santos Elton J. G., Shin Yong Cheol, et al., "Graphene/MoS_2 hybrid technology for large-scale two-dimensional electronics," *Nano Letters*, vol. 14, pp. 3055-3063, 2014.

[15] Novoselov K. S., Geim A. K., Morozov S. V., Jiang D., Zhang Y., et al., "Electric field effect in atomically thin carbon films," *Science*, vol. 306, pp. 666-669, 2004.

[16] Lee Changgu, Wei Xiaoding, Kysar Jeffrey W., and Hone James, "Measurement of the elastic properties and intrinsic strength of monolayer graphene," *Science*, vol. 321, pp. 385-388, 2008.

[17] Stankovich Sasha, Dikin Dmitriy A., Piner Richard D., Kohlhaas Kevin A., Kleinhammes Alfred, et al., "Synthesis of graphene-based nanosheets via chemical reduction of exfoliated graphite oxide," *Carbon*, vol. 45, pp. 1558-1565, 2007.

[18] Yoo Jung Joon, Balakrishnan Kaushik, Huang Jingsong, Meunier Vincent, Sumpter Bobby G., et al., "Ultrathin planar graphene supercapacitors," *Nano Letters*, vol. 11, pp. 1423-1427, 2011.

[19] Eigler S., and Hirsch A., "Chemistry with graphene and graphene oxide-challenges for synthetic chemists," *Angewandte Chemie-International Edition*, vol. 53, pp. 7720-7738, 2014.

[20] Ganatra R., and Zhang Q., "Few-layer MoS_2: a promising layered semiconductor," *Acs Nano*, vol. 8, pp. 4074-4099, 2014.

[21] Lembke D., Bertolazzi S., and Kis A., "Single-layer MoS_2 electronics," *Accounts of Chemical Research*, vol. 48, pp. 100-110, 2015.

[22] Wang Q. H., Kalantar-Zadeh K., Kis A., Coleman J. N., and Strano M. S., "Electronics and optoelectronics of two-dimensional transition metal dichalcogenides," *Nature Nanotechnology*, vol. 7, pp. 699-712, 2012.

[23] Chhowalla M., Shin H. S., Eda G., Li L. J., Loh K. P., et al., "The chemistry of two-dimensional layered transition metal dichalcogenide nanosheets," *Nature Chemistry*, vol. 5, pp. 263-275, 2013.

[24] McDonnell S. J., and Wallace R. M., "Atomically-thin layered films for device applications based upon 2D TMDC materials," *Thin Solid Films*, vol. 616, pp. 482-501, 2016.

[25] Stoller Meryl D., Park Sungjin, Zhu Yanwu, An Jinho, and Ruoff Rodney S., "Graphene-based ultracapacitors," *Nano Letters*, vol. 8, pp. 3498-3502, 2008.

[26] Wu Zhong-Shuai, Ren Wencai, Gao Libo, Liu Bilu, Jiang Chuanbin, et al., "Synthesis of high-quality graphene with a pre-determined number of layers," *Carbon*, vol. 47, pp. 493-499, 2009.

[27] Geim A. K., and Grigorieva I. V., "Van der Waals heterostructures," *Nature*, vol. 499, pp. 419-425, 2013.

[28] Rao C. N. R., Matte Hssr, and Maitra U., "Graphene analogues of inorganic layered materials," *Angewandte Chemie-International Edition*, vol. 52, pp. 13162-13185, 2013.

[29] Sorkin V., Pan H., Shi H., Quek S. Y., and Zhang Y. W., "Nanoscale transition metal dichalcogenides: structures, properties and applications," *Critical Reviews in Solid State and Materials Sciences*, vol. 39, pp. 319-367, 2014.

[30] Saito R., Tatsumi Y., Huang S., Ling X., and Dresselhaus M. S., "Raman

spectroscopy of transition metal dichalcogenides," *Journal of Physics-Condensed Matter*, vol. 28, pp. 16, 2016.

[31] Gong Y. J., Lei S. D., Ye G. L., Li B., He Y. M., et al., "Two-step growth of two-dimensional $WSe_2/MoSe_2$ heterostructures," *Nano Letters*, vol. 15, pp. 6135-6141, 2015.

[32] Fan Y., Zhou Y. Q., Wang X. C., Tan H. J., Rong Y. M., et al., "Photoinduced schottky barrier lowering in 2D monolayer WS_2 photodetectors," *Advanced Optical Materials*, vol. 4, pp. 1573-1581, 2016.

[33] Zou X. M., Wang J. L., Chiu C. H., Wu Y., Xiao X. H., et al., "Interface engineering for high-performance top-gated MoS_2 field-effect transistors," *Advanced Materials*, vol. 26, pp. 6255-6261, 2014.

[34] Lembke D., and Kis A., "Breakdown of high-performance monolayer MoS_2 transistors," *Acs Nano*, vol. 6, pp. 10070-10075, 2012.

[35] Xu K., Yin L., Huang Y., Shifa T. A., Chu J. W., et al., "Synthesis, properties and applications of 2D layered (MXVI)-X-III (M = Ga, In; X = S, Se, Te) materials," *Nanoscale*, vol. 8, pp. 16802-16818, 2016.

[36] Tian H., Chin M. L., Najmaei S., Guo Q. S., Xia F. N., et al., "Optoelectronic devices based on two-dimensional transition metal dichalcogenides," *Nano Research*, vol. 9, pp. 1543-1560, 2016.

[37] Roldan R., Silva-Guillen J. A., Lopez-Sancho M. P., Guinea F., Cappelluti E., et al., "Electronic properties of single-layer and multilayer transition metal dichalcogenides MX_2 (M = Mo, W and X = S, Se)," *Annalen Der Physik*, vol. 526, pp. 347, 2014.

[38] Fu Q., and Xiang B., "Monolayer transition metal disulfide: Synthesis, characterization and applications," *Progress in Natural Science-Materials International*, vol. 26, pp. 221-231, 2016.

[39] Wong S. L., Liu H. F., and Chi D. Z., "Recent progress in chemical vapor deposition growth of two-dimensional transition metal dichalcogenides," *Progress in Crystal Growth and Characterization of Materials*, vol. 62, pp. 9-28, 2016.

[40] Xu G. C., Lu Z. X., Zhang Q., Qiu H. L., and Jiao L. Y., "synthesis of two-dimensional transition metal dichalcogenides with chemical vapor deposition," *Acta Chimica Sinica*, vol. 73, pp. 895-901, 2015.

[41] Dickinson R. G., and Pauling L., "The crystal structure of molybdenite," *Journal of the American Chemical Society*, vol. 45, pp. 1466-1471, 1923.

[42] Liu H. F., Wong S. L., and Chi D. Z., "CVD growth of MoS_2-based two-dimensional materials," *Chemical Vapor Deposition*, vol. 21, pp. 241-259, 2015.

[43] Molina-Sanchez A., Hummer K., and Wirtz L., "Vibrational and optical properties of MoS_2: From monolayer to bulk," *Surface Science Reports*, vol. 70, pp. 554-586, 2015.

[44] Ye Mingxiao, Winslow Dustin, Zhang Dongyan, Pandey Ravindra, and Yap Yoke, "Recent advancement on the optical properties of two-dimensional

molybdenum disulfide (MoS_2) thin films," *Photonics*, vol. 2, pp. 288, 2015.

[45] Kuc Agnieszka, *Low-dimensional transition-metal dichalcogenides*, in *Chemical Modelling: Volume 11*. 2015, The Royal Society of Chemistry. p. 1-29.

[46] Jellinek F., Brauer G., and Muller H., "Molybdenum and niobium sulphides," *Nature*, vol. 185, pp. 376-377, 1960.

[47] Gu P. C., Zhang K. L., Feng Y. L., Wang F., Miao Y. P., et al., "Recent progress of two-dimensional layered molybdenum disulfide," *Acta Physica Sinica*, vol. 65, pp. 9, 2016.

[48] Sandoval S. J., Yang D., Frindt R. F., and Irwin J. C., "Raman-study and lattice-dynamics of single molecular layers of MoS_2," *Physical Review B*, vol. 44, pp. 3955-3962, 1991.

[49] Lukowski Mark A., Daniel Andrew S., English Caroline R., Meng Fei, Forticaux Audrey, et al., "Highly active hydrogen evolution catalysis from metallic WS_2 nanosheets," *Energy & Environmental Science*, vol. 7, pp. 2608, 2014.

[50] Liu X., Huang H. S., Huang M. S., Liu Z. J., *Fabrication and Characterization of Few-layer Tungsten Disulfide (WS_2) Field Effect Transistors*, in *7th IEEE International Nanoelectronics Conference*. 2016, IEEE: New York.

[51] Li W., Wang T. X., Dai X. Q., Wang X. L., Zhai C. Y., et al., "Bandgap engineering of different stacking WS_2 bilayer under an external electric field," *Solid State Communications*, vol. 225, pp. 32-37, 2016.

[52] Wang Y. L., Cong C. X., Yang W. H., Shang J. Z., Peimyoo N., et al., "Strain-induced direct-indirect bandgap transition and phonon modulation in monolayer WS_2," *Nano Research*, vol. 8, pp. 2562-2572, 2015.

[53] Kuc A., Zibouche N., and Heine T., "Influence of quantum confinement on the electronic structure of the transition metal sulfide TS_2," *Physical Review B*, vol. 83, pp. 4, 2011.

[54] Choi J., Zhang H. Y., and Choi J. H., "Modulating optoelectronic properties of two dimensional transition metal dichalcogenide semiconductors by photoinduced charge transfer," *Acs Nano*, vol. 10, pp. 1671-1680, 2016.

[55] Mak K. F., He K. L., Shan J., and Heinz T. F., "Control of valley polarization in monolayer MoS_2 by optical helicity," *Nature Nanotechnology*, vol. 7, pp. 494-498, 2012.

[56] Zeng H. L., Dai J. F., Yao W., Xiao D., and Cui X. D., "Valley polarization in MoS_2 monolayers by optical pumping," *Nature Nanotechnology*, vol. 7, pp. 490-493, 2012.

[57] Terrones H., Lopez-Urias F., and Terrones M., "Novel hetero-layered materials with tunable direct band gaps by sandwiching different metal disulfides and diselenides," *Scientific Reports*, vol. 3, pp. 7, 2013.

[58] Wang Qing Hua, Kalantar-Zadeh Kourosh, Kis Andras, Coleman Jonathan N., and Strano Michael S., "Electronics and optoelectronics of two-dimensional

transition metal dichalcogenides," *Nat Nano*, vol. 7, pp. 699-712, 2012.
[59] Eda G., Yamaguchi H., Voiry D., Fujita T., Chen M. W., et al., "Photoluminescence from chemically exfoliated MoS_2," *Nano Letters*, vol. 11, pp. 5111-5116, 2011.
[60] O'Neill A., Khan U., and Coleman J. N., "Preparation of high concentration dispersions of exfoliated MoS_2 with increased flake size," *Chemistry of Materials*, vol. 24, pp. 2414-2421, 2012.
[61] Li H., Wu J. M. T., Yin Z. Y., and Zhang H., "Preparation and applications of mechanically exfoliated single-layer and multi-layer MoS_2 and WSe_2 nanosheets," *Accounts of Chemical Research*, vol. 47, pp. 1067-1075, 2014.
[62] Shang J. Q., Xue F., and Ding E. Y., "Efficient exfoliation of molybdenum disulphide nanosheets by a high-pressure homogeniser," *Micro & Nano Letters*, vol. 10, pp. 589-591, 2015.
[63] Zhang S. L., Jung H., Huh J. S., Yu J. B., and Yang W. C., "Efficient exfoliation of MoS_2 with volatile solvents and their application for humidity sensor," *Journal of Nanoscience and Nanotechnology*, vol. 14, pp. 8518-8522, 2014.
[64] Goncalves R. H., Fiel R., Soares M. R. S., Schreiner W. H., Silva C. M. P., et al., "Single-step exfoliation and covalent functionalization of MoS_2 nanosheets by an organosulfur reaction," *Chemistry-a European Journal*, vol. 21, pp. 15583-15588, 2015.
[65] Shao Y. Y., Wang J., Wu H., Liu J., Aksay I. A., et al., "Graphene based electrochemical sensors and biosensors: a review," *Electroanalysis*, vol. 22, pp. 1027-1036, 2010.
[66] Stankovich S., Dikin D. A., Dommett G. H. B., Kohlhaas K. M., Zimney E. J., et al., "Graphene-based composite materials," *Nature*, vol. 442, pp. 282-286, 2006.
[67] Fang H., Chuang S., Chang T. C., Takei K., Takahashi T., et al., "High-performance single layered WSe_2 p-FETs with chemically doped contacts," *Nano Letters*, vol. 12, pp. 3788-3792, 2012.
[68] Novoselov K. S., Jiang D., Schedin F., Booth T. J., Khotkevich V. V., et al., "Two-dimensional atomic crystals," *Proceedings of the National Academy of Sciences of the United States of America*, vol. 102, pp. 10451-10453, 2005.
[69] Braga D., Lezama I. G., Berger H., and Morpurgo A. F., "Quantitative determination of the band gap of WS_2 with ambipolar ionic liquid-gated transistors," *Nano Letters*, vol. 12, pp. 5218-5223, 2012.
[70] Srivastava V. K., Quinlan R. A., Agapov A. L., Dunlap J. R., Nelson K. M., et al., "Macroscopic properties of restacked, redox-liquid exfoliated graphite and graphite mimics produced in bulk quantities," *Advanced Functional Materials*, vol. 24, pp. 4969-4977, 2014.
[71] Ciesielski A., and Samori P., "Graphene via sonication assisted liquid-phase exfoliation," *Chemical Society Reviews*, vol. 43, pp. 381-398, 2014.
[72] Coleman J. N., Lotya M., O'Neill A., Bergin S. D., King P. J., et al., "Two-

dimensional nanosheets produced by liquid exfoliation of layered materials," *Science*, vol. 331, pp. 568-571, 2011.

[73] Lee K., Kim H. Y., Lotya M., Coleman J. N., Kim G. T., et al., "Electrical characteristics of molybdenum disulfide flakes produced by liquid exfoliation," *Advanced Materials*, vol. 23, pp. 4178-+, 2011.

[74] Coleman J. N., "Liquid exfoliation of defect-free graphene," *Accounts of Chemical Research*, vol. 46, pp. 14-22, 2013.

[75] Benavente E., Santa Ana M. A., Mendizabal F., and Gonzalez G., "Intercalation chemistry of molybdenum disulfide," *Coordination Chemistry Reviews*, vol. 224, pp. 87-109, 2002.

[76] Py M. A., and Haering R. R., "Structural destabilization induced by lithium intercalation in MoS_2 and related-compounds," *Canadian Journal of Physics*, vol. 61, pp. 76-84, 1983.

[77] Mulhern P. J., "Lithium intercalation in crystalline MoS_2," *Canadian Journal of Physics*, vol. 67, pp. 1049-1052, 1989.

[78] Morales J., Santos J., and Tirado J. L., "Electrochemical studies of lithium and sodium intercalation in $MoSe_2$," *Solid State Ionics*, vol. 83, pp. 57-64, 1996.

[79] Tsai H. L., Heising J., Schindler J. L., Kannewurf C. R., and Kanatzidis M. G., "Exfoliated-restacked phase of WS_2," *Chemistry of Materials*, vol. 9, pp. 879-&, 1997.

[80] Zeng T., You Y. C., Wang X. F., Hu T. S., and Tai G. A., "Chemical vapor deposition and device application of two-dimensional molybdenum disulfide-based atomic crystals," *Progress in Chemistry*, vol. 28, pp. 459-470, 2016.

[81] Li X. S., Cai W. W., An J. H., Kim S., Nah J., et al., "Large-area synthesis of high-quality and uniform graphene films on copper foils," *Science*, vol. 324, pp. 1312-1314, 2009.

[82] Yu J. X., Li J., Zhang W. F., and Chang H. X., "Synthesis of high quality two-dimensional materials via chemical vapor deposition," *Chemical Science*, vol. 6, pp. 6705-6716, 2015.

[83] Song J. G., Park J., Lee W., Choi T., Jung H., et al., "Layer-controlled, wafer-scale, and conformal synthesis of tungsten disulfide nanosheets using atomic layer deposition," *Acs Nano*, vol. 7, pp. 11333-11340, 2013.

[84] Shidpour R., Vosoughi M., Maghsoudi H., and Simchi A., "A general two-step chemical vapor deposition procedure to synthesize highly crystalline transition metal dichalcogenides: A case study of MoS_2," *Materials Research Bulletin*, vol. 76, pp. 473-478, 2016.

[85] You Y. C., Zeng T., Liu J. S., Hu T. S., and Tai G. A., "Chemical vapor deposition and application of graphene-like tungsten disulfide," *Progress in Chemistry*, vol. 27, pp. 1578-1590, 2015.

[86] Wen Y. Y., Zeng X. B., Chen X. X., Wang W. Z., Ding J., et al., *Synthesis of monolayer MoS_2 by CVD approach*, in *Proceedings of the 2nd Annual International Conference on Advanced Material Engineering*, A.K.

Bhatnagar, et al., Editors. 2016, Atlantis Press: Paris. p. 1034-1039.
[87] Shi Y. M., Li H. N., and Li L. J., "Recent advances in controlled synthesis of two-dimensional transition metal dichalcogenides via vapour deposition techniques," *Chemical Society Reviews*, vol. 44, pp. 2744-2756, 2015.
[88] Wang X., Zhang Y. P., and Chen Z. Q., "Effect of MoO_3 constituents on the growth of MoS_2 nanosheets by chemical vapor deposition," *Materials Research Express*, vol. 3, pp. 7, 2016.
[89] Cho W. C., Wu K. L., Yip P. S., Wang X. S., Chai Y., et al., "Selectable synthesis of 2-D MoS_2 and its electronic devices: from isolated triangular islands to large-area continuous thin film," *IEEE Transactions on Nanotechnology*, vol. 15, pp. 310-317, 2016.
[90] Radisavljevic B., Radenovic A., Brivio J., Giacometti V., and Kis A., "Single-layer MoS_2 transistors," *Nature Nanotechnology*, vol. 6, pp. 147-150, 2011.
[91] Li L. K., Yu Y. J., Ye G. J., Ge Q. Q., Ou X. D., et al., "Black phosphorus field-effect transistors," *Nature Nanotechnology*, vol. 9, pp. 372-377, 2014.
[92] Levi R., Bitton O., Leitus G., Tenne R., and Joselevich E., "Field-effect transistors based on WS_2 nanotubes with high current-carrying capacity," *Nano Letters*, vol. 13, pp. 3736-3741, 2013.
[93] Podzorov V., Gershenson M. E., Kloc C., Zeis R., and Bucher E., "High-mobility field-effect transistors based on transition metal dichalcogenides," *Applied Physics Letters*, vol. 84, pp. 3301-3303, 2004.
[94] Ayari A., Cobas E., Ogundadegbe O., and Fuhrer M. S., "Realization and electrical characterization of ultrathin crystals of layered transition-metal dichalcogenides," *Journal of Applied Physics*, vol. 101, pp. 5, 2007.
[95] Lee H. S., Min S. W., Park M. K., Lee Y. T., Jeon P. J., et al., "MoS_2 nanosheets for top-gate nonvolatile memory transistor channel," *Small*, vol. 8, pp. 3111-3115, 2012.
[96] Ganapathi K. L., Bhattacharjee S., Mohan S., and Bhat N., "High-performance HfO_2 back gated multilayer MoS_2 transistors," *IEEE Electron Device Letters*, vol. 37, pp. 797-800, 2016.
[97] Zheng Z. Q., Zhang T. M., Yao J. D., Zhang Y., Xu J. R., et al., "Flexible, transparent and ultra-broadband photodetector based on large-area WSe_2 film for wearable devices," *Nanotechnology*, vol. 27, pp. 11, 2016.
[98] Liu J. X., Cao H., Jiang B., Xue Y. H., and Fu L., "Newborn 2D materials for flexible energy conversion and storage," *Science China-Materials*, vol. 59, pp. 459-474, 2016.
[99] Kim S. J., Choi K., Lee B., Kim Y., and Hong B. H., *Materials for Flexible, Stretchable Electronics: Graphene and 2D Materials*, in *Annual Review of Materials Research, Vol 45*, D.R. Clarke, Editor. 2015, Annual Reviews: Palo Alto. p. 63-84.
[100] Lee S. K., Jang H. Y., Jang S., Choi E., Hong B. H., et al., "All graphene-based thin film transistors on flexible plastic substrates," *Nano Letters*, vol. 12, pp. 3472-3476, 2012.

[101] Chopra K. L., Major S., and Pandya D. K., "Transparent conductors - a status review," *Thin Solid Films*, vol. 102, pp. 1-46, 1983.
[102] Ellmer K., "Past achievements and future challenges in the development of optically transparent electrodes," *Nature Photonics*, vol. 6, pp. 808-816, 2012.
[103] Alharbi F., Bass J. D., Salhi A., Alyamani A., Kim H. C., et al., "Abundant non-toxic materials for thin film solar cells: Alternative to conventional materials," *Renewable Energy*, vol. 36, pp. 2753-2758, 2011.
[104] Yin Z. Y., Li H., Li H., Jiang L., Shi Y. M., et al., "Single-layer MoS_2 phototransistors," *Acs Nano*, vol. 6, pp. 74-80, 2012.
[105] Hellman O., "Topics in solid phase epitaxy: Strain, structure and geometry," *Materials Science & Engineering R-Reports*, vol. 16, pp. 1-42, 1996.
[106] Gornert P., "Kinetics and mechanisms of flux crystal-growth," *Progress in Crystal Growth and Characterization of Materials*, vol. 20, pp. 263-284, 1990.
[107] Wu O. K., Rajavel R. D., and Jensen J. E., "Status of II-VT molecular-beam epitaxy technology," *Materials Chemistry and Physics*, vol. 43, pp. 103-107, 1996.
[108] Elarde V. C., and Coleman J. J., "Nanoscale selective area epitaxy for optoelectronic devices," *Progress in Quantum Electronics*, vol. 31, pp. 225-257, 2007.
[109] Di Cioccio L., and Neyret E., "Homoepitaxy of silicon carbide," *Vide-Science Technique Et Applications*, vol. 55, pp. 380, 2000.
[110] Masri P., Pezoldt J., Sumiya M., and Averous M., *Physics of heteroepitaxy and heterophases*, in *Silicon Carbide and Related Materials 2001, Pts 1 and 2, Proceedings*, S. Yoshida, et al., Editors. 2002, Trans Tech Publications Ltd: Zurich-Uetikon. p. 379-382.
[111] Hull R., and Bean J. C., "Misfit dislocations in lattice-mismatched epitaxial-films," *Critical Reviews in Solid State and Materials Sciences*, vol. 17, pp. 507-546, 1992.
[112] Demeester P., Ackaert A., Coudenys G., Moerman I., Buydens L., et al., "Relaxed lattice-mismatched growth of iii-v semiconductors," *Progress in Crystal Growth and Characterization of Materials*, vol. 22, pp. 53-141, 1991.
[113] Matthias Opel, "Spintronic oxides grown by laser-MBE," *Journal of Physics D: Applied Physics*, vol. 45, pp. 033001, 2012.
[114] Silveira J. P., and Briones F., "In situ observation of reconstruction related surface stress during molecular beam epitaxy (MBE) growth of III–V compounds," *Journal of Crystal Growth*, vol. 201–202, pp. 113-117, 1999.
[115] Kroger F. A., "Defect chemistry in crystalline solids," *Annual Review of Materials Science*, vol. 7, pp. 449-475, 1977.
[116] Wagner C., "Point-defects and their interaction," *Annual Review of Materials Science*, vol. 7, pp. 1-22, 1977.
[117] Wicks G. W., "Molecular-beam epitaxy of iii-v semiconductors," *Critical Reviews in Solid State and Materials Sciences*, vol. 18, pp. 239-260, 1993.
[118] Herman M. A., and Sitter H., "MBE growth physics: Application to device

technology," *Microelectronics Journal*, vol. 27, pp. 257-296, 1996.
[119] Shen X. Q., Shimizu M., Yamamoto T., Honda Y., and Okumura H., "Characterizations of GaN films and GaN/AlN super-lattice structures grown on vicinal sapphire (0001) substrates by RF-MBE," *Journal of Crystal Growth*, vol. 278, pp. 378-382, 2005.
[120] Milnes A. G., and Polyakov A. Y., "Indium arsenide - a semiconductor for high-speed and electrooptical devices," *Materials Science and Engineering B-Solid State Materials for Advanced Technology*, vol. 18, pp. 237-259, 1993.
[121] Pienkos T., Halas S., and Czarnacki M., "High temperature resistivity determination of high-melting point metals and alloys," *Vacuum*, vol. 85, pp. 498-501, 2010.
[122] Dubrovskii V. G., Cirlin G. E., Bauman D. A., Kozachek V. V., and Mareev V. V., "Kinetic models of self-organization effects in lattice systems," *Physica a-Statistical Mechanics and Its Applications*, vol. 260, pp. 349-373, 1998.
[123] Cho A. Y., and Arthur J. R., "Molecular beam epitaxy," *Progress in Solid State Chemistry*, vol. 10, Part 3, pp. 157-191, 1975.
[124] Latyshev A. V., Krasilnikov A. B., and Aseev A. L., "Direct UHV-REM observation of the behavior of monatomic steps on the silicon (111) surface," *Physica Status Solidi a-Applied Research*, vol. 146, pp. 251-257, 1994.
[125] *Computational and Theoretical Techniques for Materials Science*. 1995, Washington, DC: The National Academies Press. 58.
[126] Markov I., "Recent theoretical developments in epitaxy," *Materials Chemistry and Physics*, vol. 36, pp. 1-30, 1993.
[127] Koch R., "The intrinsic stress of polycrystalline and epitaxial thin metal-films," *Journal of Physics-Condensed Matter*, vol. 6, pp. 9519-9550, 1994.
[128] Koch R., Winau D., Führmann A., and Rieder K. H., "Growth-mode-specific intrinsic stress of thin silver films," *Physical Review B*, vol. 44, pp. 3369-3372, 1991.
[129] Daudin B, Widmann F, Feuillet G, Samson Y, Arlery M, et al., "Stranski-Krastanov growth mode during the molecular beam epitaxy of highly strained GaN," *Physical Review B*, vol. 56, pp. R7069, 1997.
[130] Koma A., "Van der Waals epitaxy for highly lattice-mismatched systems," *Journal of Crystal Growth*, vol. 201, pp. 236-241, 1999.
[131] Koma Atsushi, Sunouchi Kazumasa, and Miyajima Takao, "Fabrication and characterization of heterostructures with subnanometer thickness," *Microelectronic Engineering*, vol. 2, pp. 129-136, 1984.
[132] Koma Atsushi, "Van der Waals epitaxy-a new epitaxial growth method for a highly lattice-mismatched system," *Thin Solid Films*, vol. 216, pp. 72-76, 1992.
[133] Onomitsu K., Krajewska A., Neufeld R. A. E., Maeda F., Kumakura K., et al., "Epitaxial growth of monolayer $MoSe_2$ on GaAs," *Applied Physics Express*, vol. 9, pp. 4, 2016.
[134] Kudrynskyi Z. R., Bakhtinov A. P., Vodopyanov V. N., Kovalyuk Z. D.,

Tovarnitskii M. V., et al., "Fabrication and characterization of PbSe nanostructures on van der Waals surfaces of GaSe layered semiconductor crystals," *Nanotechnology*, vol. 26, pp. 9, 2015.

[135] Cao N. T., Zhang L., Lu L., Xie H. P., Huang H., et al., "The van der Waals heterostructure of CuPc/MoS_2(0001)," *Acta Physica Sinica*, vol. 63, pp. 8, 2014.

[136] Elahi A. S., and Ghoranneviss M., "Review of the chemical vapour deposition applications for the microelectronic devices," *International Journal of Materials & Product Technology*, vol. 52, pp. 353-361, 2016.

[137] Kuzminykh Y., Dabirian A., Reinke M., and Hoffmann P., "High vacuum chemical vapour deposition of oxides: A review of technique development and precursor selection," *Surface & Coatings Technology*, vol. 230, pp. 13-21, 2013.

[138] Weiss F., Senateur J. P., Dubourdieu C., Galindo V., and Lindner J., "MOCVD preparation of oxide films," *Vide-Science Technique Et Applications*, vol. 53, pp. 561, 1998.

[139] Neyts E. C., "PECVD growth of carbon nanotubes: From experiment to simulation," *Journal of Vacuum Science & Technology B*, vol. 30, pp. 17, 2012.

[140] Yang J., Wang S., Yang F. S., Zhang Z. P., Ding Z., et al., "In-situ growth of superconducting MgB_2 thin films by HPCVD method at low temperature," *Physica C-Superconductivity and Its Applications*, vol. 467, pp. 1-3, 2007.

[141] *Thin film processes II*, J.L. Vossen and W. Kern, Editors. 1991, Academic Press: Boston :.

[142] Simpkins PG, Greenberg-Kosinski S, and MacChesney JB, "Thermophoresis: the mass transfer mechanism in modified chemical vapor deposition," *Journal of Applied Physics*, vol. 50, pp. 5676-5681, 1979.

[143] Fang H, Yang ZJ, Wang Y, Dai T, Sang LW, et al., "Analysis of mass transport mechanism in InGaN epitaxy on ridge shaped selective area growth GaN by metal organic chemical vapor deposition," *Journal of Applied Physics*, vol. 103, pp. 014908, 2008.

[144] Jeffrey DJ, and Onishi Y, "Calculation of the resistance and mobility functions for two unequal rigid spheres in low-Reynolds-number flow," *Journal of Fluid Mechanics*, vol. 139, pp. 261-290, 1984.

[145] Pierson Hugh O, *Handbook of chemical vapor deposition: principles, technology and applications*. 1999: William Andrew.

[146] Rockett Angus, *The materials science of semiconductors*. 2007: Springer Science & Business Media.

[147] Hitchman Michael L, Fischer RA, and Jensen KF, "Chemical vapor deposition. principles and applications," *Angewandte Chemie-English Edition*, vol. 33, pp. 1403, 1994.

[148] Fujinaga T., Takagi M., Hashimoto M., Asari S., and Saito K., "Effect of hydrogen on SiNx films deposited by Cat-CVD method," *Thin Solid Films*, vol. 516, pp. 615-617, 2008.

[149] Kumar A, and Lee CH, *Synthesis and Biomedical Applications of Graphene: Present and Future Trends, Advances in Graphene Science*. 2013, InTech.
[150] Brown William A, and Kamins Theodore I, "Analysis of LPCVD system parameters for polysilicon, silicon-nitride and silicon dioxide deposition," *Solid State Technology*, vol. 22, pp. 51-&, 1979.
[151] Ketchum Jeffrey M, *Apparatus and method for removing deposits from an APCVD system*. 1995, Google Patents.
[152] Zhou X., Chen Q., Zhang Q. M., and Zhang S. H., "Dielectric behavior of bilayer films of P(VDF-CTFE) and low temperature PECVD fabricated Si_3N_4," *IEEE Transactions on Dielectrics and Electrical Insulation*, vol. 18, pp. 463-470, 2011.
[153] Wang S-B, and Wendt Amy E, "Control of ion energy distribution at substrates during plasma processing," *Journal of Applied Physics*, vol. 88, pp. 643-646, 2000.
[154] Schmidt Jan, Kerr Mark, and Cuevas Andrés, "Surface passivation of silicon solar cells using plasma-enhanced chemical-vapour-deposited SiN films and thin thermal SiO_2/plasma SiN stacks," *Semiconductor Science and Technology*, vol. 16, pp. 164, 2001.
[155] Krawitz Aaron D, "Introduction to diffraction in materials science and engineering," *Introduction to Diffraction in Materials Science and Engineering, by Aaron D. Krawitz, pp. 424. ISBN 0-471-24724-3. Wiley-VCH, April 2001.*, vol. 424, 2001.
[156] Chisholm JE, "The basics of crystallography and diffraction," *Mineralogical Magazine*, vol. 62, pp. 131-131, 1998.
[157] Dyson David John, *X-ray and electron diffraction studies in materials science*. Vol. 776. 2004: Maney Pub.
[158] Long Derek Albert, and Long DA, *Raman spectroscopy*. 1977: McGraw-Hill New York.
[159] Nie Shuming, and Emory Steven R, "Probing single molecules and single nanoparticles by surface-enhanced Raman scattering," *science*, vol. 275, pp. 1102-1106, 1997.
[160] Haynes Christy L, McFarland Adam D, and Van Duyne Richard P, "Raman spectroscopy," *Analytical chemistry*, vol., 2005.
[161] Goldstein Joseph, Newbury Dale E, Echlin Patrick, Joy David C, Romig Jr Alton D, et al., *Scanning electron microscopy and X-ray microanalysis: a text for biologists, materials scientists, and geologists*. 2012: Springer Science & Business Media.
[162] Goldstein Joseph I, Newbury Dale E, Echlin Patrick, Joy David C, Fiori Charles, et al., *Electron-Beam-Specimen Interactions*, in *Scanning Electron Microscopy and X-ray Microanalysis*. 1981, Springer. p. 53-122.
[163] Binnig Gerd, Quate Calvin F, and Gerber Ch, "Atomic force microscope," *Physical review letters*, vol. 56, pp. 930, 1986.
[164] Eaton Peter, and West Paul, *Atomic force microscopy*. 2010: Oxford

University Press.
[165] Saint Jean M, Hudlet S, Guthmann C, and Berger J, "Van der Waals and capacitive forces in atomic force microscopies," *Journal of Applied Physics*, vol. 86, pp. 5245-5248, 1999.
[166] Bruch LW, "Evaluation of the van der Waals force for atomic force microscopy," *Physical Review B*, vol. 72, pp. 033410, 2005.
[167] Murnaghan FD, "The compressibility of media under extreme pressures," *Proceedings of the National Academy of Sciences*, vol. 30, pp. 244-247, 1944.
[168] Chastain Jill, King Roger C, and Moulder JF, *Handbook of X-ray photoelectron spectroscopy: a reference book of standard spectra for identification and interpretation of XPS data*. 1995: Physical Electronics Eden Prairie, MN.
[169] Wagner Ch D, and Muilenberg GE, *Handbook of X-ray photoelectron spectroscopy*. 1979: Perkin-Elmer.
[170] Seah MP, "The quantitative analysis of surfaces by XPS: a review," *Surface and Interface Analysis*, vol. 2, pp. 222-239, 1980.
[171] Jansson C, Tougaard S, Beamson G, Briggs D, Davies SF, et al., "Intercomparison of algorithms for background correction in XPS," *Surface and interface analysis*, vol. 23, pp. 484-494, 1995.
[172] Zhang Riqing, Zhang Panfeng, Kang Tingting, Fan Haibo, Liu Xianglin, et al., "Determination of the valence band offset of wurtzite InN/ZnO heterojunction by x-ray photoelectron spectroscopy," *Applied Physics Letters*, vol. 91, pp. 162104, 2007.
[173] Zhang PF, Liu XL, Zhang RQ, Fan HB, Yang AL, et al., "Valence band offset of ZnO/GaAs heterojunction measured by X-ray photoelectron spectroscopy," *Applied Physics Letters*, vol. 92, pp. 012104, 2008.
[174] Yang Zhi-Guo, Zhu Li-Ping, Guo Yan-Min, Tian Wei, Ye Zhi-Zhen, et al., "Valence-band offset of p-NiO/n-ZnO heterojunction measured by X-ray photoelectron spectroscopy," *Physics Letters A*, vol. 375, pp. 1760-1763, 2011.
[175] Morkel Matthias, Weinhardt L, Lohmüller B, Heske Clement, Umbach Eberhard, et al., "Flat conduction-band alignment at the CdS/$CuInSe_2$ thin-film solar-cell heterojunction," *Applied Physics Letters*, vol. 79, pp. 4482-4484, 2001.
[176] Abdel Haleem AM, and Ichimura Masaya, "Experimental determination of band offsets at the SnS/CdS and SnS/InSxOy heterojunctions," *Journal of Applied Physics*, vol. 107, pp. 034507, 2010.
[177] Miller Irwin, *Probability, random variables, and stochastic processes*. 1966, Taylor & Francis Group.
[178] Van der Ziel Aldert, "Noise in measurements," 1976.
[179] Kogan Sh, *Electronic noise and fluctuations in solids*. 2008: Cambridge University Press.
[180] Hofman F, Zijlstra RJJ, De Freitas JM Bettencourt, and Henning JCM,

"Generation-recombination noise in $Al_xGa_{1-x}As$," *Solid-state electronics*, vol. 34, pp. 23-32, 1991.

[181] Van Rheenen AD, Bosman G, and Zijlstra RJJ, "Low frequency noise measurements as a tool to analyze deep-level impurities in semiconductor devices," *Solid-state electronics*, vol. 30, pp. 259-265, 1987.

[182] Bosman G, and Zijlstra RJJ, "Generation-recombination noise in p-type silicon," *Solid-State Electronics*, vol. 25, pp. 273-280, 1982.

[183] Shockley We, and Read Jr WT, "Statistics of the recombinations of holes and electrons," *Physical review*, vol. 87, pp. 835, 1952.

[184] Ng Sze Him, *Low-frequency excess noise in resonant tunneling diodes: a thesis*. 1993.

[185] Deen MJ. *Low Frequency Noise and Excess Currents Due to Trap-Assisted Tunneling in Double Barrier Resonant Tunneling Diodes*. in *Solid State Device Research Conference, 1993. ESSDERC'93. 23rd European*. 1993. IEEE.

[186] Van Rheenen AD, Bosman G, and Van Vliet CM, "Decomposition of generation-recombination noise spectra in separate Lorentzians," *Solid-state electronics*, vol. 28, pp. 457-463, 1985.

[187] Ng Sze-Him, and Surya Charles, "A model for low frequency excess noise in Si-JFETs at low bias," *Solid-state electronics*, vol. 35, pp. 1803-1809, 1992.

[188] Hooge FN, and Hoppenbrouwers AMH, "$1/f$ noise in continuous thin gold films," *Physica*, vol. 45, pp. 386-392, 1969.

[189] Hooge FN, "1/f noise sources," *IEEE Transactions on Electron Devices*, vol. 41, pp. 1926-1935, 1994.

[190] Hooge FN, and Vandamme LKJ, "Lattice scattering causes $1/f$ noise," *Physics Letters A*, vol. 66, pp. 315-316, 1978.

[191] Hooge FN, "On expressions for 1f noise in mobility," *Physica B*, vol. 114, pp. 391-392, 1982.

[192] Handel PH, "Fundamental quantum 1/f noise in semiconductor devices," *IEEE Transactions on Electron Devices*, vol. 41, pp. 2023-2033, 1994.

[193] Handel Peter H, "Quantum approach to 1 f noise," *Physical Review A*, vol. 22, pp. 745, 1980.

[194] Handel PH, "Quantum theory of $1/f$ noise," *Physics Letters A*, vol. 53, pp. 438-440, 1975.

[195] Van der Ziel Adv, and Chenette ER, "Noise in solid state devices," *Advances in Electronics and Electron Physics*, vol. 46, pp. 313-383, 1978.

[196] Simbrunner Clemens, Nabok Dmitrii, Hernandez-Sosa Gerardo, Oehzelt Martin, Djuric Tatjana, et al., "Epitaxy of rodlike organic molecules on sheet silicates a growth model based on experiments and simulations," *Journal of the American Chemical Society*, vol. 133, pp. 3056-3062, 2011.

[197] Ostendorf F, Schmitz C, Hirth S, Kühnle A, Kolodziej JJ, et al., "How flat is an air-cleaved mica surface?," *Nanotechnology*, vol. 19, pp. 305705, 2008.

[198] Zabinski JS, Donley MS, Prasad SV, and McDevitt NT, "Synthesis and

characterization of tungsten disulphide films grown by pulsed-laser deposition," *Journal of materials science*, vol. 29, pp. 4834-4839, 1994.

[199] Devadasan J Jebaraj, Sanjeeviraja C, and Jayachandran M, "Electrodeposition of p-WS_2 thin film and characterisation," *Journal of crystal growth*, vol. 226, pp. 67-72, 2001.

[200] Chatzitheodorou G, Fiechter S, Kunst M, Luck J, and Tributsch H, "Low temperature chemical preparation of semiconducting transition metal chalcogenide films for energy conversion and storage, lubrication and surface protection," *Materials research bulletin*, vol. 23, pp. 1261-1271, 1988.

[201] Verble JL, and Wieting TJ, "Lattice mode degeneracy in MoS_2 and other layer compounds," *Physical review letters*, vol. 25, pp. 362, 1970.

[202] Wieting TJ, and Verble JL, "Infrared and raman studies of long-wavelength optical phonons in hexagonal MoS_2," *Physical Review B*, vol. 3, pp. 4286, 1971.

[203] Zhao Yanyuan, Luo Xin, Li Hai, Zhang Jun, Araujo Paulo T, et al., "Interlayer breathing and shear modes in few-trilayer MoS_2 and WSe_2," *Nano letters*, vol. 13, pp. 1007-1015, 2013.

[204] Zhang X, Han WP, Wu JB, Milana S, Lu Y, et al., "Raman spectroscopy of shear and layer breathing modes in multilayer MoS_2," *Physical Review B*, vol. 87, pp. 115413, 2013.

[205] Sourisseau C, Cruege F, Fouassier M, and Alba M, "Second-order Raman effects, inelastic neutron scattering and lattice dynamics in 2H-WS_2," *Chemical physics*, vol. 150, pp. 281-293, 1991.

[206] Zhao Weijie, Ghorannevis Zohreh, Amara Kiran Kumar, Pang Jing Ren, Toh Minglin, et al., "Lattice dynamics in mono-and few-layer sheets of WS_2 and WSe_2," *Nanoscale*, vol. 5, pp. 9677-9683, 2013.

[207] Li Hong, Zhang Qing, Yap Chin Chong Ray, Tay Beng Kang, Edwin Teo Hang Tong, et al., "From bulk to monolayer MoS_2: evolution of Raman scattering," *Advanced Functional Materials*, vol. 22, pp. 1385-1390, 2012.

[208] Wang X. L., Gong Y. J., Shi G., Chow W. L., Keyshar K., et al., "Chemical vapor deposition growth of crystalline mono layer $MoSe_2$," *Acs Nano*, vol. 8, pp. 5125-5131, 2014.

[209] Brunken Stephan, Mientus Rainald, and Ellmer Klaus, "Metal-sulfide assisted rapid crystallization of highly (001)-textured tungsten disulphide (WS_2) films on metallic back contacts," *Physica Status Solidi a-Applications And Materials Science*, vol. 209, pp. 317-322, 2012.

[210] Girleanu M., Alphazan T., Boudene Z., Bonduelle-Skrzypczak A., Legens C., et al., "Magnifying the morphology change induced by a nickel promoter in tungsten(IV) sulfide industrial hydrocracking catalyst: a HAADF-STEM and DFT study," *Chemcatchem*, vol. 6, pp. 1594-1598, 2014.

[211] Fischetti MV, and Vandehberghe WG. *Physics of electronic transport in two-dimensional materials for future FETs*. in *Electron Devices Meeting (IEDM), 2016 IEEE International*. 2016. IEEE.

[212] Matthaus A., Ennaoui A., Fiechter S., Tiefenbacher S., Kiesewetter T., et al., "Highly textured films of layered metal disulfide 2H-WS_2 - preparation and optoelectronic properties," *Journal of the Electrochemical Society*, vol. 144, pp. 1013-1019, 1997.

[213] Kozawa T, Kachi T, Kano H, Nagase H, Koide N, et al., "Thermal stress in GaN epitaxial layers grown on sapphire substrates," *Journal of applied physics*, vol. 77, pp. 4389-4392, 1995.

[214] Barker Jr AS, and Ilegems M, "Infrared lattice vibrations and free-electron dispersion in GaN," *Physical Review B*, vol. 7, pp. 743, 1973.

[215] Spratt William T, Huang Mengbing, Jia Chuanlei, Wang Lei, Kamineni Vimal K, et al., "Formation of optical barriers with excellent thermal stability in single-crystal sapphire by hydrogen ion implantation and thermal annealing," *Applied Physics Letters*, vol. 99, pp. 111909, 2011.

[216] Senthil Kumar M., Sonia G., Ramakrishnan V., Dhanasekaran R., and Kumar J., "Thermal stability of GaN epitaxial layer and GaN/sapphire interface," *Physica B: Condensed Matter*, vol. 324, pp. 223-228, 2002.

[217] Berkdemir Ayse, Gutiérrez Humberto R, Botello-Méndez Andrés R, Perea-López Néstor, Elías Ana Laura, et al., "Identification of individual and few layers of WS_2 using Raman spectroscopy," *Scientific reports*, vol. 3, pp., 2013.

[218] Thripuranthaka M, Kashid Ranjit V, Sekhar Rout Chandra, and Late Dattatray J, "Temperature dependent Raman spectroscopy of chemically derived few layer MoS_2 and WS_2 nanosheets," *Applied Physics Letters*, vol. 104, pp. 081911, 2014.

[219] Sekine T, Nakashizu T, Toyoda K, Uchinokura K, and Matsuura E, "Raman scattering in layered compound 2H-WS_2," *Solid State Communications*, vol. 35, pp. 371-373, 1980.

[220] Elias A. L., Perea-Lopez N., Castro-Beltran A., Berkdemir A., Lv R. T., et al., "Controlled synthesis and transfer of large-area WS_2 sheets: from single layer to few layers," *Acs Nano*, vol. 7, pp. 5235-5242, 2013.

[221] Xu Z. Q., Zhang Y. P., Lin S. H., Zheng C. X., Zhong Y. L., et al., "Synthesis and transfer of large-area monolayer WS_2 crystals: moving toward the recyclable use of sapphire substrates," *Acs Nano*, vol. 9, pp. 6178-6187, 2015.

[222] Azimi G., Dhiman R., Kwon H. M., Paxson A. T., and Varanasi K. K., "Hydrophobicity of rare-earth oxide ceramics," *Nature Materials*, vol. 12, pp. 315-320, 2013.

[223] Chow P. K., Singh E., Viana B. C., Gao J., Luo J., et al., "Wetting of mono and few-layered WS_2 and MoS_2 films supported on Si/SiO_2 substrates," *Acs Nano*, vol. 9, pp. 3023-3031, 2015.

[224] Vargaftik NB, Volkov BN, and Voljak LD, "International tables of the surface tension of water," *Journal of Physical and Chemical Reference Data*, vol. 12, pp. 817-820, 1983.

[225] Reina A., Jia X. T., Ho J., Nezich D., Son H. B., et al., "Large area, few-layer graphene films on arbitrary substrates by chemical vapor deposition," *Nano*

Letters, vol. 9, pp. 30-35, 2009.

[226] Jiang X., and Jia C. L., "Diamond epitaxy on (001)silicon - an interface investigation," *Applied Physics Letters*, vol. 67, pp. 1197-1199, 1995.

[227] Lan C. Y., Li C., Yin Y., and Liu Y., "Large-area synthesis of monolayer WS_2 and its ambient-sensitive photo-detecting performance," *Nanoscale*, vol. 7, pp. 5974-5980, 2015.

[228] Yuan S. J., Roldan R., Katsnelson M. I., and Guinea F., "Effect of point defects on the optical and transport properties of MoS_2 and WS_2," *Physical Review B*, vol. 90, pp. 5, 2014.

[229] Shah Jay M, Li Y-L, Gessmann Th, and Schubert EF, "Experimental analysis and theoretical model for anomalously high ideality factors (n≫ 2.0) in AlGaN/GaN pn junction diodes," *Journal of Applied Physics*, vol. 94, pp. 2627-2630, 2003.

[230] Yamamoto N., and Yamamoto M., "Evaluation of p-n junction shift by the capacitance-voltage method," *Journal of Crystal Growth*, vol. 145, pp. 941-946, 1994.

[231] Mohammad S. N., Salvador A. A., and Morkoc H., "Emerging gallium nitride based devices," *Proceedings of the IEEE*, vol. 83, pp. 1306-1355, 1995.

[232] Cong C. X., Shang J. Z., Wu X., Cao B. C., Peimyoo N., et al., "Synthesis and optical properties of large-area single-crystalline 2D semiconductor WS_2 Monolayer from Chemical Vapor Deposition," *Advanced Optical Materials*, vol. 2, pp. 131-136, 2014.

[233] Zhang Yuanbo, Tang Tsung-Ta, Girit Caglar, Hao Zhao, Martin Michael C, et al., "Direct observation of a widely tunable bandgap in bilayer graphene," *Nature*, vol. 459, pp. 820-823, 2009.

[234] Lin Ming-Wei, Liu Lezhang, Lan Qing, Tan Xuebin, Dhindsa Kulwinder S, et al., "Mobility enhancement and highly efficient gating of monolayer MoS_2 transistors with polymer electrolyte," *Journal of Physics D: Applied Physics*, vol. 45, pp. 345102, 2012.

[235] Agarwal MK, and Reddy K Nagi, "Etching studies of tungstenite (WS_2) crystals in acids," *Crystal Research and Technology*, vol. 15, pp. 225-229, 1980.

[236] Baugher Britton WH, Churchill Hugh OH, Yang Yafang, and Jarillo-Herrero Pablo, "Intrinsic electronic transport properties of high-quality monolayer and bilayer MoS_2," *Nano letters*, vol. 13, pp. 4212-4216, 2013.

[237] Liu Wei, Kang Jiahao, Sarkar Deblina, Khatami Yasin, Jena Debdeep, et al., "Role of metal contacts in designing high-performance monolayer n-type WSe_2 field effect transistors," *Nano letters*, vol. 13, pp. 1983-1990, 2013.

[238] Georgiou Thanasis, Jalil Rashid, Belle Branson D., Britnell Liam, Gorbachev Roman V., et al., "Vertical field-effect transistor based on graphene-WS_2 heterostructures for flexible and transparent electronics," *Nature Nanotechnology*, vol. 8, pp. 100-103, 2013.

[239] Yoon Youngki, Ganapathi Kartik, and Salahuddin Sayeef, "How good can

monolayer MoS_2 transistors be?," *Nano Letters*, vol. 11, pp. 3768-3773, 2011.
[240] Radisavljevic Branimir, Whitwick Michael B, and Kis Andras, "Small-signal amplifier based on single-layer MoS_2," *Applied Physics Letters*, vol. 101, pp. 043103, 2012.
[241] Ovchinnikov Dmitry, Allain Adrien, Huang Ying-Sheng, Dumcenco Dumitru, and Kis Andras, "Electrical transport properties of single-layer WS_2," *ACS nano*, vol. 8, pp. 8174-8181, 2014.
[242] Liu Xue, Hu Jin, Yue Chunlei, Della Fera Nicholas, Ling Yun, et al., "High performance field-effect transistor based on multilayer tungsten disulfide," *ACS nano*, vol. 8, pp. 10396-10402, 2014.
[243] Park Woanseo, Baik Jaeyoon, Kim Tae-Young, Cho Kyungjune, Hong Woong-Ki, et al., "Photoelectron spectroscopic imaging and device applications of large-area patternable single-layer MoS_2 synthesized by chemical vapor deposition," *ACS nano*, vol. 8, pp. 4961-4968, 2014.
[244] Xu Zai-Quan, Zhang Yupeng, Lin Shenghuang, Zheng Changxi, Zhong Yu Lin, et al., "Synthesis and transfer of large-area monolayer WS_2 crystals: moving toward the recyclable use of sapphire substrates," *ACS nano*, vol. 9, pp. 6178-6187, 2015.
[245] Ponomarenko LA, Geim AK, Zhukov AA, Jalil R, Morozov SV, et al., "Tunable metal-insulator transition in double-layer graphene heterostructures," *Nature Physics*, vol. 7, pp. 958-961, 2011.
[246] Britnell L, Gorbachev RV, Jalil R, Belle BD, Schedin F, et al., "Field-effect tunneling transistor based on vertical graphene heterostructures," *Science*, vol. 335, pp. 947-950, 2012.
[247] Haigh SJ, Gholinia A, Jalil R, Romani S, Britnell L, et al., "Cross-sectional imaging of individual layers and buried interfaces of graphene-based heterostructures and superlattices," *Nature materials*, vol. 11, pp. 764-767, 2012.